The Response of Metals with Different Crystal Structures to High Strain Rate Loading and Other Mechanical Tests

by

Daniel Louis Higgins

Thesis

Submitted to the University of Birmingham

for the degree of

Doctor of Philosophy

School of Metallurgy and Materials

March 2017

Declarations

The work described in this thesis was carried out by the author in the School of Metallurgy and Materials, the University of Birmingham from Jan. 2013 to Mar. 2017, under the supervision of Prof. Ian Jones and Dr. Yu-Lung Chiu.

The present work is original and no part of this work has been submitted for a degree at any other university. Wherever others work has been drawn or cited, it is acknowledged in the text and a list of references is included at the end of this thesis.

Part of the present work has been published as follows:

D. L. Higgins, B. Pang, J. C. F. Millett, G, Whiteman, I. P. Jones and Y.-L. Chiu. Contrasting the Microstructural and Mechanical Response to Shock Loading of Cold-Rolled Copper with Annealed Copper. *Metallurgical and Materials Transactions A*, 40: 4518–4521

Acknowledgments

I would like to thank my supervisors, Prof. Ian Jones and Dr. Yu-Lung Chiu for giving me the chance to carry out this project and for guiding and supporting me through the entire process. Thank you to Jeremy Millett and Glenn Whiteman for sponsoring the project and providing specimens in the face of multiple, unavoidable setbacks. I would also like to thank Paul Stanley and Theresa Morris for providing training on a wide variety of machines and for fighting against entropy to keep those machines functioning during the course of this project.

Thank you to all the other students and post docs in the EM Group who have made the office such a welcoming place these last 4 years: Rengen Ding, Ubaid Ur Rehman Ghori, Jinsen Tian, Zhaoran Liu, Yu Lu, Xinyu Lu, Yang Lyu, Thiago Pereira, Subash Rai, Shanshan Si, Minshi Wang, Jing Wu and Xinxin Zhao. Special thanks to Rayan Ameen for helping me really learn the ropes on the FIB and reassuring me that I wasn't going to break it; to Bo Pang for helping me come to an understanding of shock physics through mutual confusion, and to Gareth Douglas for being a consistent unofficial microscope technician and lab tech, and the occasional recipient of a good old complain.

Final thanks to my wonderful girlfriend Laura, whose loving support has kept me going through the last four years and to my parents, Lilian and Louis Higgins, who have always been more kind, generous and supportive than I could ever have hoped.

Abstract

The effect of cold-rolling prior to shock loading was investigated in copper and tantalum. Annealed copper was shocked at a peak pressure of 5.08 GPa; cold-rolled copper was shocked at peak pressures of 5.87 GPa, 5.96 GPa and 9.60 GPa; as-received tantalum was shock loaded at a peak pressure of 7.20 GPa, and cold-rolled tantalum was shocked at a peak pressure of 7.20 GPa. The microstructural responses of the materials were investigated using scanning electron microscopy (SEM) and transmission electron microscopy (TEM), and the mechanical responses were investigated using compression and hardness testing. Pre-straining copper before shock loading was found to reduce the significant strain rate sensitivity observed in annealed copper. Cold-rolled tantalum was found to evidence no significant strain rate sensitivity, much like annealed tantalum. Evidence was also found linking a decrease in the peak shock pulse duration with an increase in hardness in the shock loaded material.

The effect of varying temperature and strain rate on tantalum during compression was investigated. Tantalum was compressed at 20°C at $10^{-3}s^{-1}$, $10^{-1}s^{-1}$ and $2 \times 10^{3}s^{-1}$, and at $10^{-1}s^{-1}$ at -40°C and 170°C. The quasi-static compression tests applied 70% strain to the samples and the higher strain rate sample, compressed by Split Hopkinson Pressure Bar (SHPB) was compressed to 19% strain. The microstructural responses of the materials were investigated using (SEM) and (TEM), and the mechanical responses were investigated using hardness and compression testing. The yield strengths of the samples were found to increase with increasing strain rate and decreasing temperature, as expected. It is suggested that the hardness in the compressed samples is linked to interstitial pinning and increases with increasing temperature and decreasing strain rate.

The microstructures of adiabatic shear bands (ASBs) produced using a new technique were investigated. The technique involved an alteration of the well known thick walled cylinder (TWC) collapse method, substituting a shaped impactor fired from a single stage gas gun for the more traditional shaped explosive charge. In addition,

the propagation of the ASBs along the cylindrical axis of the TWC was investigated. The microstructure was investigated using (SEM), (TEM) and scanning transmission electron microscopy (STEM). The ASBs formed were found to match the morphology and microstructure of previous ASBs formed using the TWC collapse method. ASB propagation along the length of the TWC was found to be free from the influence of the geometrical factors that dominate ASB propagation in the radial direction of the TWC, with the structure of the ASB dominated by the shear strain in the radial direction.

Contents

Abbreviations

ASB	...	Adiabatic Shear Band
BSE	...	Back Scattered Electron
CRSS	...	Critically Resolved Shear Stress
EBSD	...	Electron Back Scattered Diffraction
EDM	...	Electrical Discharge Machining
EDS	...	Electron Dispersive Spectroscopy
FIB	...	Focused Ion Beam
OFHC Cu	...	Oxygen Free High Conductivity Copper
SEM	...	Scanning Electron Microscope
SHPB	...	Split Hopkinson Pressure Bar
STEM	...	Scanning Transmission Electron Microscope
TEM	...	Transmission Electron Microscope
TKD	...	Transmission Kikuchi Diffraction
TWC	...	Thick Walled Cylinder

List of Figures

List of Tables

Chapter 1

Introduction

Knowledge of a material's response to deformation under a range of conditions is vitally important when determining its suitability for use. This is especially important when considering high strain rate deformation, as a range of high speed collisions are a risk in a variety of industries. Copper and tantalum are well known "model materials" for investigating the shock response of fcc and bcc materials respectively. In addition, tantalum sees use in explosively formed projectiles, which require a knowledge of the material's response to high strain rate loading to fully understand. Full investigations into the effect of pre-shock straining on the materials have not yet been carried out. It is important to understand the impact of refinement on the materials in question, as they could render unsuitable materials suitable, or suitable materials unsuitable for a specific purpose.

To reduce the number of variables under consideration after high strain rate loading, the loading regime used should be made as simple as possible. To this end, in this study momentum trapping was used to ensure that the specimens were subjected to a planar shock wave originating from the impact face and a planar release wave originating from the rear surface of the impactor. In this study, polycrystalline as-received and cold-rolled (50% reduction in thickness) tantalum specimens were subjected to 7.2 GPa plate impact experiments using a single stage gas gun. Annealed polycrystalline copper specimens were subjected to a 5.08 GPa plate impact experiment and cold-rolled polycrystalline copper specimens were subjected to 5.87 GPa and 9.60 GPa plate impact

experiments. Momentum trapping was used to ensure that the loading regimes were uncomplicated by release waves other than that generated at the rear surface of the impactor.

A potential response to high strain rate loading is the initiation of localised strain, which leads to the formation of adiabatic shear bands. These are well defined bands of material that have experienced a large degree of shear strain and act as precursors to failure in the material. Materials that have a low thermal conductivity and a high thermal softening coefficient are particularly susceptible to this form of deformation. These material properties describe titanium 6Al-4V, or grade 5 titanium alloy, which is the most commonly used titanium alloy in the world. Titanium 6Al-4V sees extensive use in the aerospace industry, so it is vital that this deformation behaviour be well understood.

A well used method for the generation of adiabatic shear bands is the collapse of a thick walled cylinder. This is usually achieved using explosives, but a new method using a single-stage gas gun and a shaped impactor has been attempted. This study investigates the microstructure of adiabatic shear bands in a collapsed thick walled cylinder of titanium 6Al-4V.

At strain rates lower than 8000 s^{-1} the yield strength of tantalum increases with decreasing temperature and increasing strain rate. As tantalum is often used as a model material for bcc metals, understanding the origins of these responses is an important step in understanding the behaviour of bcc metals. This study investigates the response of polycrystalline tantalum to compression under a variety of conditions: compression at $10^{-3}s^{-1}$, $10^{-1}s^{-1}$ and $2 \times 10^{3}s^{-1}$ at 20°C and compression at -40°C and 170°C at $10^{-3}s^{-1}$. The compression at $10^{-3}s^{-1}$ had a loading time of ≈520 s; the compressions at $10^{-1}s^{-1}$ had a loading time of ≈5.2 s and the compression at $2 \times 10^{3}s^{-1}$ had a loading time of ≈70 μs.

Chapter 2

Literature review

2.1 Defects in Plastic Deformation

It is well known that metals have a crystal structure, which means that their constituent atoms are arranged in a pattern that repeats itself in three dimensions. The three most common crystal structures are face centered cubic (fcc), body centered cubic (bcc) and hexagonal close packed (hcp). The focus of this project is on metals with all three of these structures: copper (fcc), tantalum (bcc) and titanium 6Al-4V (bcc and hcp). If these perfect crystal structures are subjected to plastic strain, defects are introduced that interrupt the repeating pattern. The three defects that are discussed in this project are dislocations, deformation twins and shear bands. Shear bands will be discussed in greater detail in Section 2.7.3.

2.1.1 Dislocations

Dislocations are irregularities in the periodic crystal structure of materials. The best way to describe dislocations is in the form of a schematic model, as in Figure 2.1. From these models it can be seen that dislocations come in two forms: edge dislocations, which appears as if an extra half plane has been inserted into the crystal lattice and screw dislocations, which appear as if the crystal has been cut along a plane to a specific line and then the crystal above that line has been offset by a single atomic spacing. Screw dislocations can occur as right-handed and left-handed. The handedness of screw dislocations is determined by drawing a clockwise loop around the dislocation. If the loop

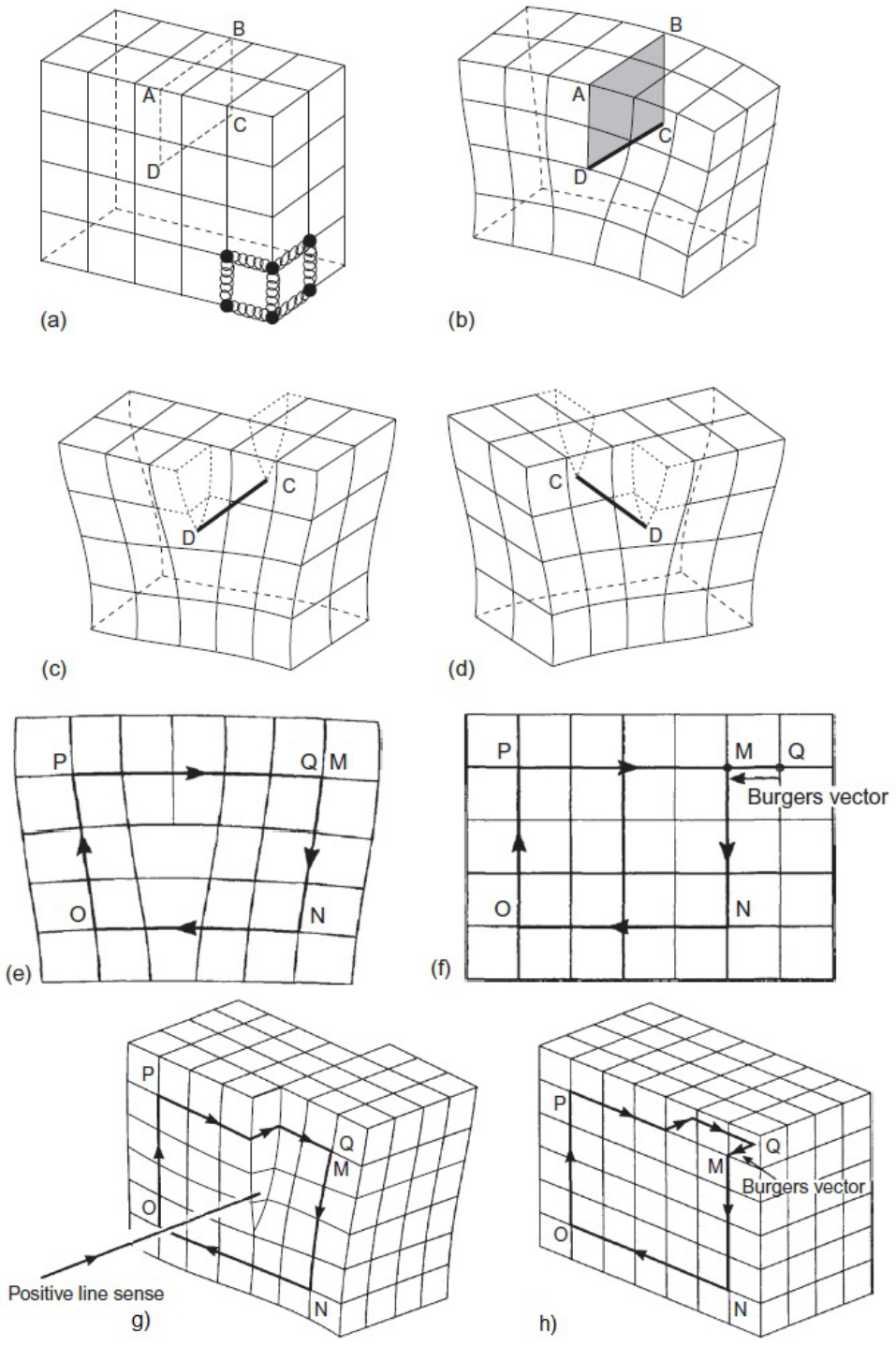

Figure 2.1: *a) Model of a simple cubic lattice; b) edge dislocation DC formed by inserting a half plane of atoms in ABCD; c) left-handed screw dislocation DC formed by displacing the faces of ABCD relative to each other; d) right-handed screw dislocation DC; e) Burgers circuit round an edge dislocation, with positive line sense into the paper; f) the Burgers circuit transposed onto a perfect crystal with Burgers vector included; g) Burgers circuit round a left-handed screw dislocation; h) the Burgers circuit transposed onto a perfect crystal with Burgers vector included. [1]*

moves into the page, then the dislocation is left-handed and if it moves out of the page it is right-handed. Examples of right- and left-handed screw dislocations can be seen in Figure 2.1. Dislocations are defined by the Burgers vector. If a loop is imagined around a dislocation, then this loop is transposed onto an undeformed crystal lattice, then this loop will not be closed. The Burgers vector is the vector required to close the loop. This loop is called a Burgers circuit. Examples for both edge and screw dislocations can be seen in Figure 2.1e–h. The positive line sense for a dislocation is defined by applying the right hand rule to the Burgers circuit. The time scales required for dislocation nucleation are on the order of 50 ps and the time scales for dislocation-dislocation interactions are on the order of 100 ns [13].

2.1.2 Deformation Twinning

During the process of deformation twinning, a section of the crystal structure is sheared in such a way as to reproduce the original crystal structure, but in a different orientation. This sheared section is known as a twin. The simplest version of this process results in the crystal structure of the twin being a mirror image of the original crystal structure, reflected in the so-called "composition plane". A schematic of this mirrored twin structure can be seen in Figure 2.2. The time scales required for twinning nucleation are on the order of 1 ns [13].

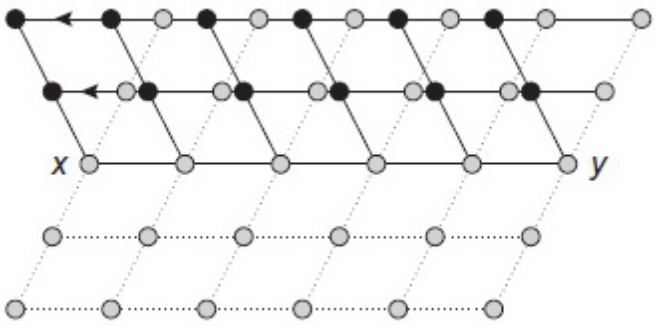

Figure 2.2: *Schematic showing the movement of atoms during the creation of a twin with a crystal structure mirrored in the composition plane, here defined as the plane between x and y. The grey atoms are the original crystal orientation and the black atoms are those of the twin. [1]*

2.2 Copper

2.2.1 Copper Applications

Copper is a transition metal known and used since antiquity, with an fcc structure and atomic number 29. Due to its high ductility and thermal and electrical conductivity, copper is commonly used in wiring and other electronic devices, in the form of heat exchangers, heat sinks, electromagnets and so on. Copper is a biostatic material, which means that, while not actively producing a disinfectant effect, the growth of microbes and other forms of life is severely restricted while adjacent to the material. This has led to the use of copper alloys in a variety of home applications and also in its pure form on the keels of British ships of the line in the 18th and 19th centuries, to prevent biofouling by barnacles and mussels [14]. The alloy Muntz metal and copper paint are still used for this purpose. Copper has also seen extensive use as an architectural material for its corrosion resistance, low density and low thermal expansion properties relative to other metals traditionally used for roofing, such as lead.

Copper alloys, including brass and bronze are used for a variety of purposes generally because of their thermal, electrical and corrosion resistance properties. Exceptions to this are beryllium copper, which is prized as a non-sparking, non-magnetic and physically tough alloy and consequently sees most of its use in tools, high cost armour penetrating bullets and the aerospace industry, and phosphor bronze which can be used for marine propellers due to its low coefficient of friction, high strength and corrosion resistance.

These applications of pure copper do not seem to require much knowledge of its behaviour under high strain rate loading. Apart from its alloys, copper sees very little use in an industrial setting (with the exception of all copper bullets, which are becoming an increasingly popular alternative to lead bullets in hunting as a way of preventing lead poisoning from adversely affecting scavengers). However, copper is frequently used in high strain rate experiments in order to investigate the strain rate sensitivity of fcc metals [15, 16]. For this reason, the response of copper to high strain rate loading is well understood, providing a solid foundation from which to introduce additional complexity

into a high strain rate experiment. A description of the response of copper during shock loading will be provided in a later section.

2.2.2 Plastic Deformation of Copper

Copper has 4 $\{111\}$ slip planes, each of which can slip along 3 $\langle 110 \rangle$ directions, making in total 12 possible slip systems. The flow stress of copper decreases with increasing temperature [17]. The high stacking fault energy of copper enables easy cross slip of dislocations. This has the effect of copper expressing strain through the movement of dislocations rather than twinning and ultimately leading to the formation of a dislocation cell structure [18].

The hardening of copper has often been described in the context of a three stage hardening process. In this process Stage I is limited to the behaviour of single crystals and describes the activation of a single slip system. Stage II is common to both single and polycrystals and is characterised by a linear increase in work hardening. Stage III is the crossover to a steady decrease in the work hardening rate, finishing when dislocation recovery reaches an equilibrium with dislocation storage, preventing further hardening. In reality, however, the end of Stage III has been found to be the beginning of a Stage IV, where a steady increase in hardening exists at higher strains. This ends at Stage V with additional dynamic recovery and the saturation of the flow stress which originally was thought to have occurred at the end of Stage III [19].

2.3 Tantalum

2.3.1 Tantalum Applications

Tantalum is a transition metal, like copper and is also a member of the refractory metals group, with bcc structure and an atomic number of 73. Tantalum is mainly used in the manufacturing of capacitors for use in electrical equipment. Due to its high melting point of 3290 K and its resistance to oxidation, tantalum is often used to produce components

for vacuum furnaces. Its bioinertness also makes tantalum ideal for biomechanical applications. The high ductility and density (16,690 kgm^{-3}) of tantalum have led to its use in explosively forged projectiles. It is for this reason that an understanding of the response of tantalum to deformation over a range of temperatures and strain rates is so important.

2.3.2 Plastic Deformation of Tantalum

Tantalum has 6 $\{110\}$ slip planes, each of which can slip along 2 $\langle 111 \rangle$ directions, making 12 possible slip systems. Being bcc, tantalum also theoretically has an additional 24 $\{123\}$ and 12$\{112\}$ slip planes which can each slip along a single $\langle 111 \rangle$ direction, giving an extra 36 slip systems. The preferred slip is along the $\{110\}$ planes and it has been postulated that traces of $\{112\}$ and $\{123\}$ planes during tensile tests can actually be explained by two non-parallel $\{110\}$ planes sharing the same slip direction [20]. However, tantalum tends to slip along the plane with the highest resolved shear stress (RSS) regardless of indices and then cross-slip back to a $\{110\}$ plane. [20].

Again like copper, tantalum has been found to undergo three stage hardening during deformation. This is more difficult to observe in tantalum than in copper due a range of factors. The flow stress of tantalum dramatically increases at low temperatures, masking the hardening process. At high temperatures, the stress-strain curve becomes parabolic, eliminating Stages I and II hardening. These two factors combine to give a temperature window of $T/T_m \approx 0.10 - 0.18$, where T is the temperature at which deformation is taking place and T_m is the melting point of the metal, where three stage hardening can occur. This also applies to high strain rates, which are analogous to low temperatures. In addition to these factors, the tendency of tantalum to slip along the plane with the highest RSS instead of along a well-defined crystallographic planes, makes stage I hardening (which involves single glide) difficult. [21]

Three stage hardening in tantalum consists of: (i) the formation of dislocation tangles along slip planes; (ii) the increase in density of these tangles, forming dislocation walls, and finally (iii) the formation of sub-grains, which decrease in size with increasing strain [2]. Micrographs illustrating three stage hardening in tantalum can be seen in

Figure 2.3 [2].

2.4 Titanium 6Al-4V

Titanium 6Al-4V (also known as Grade 5 titanium alloy) is an alloy of titanium with 5.5-6.75% aluminium, 3.5-4.5% vanadium and will also contain iron, often restricted to a maximum of 0.3% [22]. It has a low thermal conductivity of 5.8 $Wm^{-1}K^{-1}$ [23] and a high thermal softening coefficient [24,25]. It is an alpha-beta alloy, with a microstructure

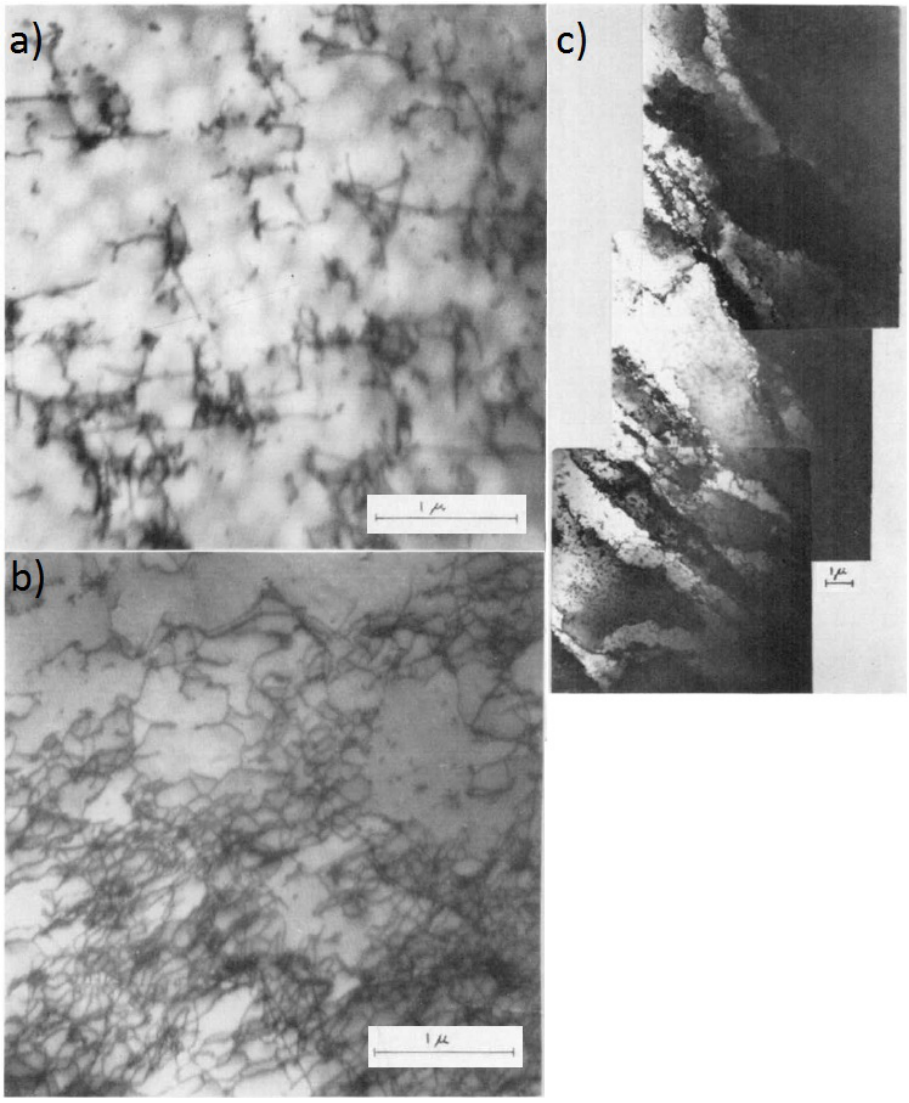

Figure 2.3: *TEM micrographs illustrating three stage hardening in tantalum. Displaying: a) stage I with dislocation tangles; b) stage II with dislocation cell walls, and c) stage III with sub-grains [2].*

composed of alpha lath colonies with an hcp structure and beta laths located between the alpha colonies with a bcc structure [26]. Aluminium acts as an alpha stabiliser, so a higher aluminium percentage will be present in the alpha grains and vanadium and iron act as beta stabilisers, so a higher percentage of vanadium and iron will be present in the beta grains [27].

Due to its high strength, relatively low density, corrosion resistance and ability to be heat treated titanium 6Al-4V is currently the most commonly used titanium alloy in the world. Over 50% of all titanium alloy in use is titanium 6Al-4V. Of this, over 80% is used by the aerospace industry, where strength and weight considerations are paramount. Titanium 6Al-4V sees extensive use in turbine engines and airframes. In addition, 3% of titanium 6Al-4V is used for biomedical implants due to its good tensile and fatigue strength and also its biological compatibility. It is used for bone screws and in the replacement of a variety of joints [22].

2.5 Shock loading

2.5.1 Introduction

Shock loading at its most fundamental level can be understood to be the loading of a material at a high strain rate. This high rate strain often takes the form of a shock wave, a discontinuous compression wave that moves through the material at the speed of sound within that material. These are generated using explosives, high velocity impacts and even laser shots. Understanding the material response to shock loading is of vital importance to a variety of industries. For example: bird strikes in the aerospace industry; micrometeorite impacts on satellites, and more military applications such as armour and armour-defeat.

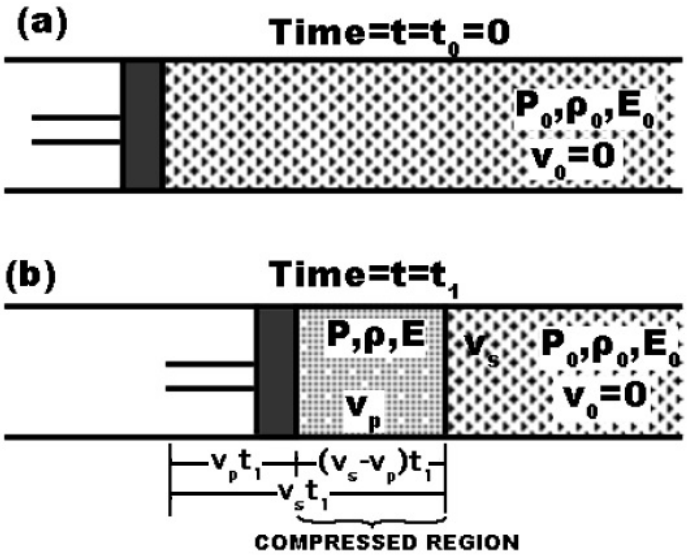

Figure 2.4: *A schematic showing shock compression by the impact of a piston. a) At time $t = t_0 = 0$ a piston with velocity v_p is introduced and makes contact with undeformed material with density ρ_0, pressure P_0, internal energy E_0 and velocity v_0. b) At a time t_1, the piston has moved a distance $v_p t_1$. The shock wave created by the impact of the piston on the undeformed material has velocity v_s and has advanced a distance $v_s t_1$. The deformed material behind the shock wave has density ρ, pressure P, internal energy E, and velocity v_p [3].*

2.5.2 Equations of State

A shock wave is defined as the boundary between undeformed material and material deformed by discontinuous compression. Shock waves are generated whenever an object is subjected to an impact at high enough speeds. At a certain velocity, the object cannot respond to the impact by moving in the direction of the impact and an elastic wave and a plastic front is produced within the object. The plastic front emerges when the applied stress is greater than the yield strength of the material under compression. The conditions on either side of a shock wave are defined in Figure 2.4 [3]. The material initially has a density ρ_0, pressure P_0, internal energy E_0 and velocity v_0. After the compression of the material by a piston moving at velocity v_p, a shock wave with velocity v_s divides the object into uncompressed and compressed material. The compressed material has density ρ, pressure P, internal energy E, and velocity v_p.

Equations of state for the relationships between these factors can be derived [3]. For the first two derivations, the shock wave will be considered as a stationary reference point, with mass moving towards the wave and away from the wave. Beginning with

the conservation of mass, the mass moving towards the shock front ($A\rho_0 (v_s - v_0)\, dt$) is equal to the mass moving away from the shock front ($A\rho (v_s - v_p)\, dt$):

$$A\rho_0 (v_s - v_0)\, dt = A\rho (v_s - v_p)\, dt \tag{2.1}$$

where A is the area of the shock wave and dt is the time increment. Simplifying the equation and taking $v_0 = 0$ gives:

$$\rho_0 v_s = \rho(v_s - v_p) \tag{2.2}$$

The conservation of momentum requires that a change in the momentum must be matched by an impulse applied to the material. The change in momentum (Δp) is given by:

$$\Delta p = \rho A (v_s - v_p)\, dt - \rho_0 A (v_s - v_0)\, dt \tag{2.3}$$

The impulse (I) is given by:

$$I = (PA - P_0 A) \tag{2.4}$$

Equating Equations 2.3 and 2.4, simplifying and setting $v_0 = 0$ gives:

$$P - P_0 = \rho_0 v_s v_p \tag{2.5}$$

Deriving the equation for the conservation of energy requires setting the work done by P minus the work done by P_0 equal to the difference in energy (E_T) on either side of the shock wave. The difference in the work done (ΔW) by P and P_0 is given by:

$$\Delta W = (PA)(v_p dt) - (P_0 A)(v_0 dt) \tag{2.6}$$

The difference in E_T (which can be broken down into kinetic energy plus internal energy) is given by:

$$\Delta E_T = \frac{1}{2}[\rho A\,(v_s - v_p)\,dt]v_p^2 + EA\rho\,(v_s - v_p)\,dt - \{\frac{1}{2}[\rho_0 A\,(v_s - v_0)\,dt]v_0^2 + E_0 A\rho_0\,(v_s - v_0)\,dt\} \quad (2.7)$$

Equating Equation 2.6 and 2.7, setting $v_0 = 0$ and simplifying gives:

$$E - E_0 + \frac{1}{2}\,(P + P_0)\left(\frac{1}{\rho_0} - \frac{1}{\rho}\right) \quad (2.8)$$

The final equation of state is the simplification of an empirically derived polynomial equation:

$$v_s = C_0 + S_1 v_p \quad (2.9)$$

where C_0 is the speed of sound in the material and S_1 is an empirically derived material constant. Both C_0 and S_1 are known as the Hugoniot parameters of the material. If these two parameters are known, along with one of the variables P, E, ρ, v_s, and v_p, then the rest of the variables can be determined.

The equations of state can be solved to give a relationship between P and the specific volume $(\frac{1}{\rho})\ V$:

$$P = \frac{C_0^2\,(V_0 - V_1)}{[V_0 - S\,(V_0 - V_1)]^2} \quad (2.10)$$

This equation can be used to generate a theoretical stress-strain curve for a material under shock loading. An example of this can be seen in Figure 2.5. The original Hugoniot curve from Equation 2.10 is present and labelled, but the more accurate curve has been offset from the origin by the elastic precursor wave line OA. As the name suggests, this elastic precursor wave is the initial elastic wave that propagates into the material before the yield point is reached. This yield point is referred to as the Hugoniot elastic limit (HEL) and is located at point A in Figure 2.5. The HEL can be derived by applying Hooke's law under one-dimensional strain:

$$\nu_x = \frac{1}{E}[\sigma_x - \nu\,(\sigma_y + \sigma_z)] \tag{2.11}$$

$$\nu_y = \frac{1}{E}[\sigma_y - \nu\,(\sigma_x + \sigma_z)] \tag{2.12}$$

$$\nu_z = \frac{1}{E}[\sigma_z - \nu\,(\sigma_x + \sigma_y)] \tag{2.13}$$

$$\sigma_y = \sigma_z \tag{2.14}$$

where ν is Poisson's ratio, σ is the longitudinal stress and E is Young's modulus for the material. Substituting Equation 2.14 into Equations 2.11, 2.12 and 2.13 and rearranging gives:

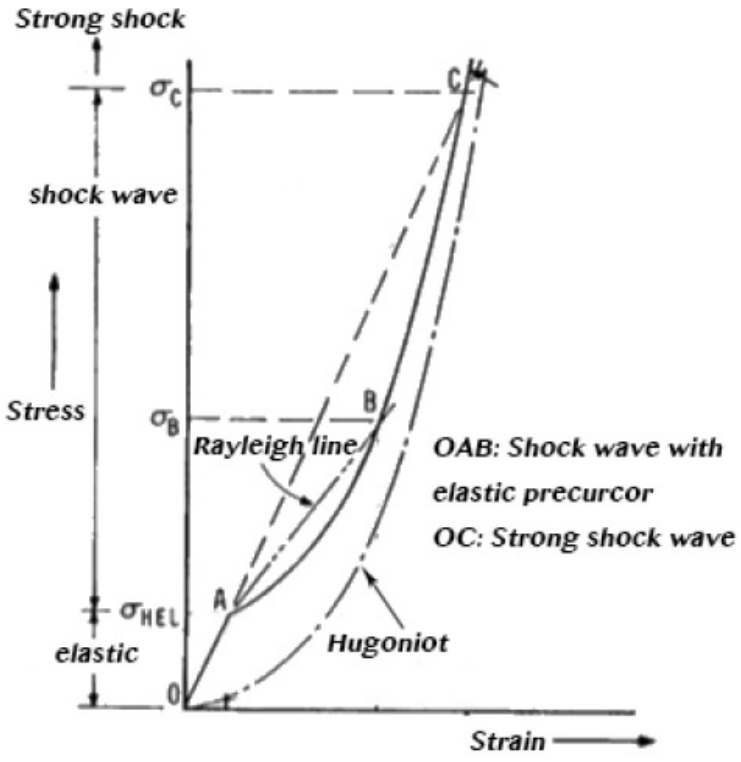

Figure 2.5: *The theoretical Hugoniot stress-strain curve of a material during shock loading. The elastic precursor wave is present as line OA, with the Hugoniot Elastic Limit (HEL) situated at point A. The boundary between shock and strong shock can be seen when the gradient of the Hugoniot matches the gradient of the elastic precursor wave [3].*

$$\sigma_y = \sigma_z = \frac{\nu}{1-\nu}\sigma_x \tag{2.15}$$

Applying the von Mises yield criterion: $\sigma_x - \sigma_y = Y$, where Y is the yield strength of the material, gives:

$$\sigma_{HEL} = \frac{1-\nu}{1-2\nu}Y \tag{2.16}$$

where σ_{HEL} is also the Hugoniot elastic limit.

The hydrodynamic pressure P is defined as:

$$P = \frac{1}{3}\left(\sigma_x + \sigma_y + \sigma_z\right) \tag{2.17}$$

which is the mean of the three orthogonal stresses. Substituting in Equation 2.14 equating σ_y and σ_z and the shear stress τ defined as:

$$\tau = \frac{1}{2}\left(\sigma_x - \sigma_y\right) \tag{2.18}$$

gives:

$$\sigma_x = P + \frac{4}{3}\tau \tag{2.19}$$

which demonstrates the separation of the longitudinal stress σ_x into hydrostatic and deviatoric components [28]. This deviatoric stress component is the portion of the applied stress that causes the material volume to distort, setting up the stressed plane between the uncompressed and compressed crystal lattice at the front of the shock wave and P is the mean of the applied stresses. These are the stress components in the shocked material after a uniaxial strain has been applied to the specimen. An elasto-plastic material will respond to rising stress in the shock front elastically, until the HEL (as defined in Equation 2.16) is reached, after which the material will behave plastically. This "yield surface" at which plastic strain as occurred will move through the material as subsequent points along the path of the shock wave are brought to the HEL by the

applied stresses. In reality, this simply the point at which the yield stress is reached moving through the material, but it can be useful to think of this yield surface as a plastic wave (or series of plastic waves) following the initial elastic precursor wave.

It becomes necessary at this point to explain why, after passing the HEL, there exists a discontinuous plastic shock wave as well as the discontinuous elastic precursor wave. The sound speed within a compressive fluid (c) is given by the equation:

$$c = \sqrt{\frac{\partial P}{\partial \rho}} \tag{2.20}$$

In the case of the elastic precursor wave, the pressure and density are linearly related and the speed of the wave c_E is governed by the equation [29]:

$$c_E^2 = \frac{E\,(1-\nu)}{\rho_0\,(1-2\nu)\,(1-\nu)} \tag{2.21}$$

This results in a single elastic shock wave. Beyond the elastic region, the wave speed (c_p) is given by:

$$c_p = \sqrt{\frac{1}{\rho_0}\frac{d\sigma}{d\epsilon}} \tag{2.22}$$

This condition allows for a series of waves, with velocities that increase with the strain experienced by the material. As strain increases, waves of higher and higher velocity are produced. These higher velocity waves catch up to the lower velocity waves until a single, discontinuous plastic front is present in a process known as "shocking-up" [29].

An important distinction to make when discussing the Hugoniot and the shock jump conditions is the real-world meaning of the Hugoniot and the relevance of the Rayleigh line present in Figure 2.5. The Hugoniot is not a path that the shock wave takes, nor is the Rayleigh line. Instead, the Hugoniot can be thought of as a locus of possible points and the Rayleigh line as the indicator of which point is selected. As the shock wave is a discontinuous front, the conditions jump directly from point A to point B after the HEL is passed. Under further investigation of the combined elastic

wave-Hugoniot curve, another important point becomes apparent. When the stress of the plastic shock wave reaches a high enough level, point B overlaps with point C. This point describes the barrier between so-called strong shock and weak shock. In the strong shock regime, there is no elastic precursor wave within the material, only the plastic wave, and the material is thought to behave as a fluid. This regime is obtained through a more extreme version of the "shocking-up" described above, where the plastic shock wave generated has a velocity high enough to overtake the elastic precursor wave [29].

2.5.3 Models for Dislocation Generation within Shock

The earliest investigations into the effect of shock loading on various materials were carried out using ballistic impacts with some form of projectile (e.g. bullets, or ball bearings) [30], or using explosives, the intent behind these early experiments being to investigate how materials react to real world high strain rate impact scenarios, rather than to probe the underlying microstructure response to shock waves. The disadvantage to both bullet projectile and certain types of explosive shock loading are that the shock wave produced in the material tends to be of a more spherical nature, resulting in varying amounts of shear and normal stress throughout the material. In addition, the introduction of release waves without control methods further complicates the picture, making it difficult to draw any but the most macro-scale conclusions from the experiments. This changed with the work of C. S. Smith [4], who introduced the idea of using an explosively driven impact plate and a series of momentum traps to ensure that the sample is only loaded and unloaded by a simple planar shock wave and release wave respectively. This will be discussed in greater detail later. The Smith model for dislocation generation in a shock wave postulated that, for a planar shock wave, a discontinuous elastic wave will propagate through the material until the deviatoric stress, caused by the lattice mismatch between the compressed and uncompressed material, reaches some critical level. At this point, a series of geometrically necessary dislocations (GNDs) will be generated within the shock front in order to compensate for the deviatoric stress. Smith postulated that a pair of dislocations with inclined slip planes moving along with the shock front could accomplish this [4]. A schematic of the Smith model can be seen in Figure 2.6 [4].

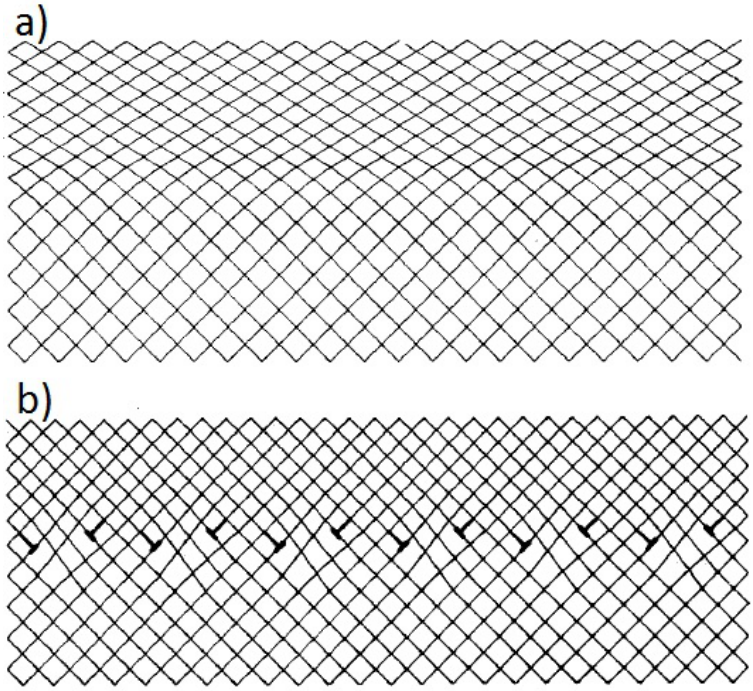

Figure 2.6: *Theory of dislocation generation within a planar shock wave proposed by Smith. a)Uniaxial elastic compression and b) hydrostatic compression [4].*

The Smith model describes a regime in which the material behind the shock wave would be left unchanged by the passage of the shock wave. All previous shock wave work shows that this is far from being the case. Hornbogen [5] suggested a refinement of the Smith model. In this new model, the paired, inclined dislocations postulated by Smith are described as paired dislocation loops. The edge components of these loops would continue moving with the shock wave, while the screw components would remain behind and increase in length as the shock wave propagates. The original schematic for this loop propagation model can be seen in Figure 2.7 [5].

Both the Smith and Hornbogen models rely heavily on dislocations moving with the shock wave, that is to say, the ability of dislocations to move at sonic or supersonic speeds. This proves untenable, as the energy of a moving dislocation becomes infinite as the dislocation's velocity approaches the velocity of transverse elastic waves within the medium [31]. This relativity-like effect would render supersonic dislocations impossible. The existence of supersonic dislocations had been proposed by Eshelby [32], but this

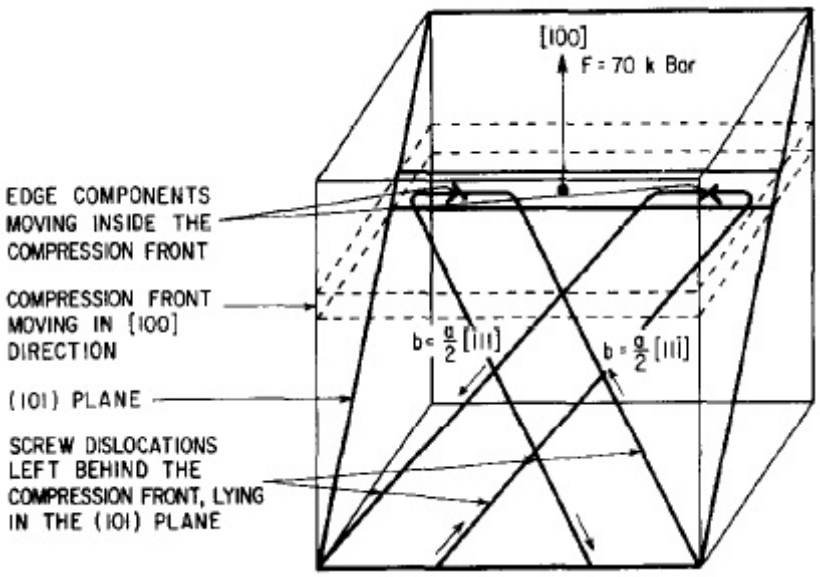

Figure 2.7: *Refinement to the theory of dislocation generation within a planar shock wave proposed by Hornbogen [5].*

remains an issue with the two preceding models. Meyers [6] suggested a further refinement of the original Smith model, which accounts for the two issues discussed above. Meyers' model begins much like Smith's, with deviatoric stresses across a discontinuous planar elastic shock wave leading to the formation of a planar field of paired, angled dislocations. Where the models begin to differ is that in Meyers' model, the dislocations do not travel with the shock wave, but instead remain behind in the deformed material. The planar elastic shock wave then continues on until the deviatoric stresses once more reach a critical level, producing a succession of planar dislocation fronts. The dislocations remaining in the deformed material will then be able to move and interact at subsonic speeds, generating the dislocation structures observed. A schematic of this refined model can be seen in Figure 2.8 [6].

2.5.4 Methods for Shock Loading

There are three main methods used for shock loading samples: laser, explosives and impact. Each has its pros and cons, which will be discussed in this section.

In laser shock a pulsed laser is fired at the sample surface [16]. This vaporises

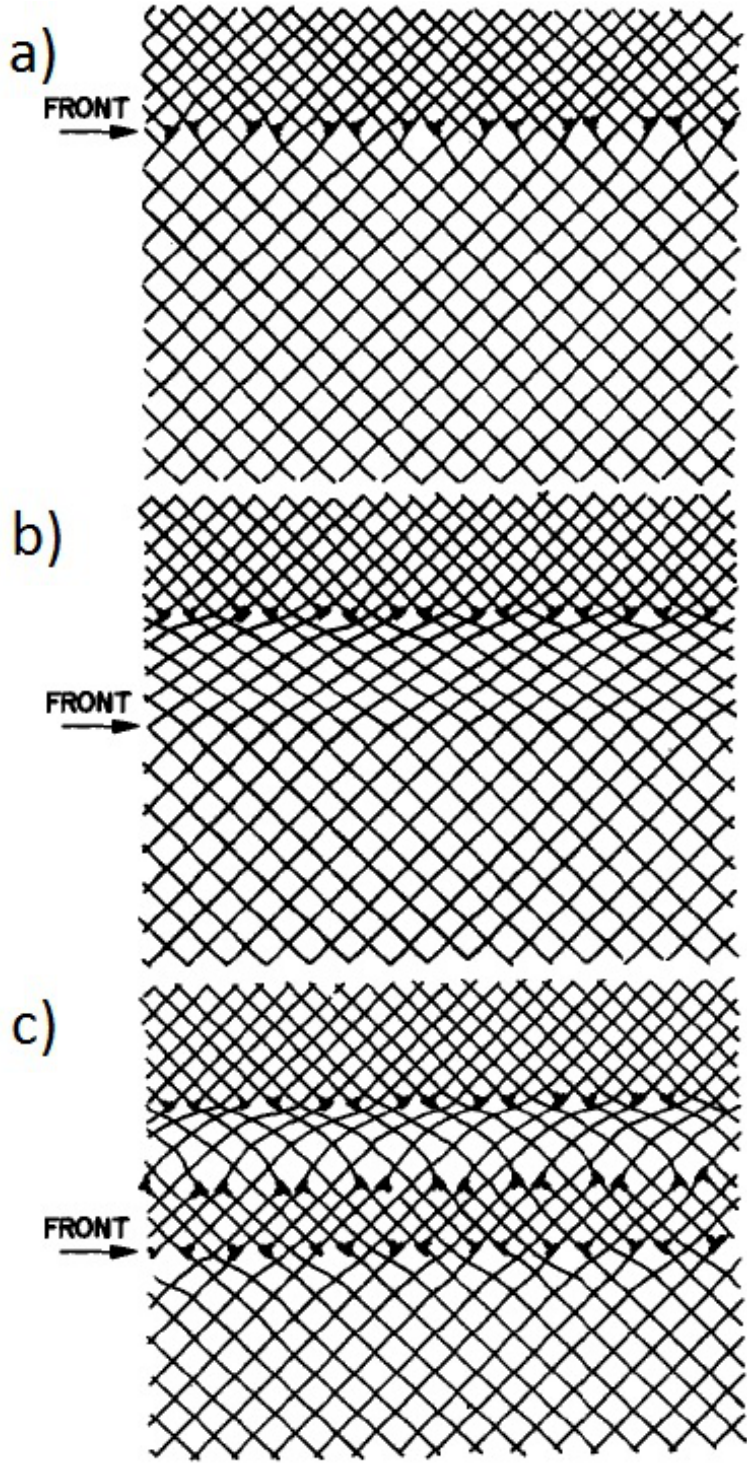

Figure 2.8: *Refinement to the theory of dislocation generation within a planar shock wave proposed by Meyers. a) Dislocation generation plane; b) elastic shock front proceeds, leaving the dislocations behind, and c) successive dislocation generation occurs [6].*

an amount of material from the shocked surface, generating a shock wave within the specimen and leaving a crater in the shocked surface, an example of which can be seen in Figure 2.9a [7]. The advantage to laser shock is that peak pressures as high as 100 GPa can be obtained [7]. In addition, the short pulse duration of the shock wave produced by the laser beam provides access to very rapid deformation conditions. On the other hand, this short pulse duration can be a disadvantage, as many deformation mechanisms require more time to occur. The other disadvantages of laser shock are the spherical wave generated within the material and that the peak pressure observed suffers a large degree of attenuation as seen in Figure 2.9b [7]. This has the effect of complicating the loading experienced by the specimen and can make it more difficult to analyse the shocked material.

When using high explosives to shock load a specimen shaped wave generators are used to detonate explosives adjacent to the specimen and introduce shock waves of the desired configuration. An example of an explosive plane wave generator can be seen in Figure 2.10 [8]. Explosives can be used to load a specimen with a peak shock pressure of tens of GPa. The advantages of explosives are that the experimental setup is simple and relatively cheap. The disadvantages of using high explosives are: that additional safety procedures are required when handling and using explosives; the release waves (discussed in greater detail below) for loading generated by explosives are non-planar in nature, complicating the loading cycle of the specimen; as with the laser shock experiment the peak shock pressure from explosives sees a large degree of atten-

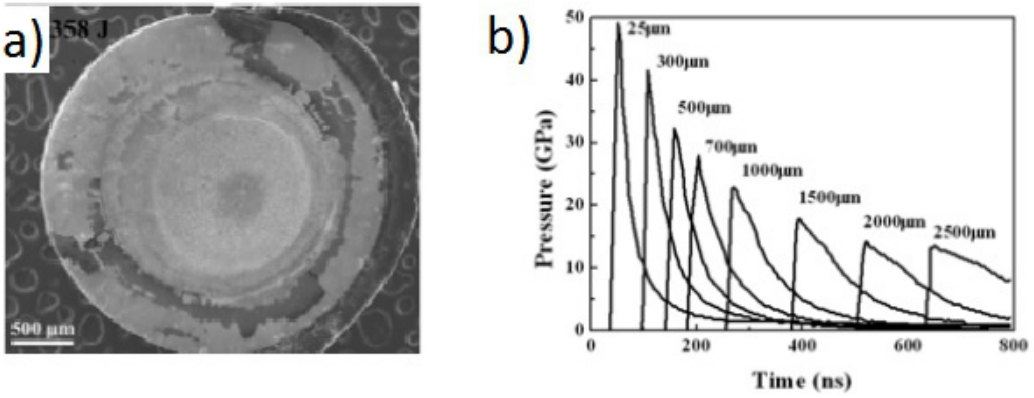

Figure 2.9: *Features from a 358 J laser shock experiment. a) Resultant crater in the specimen surface and b) simulated decay of the pressure pulse generated by the laser [7].*

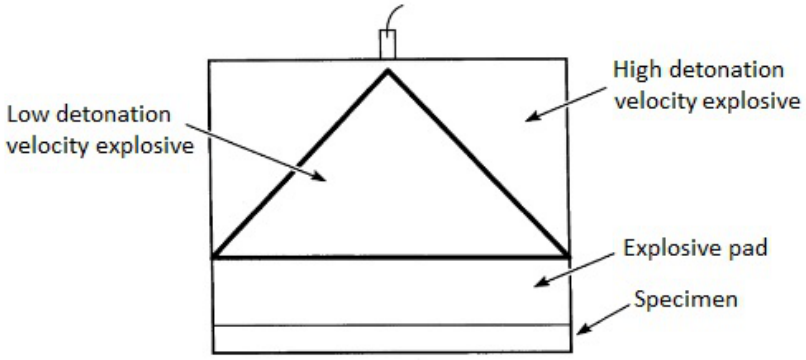

Figure 2.10: *Schematic of an explosive plane wave generator [8].*

uation after entering the specimen, and reproducibility of experiments can be difficult [8].

The final method used to shock load material is to subject the specimen to an impact. This is one of the oldest shock loading methods and at its most straightforward involves firing a small projectile (for example, a metal sphere, or a bullet) into a much larger specimen [33–37]. This has the advantage of simplicity and can be important for testing the real world response to projectile impact. However, as with the laser shock discussed above, the complicated spherical wave produced makes identifying the effects of individual shock factors difficult. In order to simplify the impact experiment a gas gun driven impact plate experiment can be used. In this method, either explosives [38, 39], or a gas gun can be used to propel a flat plate into the front surface of the specimen [40–42]. For the current project a single stage gas gun was used. Double stage gas guns exist that can fire a gun that in turn fires the impact plate. Plate impact is generally considered to be the best way of obtaining a planar shock wave, when combined with a momentum trapping system. Pulse durations produced by plate impact tend to be on the order of 1 μs or greater, although it is possible to reduce this figure by using thinner impact plates. The main disadvantage of the plate impact method is that it is more difficult to obtain the high pressures that the laser shock produces. All specimens under discussion in this thesis were produced using a single stage gas gun, which will be discussed further in a later (experimental) chapter.

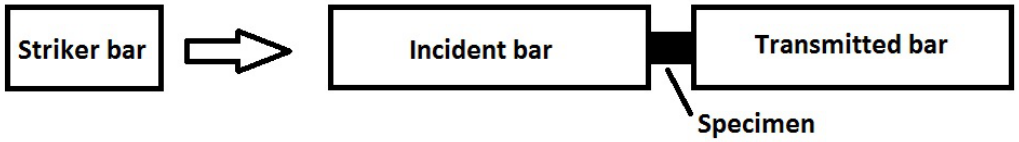

Figure 2.11: *Split Hopkinson pressure bar schematic.*

2.5.5 Split Hopkinson Pressure Bar (SHPB)

An SHPB is an apparatus used for subjecting specimens to strain rates higher than standard compression testing, but lower than those discussed in Section 2.5.4. A typically cylindrical specimen is situated between two straight metal bars, the "incident" bar and the "transmitted" bar. In SHBP compression tests, the incident bar is struck by a "striker" bar fired from a gas gun. A stress wave travels through the incident bar into the specimen, causing plastic deformation before exiting the specimen into the transmitted bar. Strain gauges can be located in both the incident and transmitted bars to determine the loading cycle of the specimen. A schematic of an SHPB can be seen in Figure 2.11.

2.5.6 Relative Length and Time Scales for Different Loading Regimes

All of the loading regimes discussed in this thesis take place over a wide range of length and time scales and subject the specimens to a wide range of peak pressures (or maximum stresses). This section will provide a summary of this range. This is also summarised in Figure 2.12.

At the most extreme end of the scale under consideration in this thesis are specimens shock loaded via gas gun impact. These can experience peak shock pressures on the order of 1–100 GPa over loading times on the order of 1 μs. Loading times lower than this can be generated using thinner impactors, but this can result in a less stable shock wave, hindering reproducibility. With the speed of sound within the materials being on the order of 1000 ms^{-1}, this loading takes place in a compressed region on the order of 1 mm thick, spanning the width of the specimen. The strain rates involved are

on the order of $10^4 - 10^5$ s^{-1}

Specimens loading via an SHPB see maximum stresses on the order of 500 MPa over loading times on the order of 100 μs. With the same wave speeds as gas gun impact experiments, a pulse within the specimen is on the order of 100 mm thick, which is actually longer than the usual length of any specimen that would be loading using an SHPB. The strain rates involved are on the order of 10^3 s^{-1}.

Quasistatic compression generally introduces similar maximum stresses to the SHPB loading, though over substantially longer periods of time. Strain rates between 10^{-3}–10^{-1} s^{-1} delivering a maximum strain of 20% result in total loading times of 2–200 s. As quasistatic compression takes place at strain rates much lower than both gas gun and SHPB impact loading, it makes little sense to consider the length of a "pulse" within the compressed specimens, but the length scales activated within the compressed specimens are several orders of magnitude larger than those in gas gun and SHPB experiments.

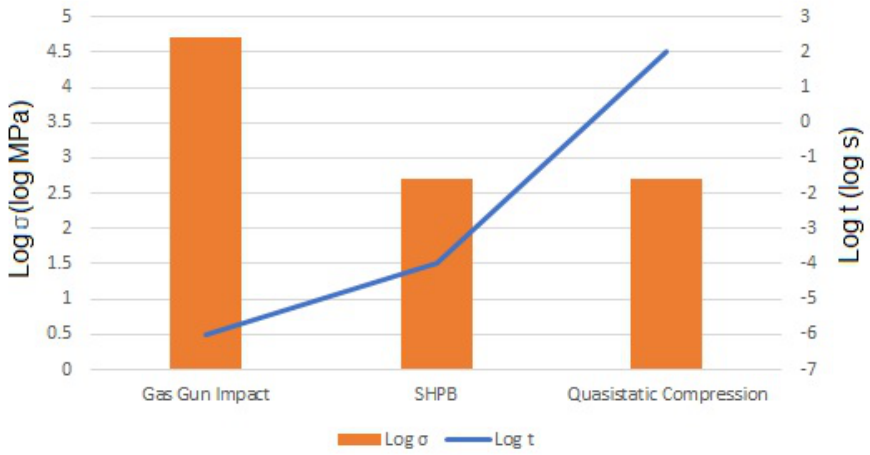

Figure 2.12: *Loading times and maximum stresses experienced during gas gun impact, SHPB and quasistatic compression experiments. In this case, t represents the loading time and σ represents the maximum applied stress during loading.*

2.5.7 Release Waves and Momentum Trapping Apparatus in Plate Impact Experiments

The effect of a shock wave reaching a free surface will now be derived. A cylinder with cross-sectional area A is defined with a wave of width dx incident on a boundary between two volumes A and B. The particle velocity within the wave is U_p and the wave velocity is C with the subscript denoting the volume the wave is occupying. A diagram can be seen in Figure 2.13. Firstly, from conservation of momentum:

$$Fdt = d(mU_p) \tag{2.23}$$

$$\sigma A dt = \rho A \; dx \; U_p \tag{2.24}$$

$$\sigma = \rho \frac{dx}{dt} U_p \tag{2.25}$$

$$\sigma = \rho C U_p \tag{2.26}$$

When the wave interacts with the boundary, there will be formed a transmitted and reflected wave. The stresses associated with the three waves are assumed to be conserved on either side of the boundary, giving the equation:

$$\sigma_I + \sigma_R = \sigma_T \tag{2.27}$$

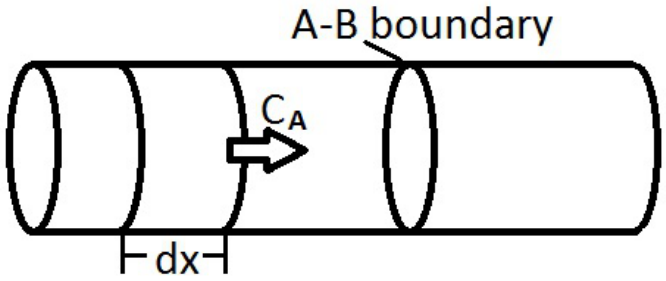

Figure 2.13: *Cylinder with cross-sectional area A with a wave of width dx incident on a boundary between two volumes A and B [3].*

where subscript I refers to the incident wave, subscript R refers to the reflected wave and subscript T refers to the transmitted wave. There is also assumed to be continuity across the boundary, so there will be no overlapping matter or creation of gaps:

$$U_{pI} + U_{pR} = U_{pT} \tag{2.28}$$

The particle velocities can be obtained from Equation 2.26:

$$U_{pI} = \frac{\sigma I}{\rho_A C_A} \quad U_{pT} = \frac{\sigma T}{\rho_B C_B} \quad U_{pR} = -\frac{\sigma R}{\rho_A C_A} \tag{2.29}$$

Substituting Equations 2.29 into Equation 2.28 gives:

$$\frac{\sigma_I}{\rho_A C_A} - \frac{\sigma_R}{\rho_A C_A} = \frac{\sigma_T}{\rho_B C_B} \tag{2.30}$$

which can then be combined with Equation 2.27 and rearranged to give:

$$\frac{\sigma_T}{\sigma_I} = \frac{2\rho_B C_B}{\rho_B C_B + \rho_A C_A} \tag{2.31}$$

and:

$$\frac{\sigma_R}{\sigma_I} = \frac{\rho_B C_B - \rho_A C_A}{\rho_B C_B + \rho_A C_A} \tag{2.32}$$

For a free surface, $\rho_B C_b = 0$, which gives:

$$\frac{\sigma_T}{\sigma_I} = 0 \quad \frac{\sigma_R}{\sigma_I} = -1 \tag{2.33}$$

Similar expressions to Equations 2.31 and 2.32 can be obtained for the particle velocities:

$$\frac{U_{pT}}{U_{pI}} = \frac{2\rho_A C_A}{\rho_A C_A + \rho_B C_B} \tag{2.34}$$

$$\frac{U_{pR}}{U_{pI}} = \frac{\rho_A C_A - \rho_B C_B}{\rho_A C_A + \rho_B C_B} \tag{2.35}$$

Again, for a free surface:

$$\frac{U_{pT}}{U_{pI}} = 2 \quad \frac{U_{pR}}{U_{pI}} = 1 \tag{2.36}$$

It can be seen from Equations 2.33 and 2.36 that upon reaching a free surface a reflected tension wave will enter the material with equal and opposite stress. This is known as a release wave and will act to reduce the pressure in the material back to its starting value.

This free surface interaction can be useful tool for a shock experimentalist. It is very difficult to measure the stresses and strains occurring within a specimen during shock loading, but the rear free surface can provide a window into the rise and fall of the shock wave within the specimen. The technique mostly used for this is known as Heterogeneous Velocimetry (Het-V), or Velocity Interferometer System for Any Reflector (VISAR). Het-V works by using a laser interferometer to measure the rear surface velocity of a shocked specimen. An example trace can be seen in Figure 2.14. By making use of the equations of state derived in Section 2.5.2 the free surface velocity can be converted into a pressure, allowing measurement of the HEL and the peak pressure of the shock wave.

The trace shown in Figure 2.14 is from a shock regime that sees a planar shock wave enter the front surface of a specimen, pass through the specimen bringing it up to the peak shock pressure, followed by a planar release wave originating at the rear free surface of the impact plate. This is a setup that is designed to ensure uniaxial strain throughout the specimen and to ensure that the peak shock pressure and peak pressure loading time is mostly constant throughout the specimen. As the sound speed in the material is dependent on the density of the material, the material compressed by the shock wave will have a higher sound speed than the undeformed material. The release wave will therefore slowly catch up with the shock wave. The change in peak pressure pulse duration over the width of the specimen will be discussed in greater detail in Sec-

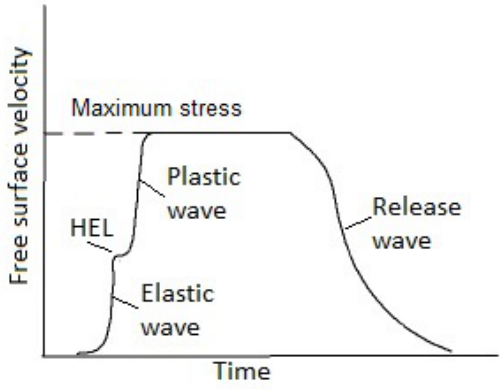

Figure 2.14: *Het-V trace of a specimen during shock loading. First the elastic precursor wave can be seen, followed by the HEL and the "shocking-up" of the plastic wave until the maximum stress is reached. Finally a release wave arrives, reducing the stress within the specimen down to zero.*

tion 4.2. In the context of the loading regime described above, there are two types of release waves that are undesirable. Firstly, when the shock wave reaches the rear surface of the specimen, another planar release wave will be generated. This will have the effect of reducing the peak pressure loading time in the rear half of the specimen substantially, as it will bring that portion of the sample back down to ambient pressure before the release wave from the rear of the impact plate can arrive. This complicates the loading cycle within the specimen. In addition, when the two planar release waves meet, a plane of tension will be set up within the specimen. This is known as the spall plane and can result in voids nucleating in the tension region. In extreme cases, these voids can link together, causing the rear surface of the specimen to separate from the bulk specimen. Secondly, as the shock wave propagates through the specimen, it will interact with the free surface at the sides of the specimen, producing lateral release waves. These will cause the loading regime experienced by the specimen to deviate from the desired uniaxial strain into a more complicated triaxial strain, as well as introducing large variations in the peak pressure pulse duration throughout the entirety of the specimen. In addition, the oblique lateral release waves will subject the specimen to higher shear stresses than a simple planar shock. Work by Pang *et al.* [43] shows that the introduction of lateral release waves can cause twinning nucleation at peak shock pressures below the critical twinning pressure.

These undesired release waves can be prevented from entering the specimen

through use of momentum trapping apparatus. These include spall plates to trap the release wave originating from the rear surface of the specimen and lateral momentum traps to delay the lateral release waves. The momentum traps must be made from material with a good impedance match to the specimen material. When using spall plates, the shock wave will pass through the interface between the specimen and the spall plate and generate the release wave from the rear surface of the spall plate. When this release wave reaches the interface between the spall plate and the specimen, the tension wave will not be transmitted across the boundary and will instead cause the spall plate to accelerate away from the specimen. Lateral momentum traps are close fitting rings of material around the specimen. The purpose of the rings is to delay the lateral release waves. The waves will be generated at the sides of the lateral momentum traps rather than the side of the specimen delaying the lateral release waves. The lateral momentum traps are not free to move in the same way as the spall plate, so cannot completely remove the lateral release wave from the area occupied by the specimen. Instead, the delay of the lateral release waves should ensure that the specimen will have been released by the release wave from the rear surface of the impact plate before the lateral release waves can enter the specimen. The sample will then accelerate ahead of the lateral momentum trapping rings, avoiding the lateral release waves entirely.

The use of momentum traps to produce uniaxial strain was originally pioneered in work carried out by Smith [4]. A schematic of his experimental setup can be seen in Figure 2.15. Subsequent work has seen a refinement of the original equipment, but the fundamental concept remains the same [13, 15, 42, 44, 45].

2.6 Response of Copper and Tantalum to High Strain Rate Loading

2.6.1 Copper

Copper has been shown to exhibit a large degree of strain rate sensitivity. After shock loading, copper specimens display a greater increase in yield strength and hardness than a similar specimen subjected to the same level of strain in a quasi-static manner [41].

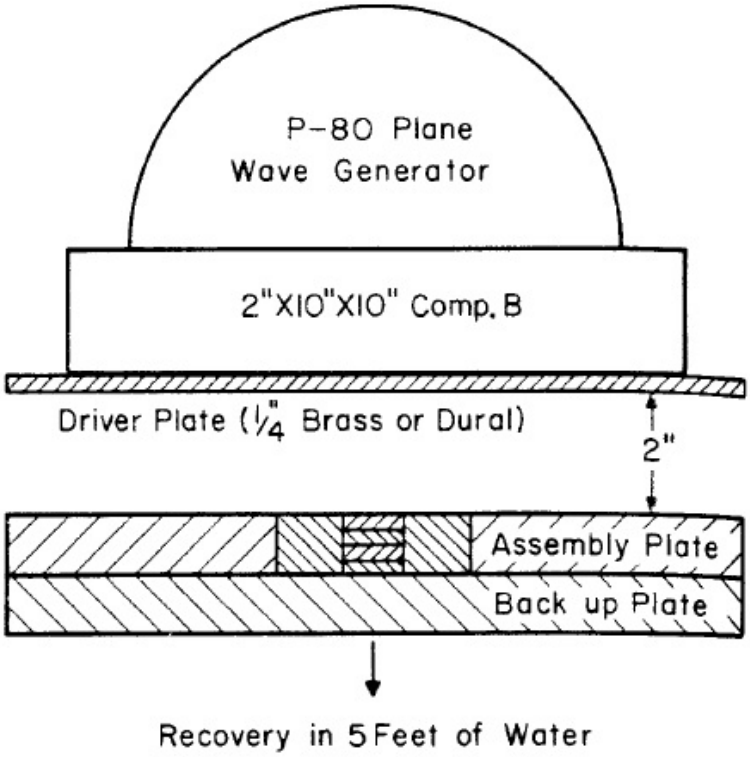

Figure 2.15: *A schematic of the explosively driven impact plate experiment carried out by Smith [4]. Momentum trapping apparatus is present to prevent release waves entering the specimen.*

This is thought to arise from two factors: the relativistic behaviour of dislocations as they approach the speed of sound in the material, as mentioned in Section 2.5.3, prevents dislocations from moving with the shock front and suppresses the extent to which strain can be accommodated by moving dislocations [42]. To compensate for this, a greater number of dislocations will be generated at high strain rates than at the same level of strain at lower strain rates. The high strain rate also has the effect of suppressing dynamic recovery which can act to reduce dislocation density and which is reduced at both high loading rate and under low temperature loading due to reduced thermal activation. This increase in dislocation density increases dislocation interactions and increases the hardness of the material.

The dislocation structure produced by shock loading in copper is very similar to that found in quasi-statically deformed copper, albeit occurring at much lower applied strains after high strain rate loading. Dislocation cells with walls of tangled dislocations and largely empty interiors dominate [41]. The shock pressure threshold for twinning

nucleation at room temperature in copper is between 16-17 GPa, though this increases significantly for grain sizes below 100 μm [16]. This is well above the peak shock pressures under investigation in this work.

2.6.2 Tantalum

In contrast to copper, tantalum displays no strain rate sensitivity under shock loading. The yield stress and hardness of shock loaded tantalum specimens see an increase when compared with the starting material, but this is due to the strain introduced during loading and is not sensitive to the rate at which it occurs [42]. This is thought to be due to the high Peierls stress in tantalum [42]. Dislocation generation and motion will be heavily suppressed by this high Peierls stress at high strain rates and low temperatures. Cross-clip is also inhibited in bcc at high loading rates, which will make the creation of additional dislocation line length difficult, as non-conservative dislocation motion will be limited.

The dislocation structure of tantalum after shock loading is almost identical to that observed after quasi-static loading to the same effective strain. This structure evolution has already been discussed in Section 2.3.2.

2.7 Adiabatic Shear Banding

2.7.1 Introduction

Adiabatic shear bands (ASBs) occur in materials where initially homogeneous deformation, resulting in strain hardening, transitions to more localised thermal softening behaviour. Particularly at high strain rates and in materials with low thermal conductivity and a high thermal softening coefficient, preferential localised deformation results in adiabatic heating (hence the adiabatic part of ASB). The localised heating aids further localised deformation, resulting in the accommodation of any subsequent strain by long thin sheets of heavily deformed material. The surrounding material remains

largely untouched [36]. Other terms commonly used to refer to ASBs are: heat lines, thermal crosses (both used in the context of steel forging) and white etching bands. ASBs have been found in steel [36,46–52], brass [53,54], aluminium alloys [55,56], titanium [10,35,57,58] and its alloys [34,57,59,60], magnesium [37,61] and uranium [62,63]. In addition to these metals, ASBs can also be found in rocks [64], ceramics [65], and explosives [66].

2.7.2 An Historic Overview

The first known academic description of ASBs can be found in the work of Tresca [46], published in 1878, where he describes heat lines produced in iron bars during forging. Work by Zener and Hollomon [47] provided the first 20th century mention of localised strain. They showed that when a negative gradient develops in a stress-strain curve, heterogeneous deformation becomes the preferred response. Their work also lent further credit to the idea that decreased temperature and increased strain rate during deformation have a similar effect on material response.

After their initial identification, the importance of ASBs during deformation became obvious. In some materials, the deformed material becomes far more brittle than the surrounding material, allowing ASBs to act as nucleation sites for cracks and as such play a significant role in crack propagation and ultimately in material failure [67,68]. As steels, and titanium alloys in particular, see large amounts of use in multiple areas of engineering, understanding the microstructure and propagation behaviour of ASBs is of vital importance. On the other hand, a potentially useful application of ASBs emerges from work by Magness [63]. Magness found that projectiles could "self sharpen" through generation of ASBs.

2.7.3 ASB Nucleation, Propagation and Evolution

As mentioned above, an ASB can be said to have formed when homogeneous deformation applied to a material has become localised. This occurs when an increase in strain

results in a localised decrease in material strength. Put another way, the nucleation point of a shear band can be defined as the point on a stress strain curve at which increasing strain is accompanied by decreasing stress. Walley, in his history of shear localisation [69], describes a derivation for determining which factors are important for setting up such a nucleation point. The nucleation point can be defined as:

$$\frac{d\tau}{d\gamma} = 0 \tag{2.37}$$

where τ is the shear stress and γ is the shear strain. If we then assume that τ is only a function of γ, $\dot{\gamma}$ and the temperature (T), then Equation 2.37 can be written as:

$$\left(\frac{\partial\tau}{\partial\gamma}\right)_{T\dot{\gamma}} + \left(\frac{\partial\tau}{\partial\dot{\gamma}}\right)_{\gamma T}\left(\frac{\partial\dot{\gamma}}{\partial\gamma}\right) + \left(\frac{\partial\tau}{\partial T}\right)_{\gamma\dot{\gamma}}\left(\frac{\partial T}{\partial\gamma}\right) = 0 \tag{2.38}$$

Then, we assume that the strain rate remains constant as strain increases, so that:

$$\frac{d\dot{\gamma}}{d\gamma} = 0 \tag{2.39}$$

and also that shear band creation is completely abiabatic, so that the amount of heat generated within the shear band equals the work applied:

$$\rho C dT = \tau d\gamma \tag{2.40}$$

where ρ is the density and C is the specific heat. Substituting Equations 2.39 and 2.40 into Equation 2.38 gives:

$$\left(\frac{\partial\tau}{\partial\gamma}\right)_{\dot{\gamma}T} = -\left(\frac{\tau}{\rho C}\right)\left(\frac{\partial\tau}{\partial T}\right)_{\gamma\dot{\gamma}} \tag{2.41}$$

Equation 2.41 suggests that material with low density and thermal conductivity and a strong link between flow stress and temperature will be prone to ASB nucleation.

Having discussed the material properties that enable the strain localisation that leads to the formation of an ASB, we can now investigate what dictates the location

of the nucleation site. It is logical to assume that pre-existing concentrations of strain would provide favourable sites for ASB nucleation. When discussing this topic, Meyers [9] divided the factors determining these sites into geometrical and microstructural factors. Geometrical factors are macrostructural in nature and derive from the geometry of the specimen and impactor used to generate the ASB. These include strain concentration, where a specific area of the specimen under load will experience a far higher degree of strain (i.e. the hat design and the thick walled cylinder collapse method described in detail below), and inhomogeneity of external loading, where the impactor used is substantially smaller than the specimen. The microstructural factors include four main mechanisms. The existence of a "fractured second phase particle" in a grain will result in strain localisation along the edges of the fracture. Dislocation pile-up at grain boundaries will lead to localised heating in the material, beginning the process of strain localisation in materials with a high thermal softening coefficient. Rotation of grains during strain can lead to geometrical softening, decreasing the local flow stress and initiating strain localisation at the scale of a single grain. Finally, interlens sliding during deformation can result in localised heating. This last mechanism is especially important to the Ti 6Al-4V that will be under investigation in subsequent chapters of this work, due to the beta lath structure and the alpha colony structure. Work by Nesterenko [10] also includes an additional microstructural factor of grain size inhomogeneity, where larger grains in the microstructure will have a lower flow stress than smaller grains. As all of these nucleation factors are preceded by a period of homogeneous deformation, it is clear that the process of strain localisation requires far longer time scales than other deformation features, such as dislocations and twins. The time scales required for ASB nucleation through strain localisation are of the order of 10 μs [13].

With regard to shear band propagation, shear bands are largely macrostructural features, as their size varies from 1-100 μm and they can cut across multiple grains. If a driving force is present and acting on the shear band, as is the case in the hat design and thick walled cylinder collapse method to be discussed, then the progress of the band will be overwhelmingly controlled by these external factors. In the absence of this kind of driving force, the ASB propagation will be controlled by the microstructural factors listed above. The front of the ASB will move from favourable condition to favourable condition, following the path of least resistance through the material.

Following on from the topic of propagation is the subject of ASB evolution. How does the shear band develop as it accommodates a larger amount of shear strain? Nesterenko [10] breaks down the evolution of the ASB into three phases. Phase 1 is the initial localisation and applies both to the initial ASB nucleation point and also to the area at the very tip of the propagating ASB. In this phase, strain localisation will occur, driven by the geometrical factors described above. These points of strain localisation will initially be a series of discrete instances of localised strained material, before they expand and connect to form a unified band of deformed material in Phase 2. Phase 2 consists of highly strained material, with elongated grains aligned in the direction of ASB propagation. As mentioned above, the highly localised strain results in a localised temperature increase in the material. This then leads to Phase 3, which is the recrystallization of the highly deformed material into a nano-grain structure [52].

2.7.4 Methods of ASB Generation

Previous methods of generating ASBs have been: high rate machining [24, 25, 70] and compression [62], thick walled cylinder (TWC) collapse by use of explosives [10, 50, 57], cold-rolling [53, 54, 56, 71], and high velocity impacts. This last category can be further broken down into: ballistic impact [34–37, 72] and forging [46], where the impactor is often a spherical or cylindrical projectile impacting a much larger specimen; split Hopkinson pressure bar (SHPB) [52, 55, 59, 60, 67, 68] and gas gun impact, where a high strain rate load is applied by a flat impactor to a specimen smaller than the impactor, and the use of so-called "hat shaped" specimens [9, 60, 73], where a target specially shaped to generate ASBs is subjected to high rate loading by an impactor.

Recreation of Real World Conditions

As described above, some of the oldest investigations into ASBs were concerned with their creation during real world applications. These include high rate machining [24, 25, 70], cold-rolling [53, 54, 56, 71], ballistic impact [34–37] and forging [46]. These types

of experiments are at their most useful when the aim of the experiment is to answer a specific practical question. How does armour of this specific alloy respond to a ballistic shot test? How does this particular metal respond to a specific set of forging conditions? These questions are important ones and answering them is vital to explaining and ascertaining the suitability of materials for a range of practical applications. However, the loading conditions present in this type of experiment are, by virtue of being a recreation of real world conditions, complicated. This makes it more difficult to isolate the factors leading to the creation of specific ASBs. It is for this reason that we turn to experiments that apply a simpler loading cycle.

Hat Shaped Specimens

The hat shaped specimen was designed by Meyer and Manwaring [73]. A schematic of the hat shaped specimen can be seen in Figure 2.16 [9]. The specimen is designed to

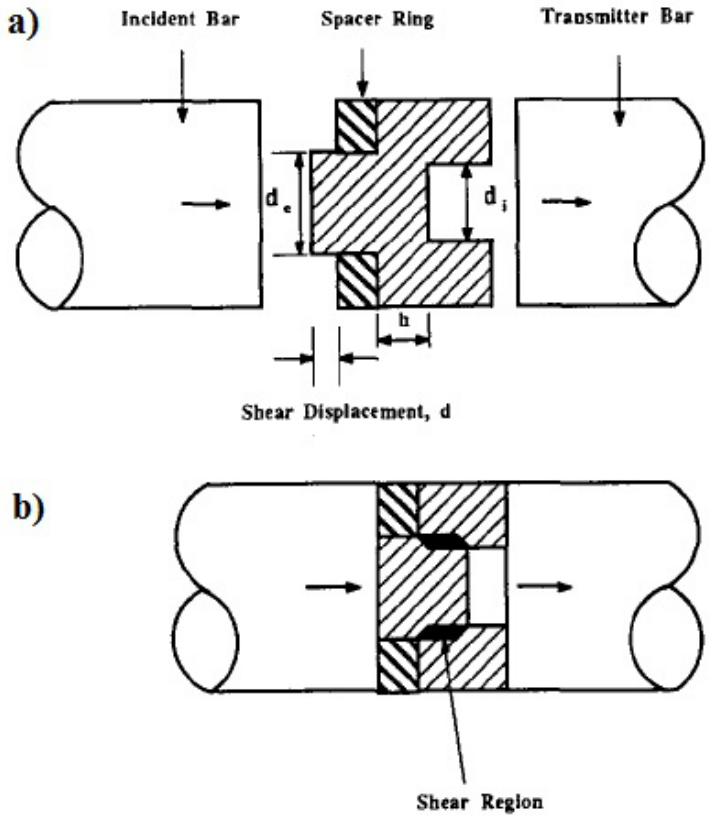

Figure 2.16: *Hat shaped specimen schematic a)before and b) after testing in an SHPB [9].*

apply simple shear stress to the deformed region in the specimen. The most commonly used impactor in this experiment is the SHPB, as demonstrated in Figure 2.16. A spacer ring can be used to control the total displacement experienced by the specimen during impact. The plastic shear strain τ experienced by the specimen can be approximated as:

$$\tau \approx P\left[\pi h\left(\frac{d_i + d_e}{2}\right)\right] \tag{2.42}$$

where P is the load, d_i and d_e are the internal and external diameters respectively and h is the length of the shear region. The main advantages of the hat shaped specimen are that the strain applied in the region of interest is close to pure shear and ASBs will always occur in the same region, making them far easier to locate.

The main disadvantage of the hat shaped specimen is the complicated stress and strain distribution in the shear region and the relatively complicated geometry of the specimen. The outcomes of hat shaped specimen experiments are strongly influenced by the specimen geometry, so a larger degree of care must be taken in specimen formation to ensure repeatability [74].

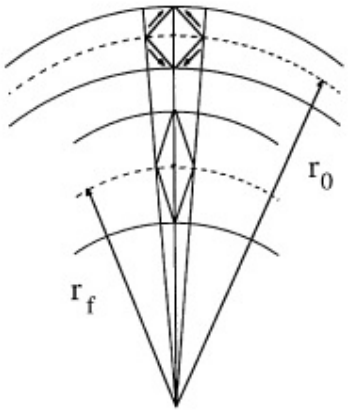

Figure 2.17: *Deformation of a unit cell within the TWC as the cylinder collapses. r_0 and r_f are the starting and final radii of a reference point within the TWC respectively [10].*

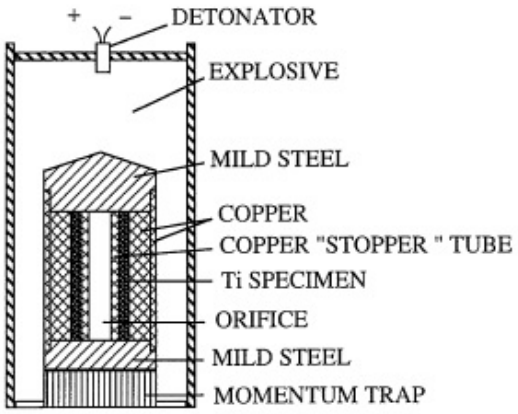

Figure 2.18: *Schematic of a titanium TWC collapse experiment using explosives [10].*

Thick Walled Cylinder (TWC) collapse

The TWC collapse method was invented by Nesterenko *et al.* [75] as a method of generating multiple ASBs by the radial implosion of a cylindrical specimen. A thick walled cylinder is subjected to inward radial stresses, causing the cylinder to collapse, reducing the radius of the cylinder. The stress is ideally applied solely in the radial direction, with no applied stresses acting along the z-axis of the cylinder. Figure 2.17 [10] demonstrates the strain applied to a unit cell in the TWC during cylinder collapse. As the radius of a reference point within the TWC moves from the initial radius r_0 to a final radius r_f, the internal surface of the TWC experiences the greatest shear stress and will be the site of ASB nucleation. As the planes of maximum shear lie at 45° to the radius of the TWC, a propagating ASB will curve from the internal surface towards the same 45° angle.

The effective strain ϵ_{ef} experienced by this specimen is given by:

$$\epsilon_{ef} = \frac{2}{\sqrt{3}} ln \left(\frac{r_0}{r_f} \right) \tag{2.43}$$

The usual method for initiating TWC collapse is the use of explosives. An example schematic making use of a titanium sample can be seen in Figure 2.18 [10]. After the explosives are detonated, the TWC will be subjected to cylindrical stresses that should be applied to the entire outer surface of the TWC almost simultaneously. There will be a slight delay between loading at the "top" of the specimen and the "bottom" as de-

picted due to the transmission speed of the detonation signal, but this will be negligible. The internal copper stopper tube is used to limit the collapse of the TWC to ensure the desired ϵ_{ef} is obtained. A solid copper rod can also be inserted within the stopper tube to prevent its collapse along with the specimen, but this can lead to disruption of the final shear band structure due to collision between the copper rod and the specimen internal surface [10].

2.7.5 ASBs in Titanium 6Al-4V

Having derived the material properties that can lead to the nucleation of shear bands in Section 2.7.3 it becomes clear that the low thermal conductivity and high thermal softening coefficient of titanium 6Al-4V make it an ideal candidate for ASB nucleation. Its widespread use also means that understanding how it responds to high strain rates and the introduction of a major precursor to failure is vitally important.

Me-Bar and Shechtman [72] carried out some of the first work investigating ASB nucleation in titanium 6Al 4V. They induced ASB formation by ballistic impact. The characteristic fine grain structure was produced, with no notable texture. Evidence of phase transformation was discovered, from which it was concluded that the temperature achieved by the ASB was around the β transition point of 950°C. It was found that the final structure within the ASBs was completely independent of the starting structure of the material and was concluded to be a product of the high cooling rate within the ASBs. The complicated loading regime applied by the projectile resulted in a complicated series of shear band networks with the observation made that a series of ASBs would have been generated through the loading process, with only the final state of the material observable. Grebe *et al.* [76] followed this work soon after with an impact test using a more refined ballistic projectile and confirmed many of the conclusions of Me-Bar and Shechtman. They confirmed the existence of large amounts of deformation near the ASBs and a sub-micron grain structure within the ASBs. Voids were also detected within the ASBs, reaffirming their place as sites for crack nucleation. Timothy and Hutchings [34] impacted their specimens with steel spheres. In contrast to Me-Bar and Schechtman, they found the ASB structure to"consist of zones of intense shear defor-

mation of the original microstructure, modified by the effects of elevated temperature", but no phase transformation was detected.

Moving away from the ballistic impact method, Nesterenko *et al.* [10] made use of the TWC collapse method in order to investigate the nucleation and propagation of ASBs as one interlinked system within the specimen, rather than observing individual ASBs. They compared the theoretical models of Grady and Kip [77], and Wright and Ockendon [78] to experimental results. Both the Grady-Kipp and Wright-Ockendon models used the age-old approximations of one dimensional shearing of an infinite strip of material, so as to avoid complications from boundary effects. In the Grady-Kipp model, postulated for rate independent materials, it was proposed that the rapid loss of strength experienced by the material during the creation of an ASB forces the surrounding material to unload. This unloading travels through the material and the minimum ASB separation is given by the distance traveled by the unloading front during the time required for localisation to occur at the theoretical minimum distance. The rationale for this being that the unloading front removes the stress needed for an ASB to occur, so a pre-existing ASB will suppress subsequent ASB nucleation within this minimum separation. The separation L_{GK} is given by the equation:

$$L_{GK} = 2\left(\frac{9kC}{\dot{\gamma}^3 a^2 \tau_0}\right)^{\frac{1}{4}} \tag{2.44}$$

where k is the thermal conductivity; C is the heat capacity; $\dot{\gamma}$ is the shear strain rate; a is a softening term, and τ_0 is the strength at a reference temperature.

The Wright-Ockendon model applies to rate dependent materials and postulates that the ASBs grow from perturbations in an initially uniform stress field. They found the wavelength that would result in the fastest growing perturbation and took this as the ASB separation. The separation L_{WO} is given by the equation:

$$L_{WO} = 2\pi\left(\frac{kCm^3\dot{\gamma}_0^m}{\dot{\gamma}^{3+m} a^2 \tau_0}\right)^{\frac{1}{4}} \tag{2.45}$$

where m is the strain rate sensitivity and τ_0 is the strength at a reference tem-

perature and reference strain rate $\dot{\gamma}_0$. Nesterenko *et al.* [10] concluded that the two models, despite treating the ASB separation problem very differently, actually produced very similar solutions, with the main differences being the lack of strain rate sensitivity in Grady-Kipp and the numerical factors involved. Wright-Ockendon produced values one sixth as large as Grady-Kipp. Both models were in agreement with experimental results within one order of magnitude, though the Wright-Ockendon model provided a closer match. This means that it is most likely that the distance between ASBs is set during the initial formation of the ASBs, rather than as a result of interactions between fully or mostly formed ASB and the surrounding material.

Chapter 3

Experimental procedure

A series of copper, tantalum and titanium 6Al4V specimens was subjected to various loading regimes at differing stresses and strain rates. The micro-structural and mechanical properties of the specimens were then investigated pre- and post-strain.

3.1 Specimen Preparation

3.1.1 Plate Impact Shock Loading

Copper and tantalum specimens were subjected to plate impact shock loading. The copper specimens had either been annealed or subjected to a reduction in thickness of 20 %. The tantalum specimens were either as-received tantalum from the supplier, or had been subjected to an additional reduction in thickness of 50 %. The initial microstructures of both sets of starting materials will be discussed in greater detail in Section 4.1.

The shock loading of the material specimens was undertaken by the AWE, using a single stage, 70 cm bore, 3 m gas gun. Pictures of the gas gun can be seen in Figure 3.1. A summary of the shock tests, including the plate impact speeds and the peak pressures that resulted, appears in Table 3.1. The specimens were discs with a thickness of 5 mm. The copper specimens had a mean diameter of 35 mm and the tantalum specimens had a mean diameter of 30 mm. The thickness of the impact plate varied between 'shots' and was selected to give a peak shock pulse duration of 1 μs.

Sample	Pre-shock work	Material	Impact velocity (ms^{-1})	Peak shock pressure (GPa)	Momentum apparatus
A Cu 5.08	Annealed	Copper	275	5.08	Thick spall
CR Cu 5.96	Cold-rolled	Copper	320	5.96	Thin spall
CR Cu 5.87	Cold-rolled	Copper	315	5.87	Cup
CR Cu 9.60	Cold-rolled	Copper	499	9.60	Cup
AR Ta 7.20	Residual strain	Tantalum	237	7.20	Thick spall
CR Ta 7.20	Cold-rolled	Tantalum	231	7.20	Thick spall

Table 3.1: *Shock test details.*

Momentum trapping rings and spall plates were used for all of the tests. Three different designs were used: (i) three spall plates, all 1 mm thick (referred to as the thin spall plate apparatus); (ii) two thin spall plates 1 mm thick with one larger plate 5 mm thick (referred to as the thick spall plate apparatus), and (iii) a cup structure around the specimen in place of the first spall plate and first momentum trapping ring (referred to as the cup apparatus). A schematic of the thin spall apparatus and the cup apparatus can be seen in Figure 3.2.

The momentum trapping apparatus was mentioned in Section 2.5.7. In the absence of the momentum traps, release waves would be generated at every free surface that the shock wave comes into contact with. These release waves reduce the stress within the specimen to ambient levels. Allowing release waves to enter a specimen from the sides of the specimen and from the rear of the specimen would complicate the loading cycle and was undesirable for this experiment. The spall plates act to prevent the release wave from the rear surface of the apparatus from entering the specimen. As

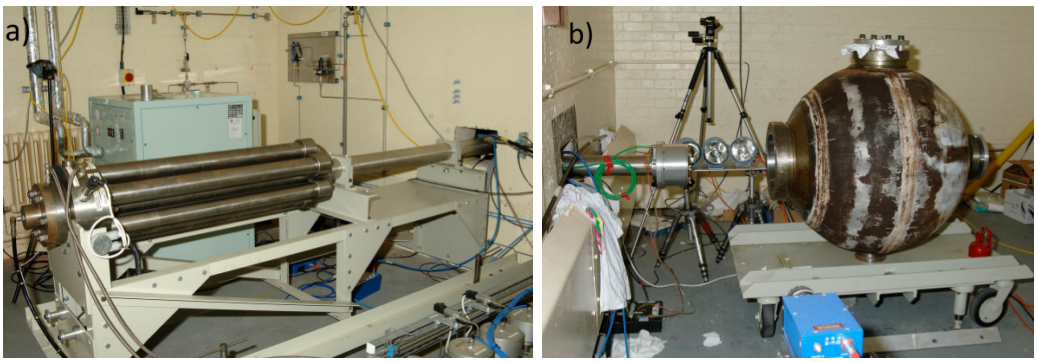

Figure 3.1: *Single stage gas gun: a) breech, b) recovery chamber.*

the release wave (which is a tension wave) reaches the boundary between two plates, the plates will separate. A single plate is not sufficient to fully trap all of the release wave and so multiple plates are used. The momentum trapping rings ensure that the lateral release waves are generated at the edge of the momentum trapping rings. This delays the lateral release waves entering the specimen until the release wave from the rear surface of the impactor has fully unloaded the specimen and the specimen has exited the momentum trapping apparatus. With the momentum trapping apparatus in place, the specimen should be loaded by a simple planar shock wave and unloaded by a simple planar release wave. The thickness of the impactor is calculated so that the time between loading and unloading the specimen is 1 μs.

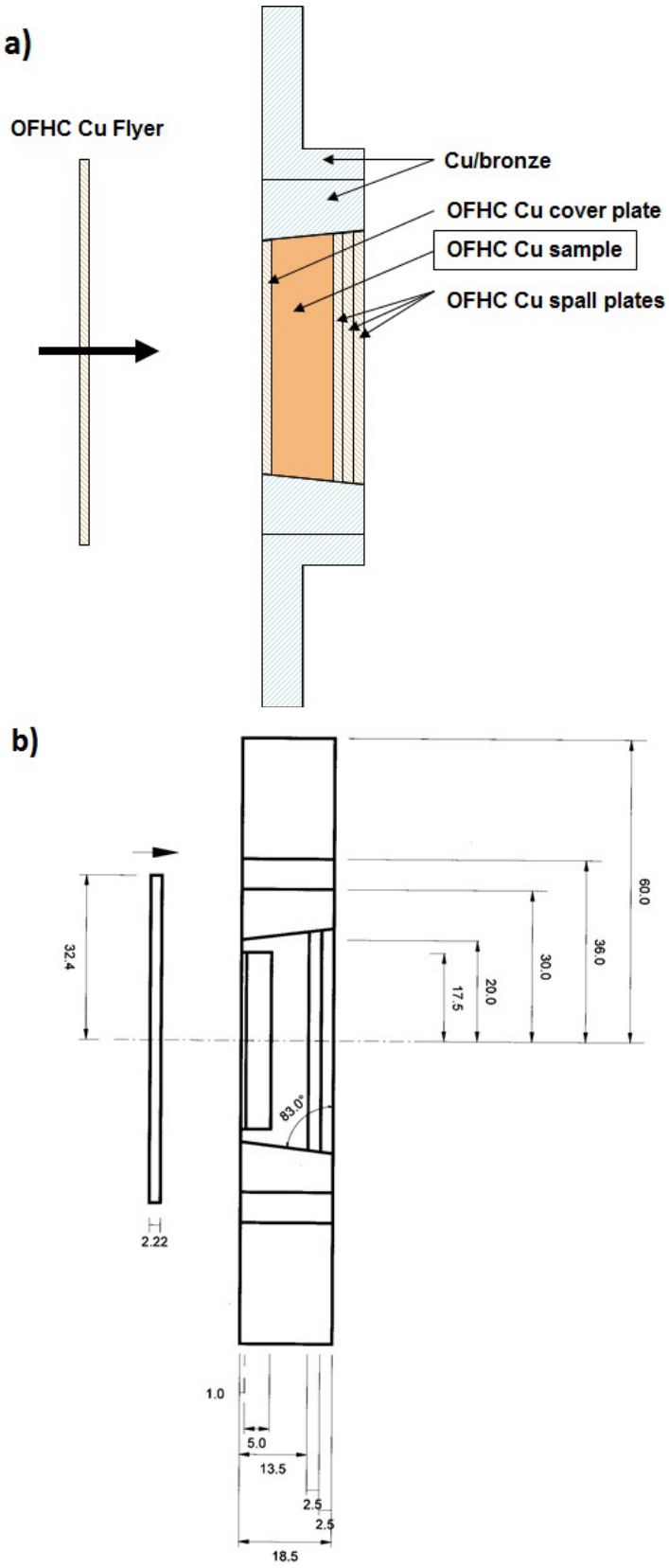

Figure 3.2: *Momentum trapping apparatus schematics for the: a) thin spall apparatus and b) cup apparatus. All dimensions and materials referenced are for the oxygen free high conductivity copper (OFHC Cu) specimens. All dimensions are given in millimetres.*

3.1.2 Tantalum Compression and Split Hopkinson Pressure Bar (SHPB)

These tests were carried out by Dr. Alex Worley (at the time a PhD student), Dr. Paul Hooper and Prof. John Dear of the Department of Mechanical Engineering, Imperial College London with the assistance of Dr. Jeremy Millett and Mr. Glenn Whiteman of AWE, Aldermaston. A series of five tantalum samples was machined from the residual strain material described above and compressed. The compression specimens were cylinders 4.55 mm in diameter and 4.40 mm in length. This was carried out at strain rates of 10^{-1} s^{-1} and 10^{-3} s^{-1} in quasi-static compression and at a strain rate of 2×10^{3} s^{-1} using a split Hopkinson pressure bar (SHPB) as described in Section 2.5.5. The quasi-static compression was also carried out at -40°C, 20°C and 170°C. The quasi-static compressed specimens were subjected to 70 % strain and the SHPB specimen was subjected to 20 % strain. Table 3.2 summarises the strain rates and temperatures used for each specimen.

Sample	Strain %	Strain rate (s^{-1})	Temperature (°C)
Ta-120	70	10^{-1}	20
Ta-320	70	10^{-3}	20
Ta-140	70	10^{-1}	-40
Ta-1170	70	10^{-1}	170
Ta320	19	2×10^{3}	20

Table 3.2: *Compressed tantalum specimens*

3.1.3 Thick Walled Cylinder Collapse

In order to generate adiabatic shear bands (ASBs), a TWC made of titanium 6Al4V (Ti6-4) was shock collapsed using the 100 mm bore gas gun at the Institute of Shock Physics, Imperial College, London. The cylinder was 200 mm long, with an inner diameter of 23 mm and a wall thickness of 4 mm. This was machined from rolled Ti6-4 bar stock, with the z-axis of the cylinder parallel to the axis of the bar stock. The collapse was achieved by firing a shaped, polycarbonate projectile into a stainless steel confining cylinder containing both the Ti6-4 TWC and a complementarily shaped copper infill. A schematic diagram of this setup can be seen in Figure 3.3. The curved surface of the

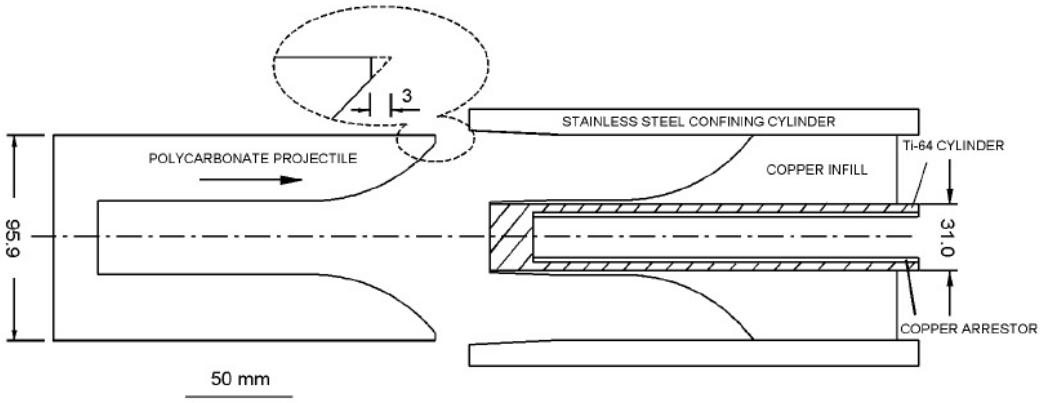

Figure 3.3: *Schematic of the thick walled cylinder collapse apparatus.*

impact face generates shock waves after impact that apply the radial stress necessary to collapse the TWC in a purely radial direction. Simulations carried out by Winter *et al.* [11] found that the collapse of the TWC would not be constant along its entire length, as shown in Figure 3.4. The specimen under investigation in this thesis was obtained from the most highly strained section of the collapsed TWC. A copper arrestor pipe with a wall thickness of 1 mm was inserted into the TWC to limit the cylinder's collapse and achieve a final strain of 0.34.

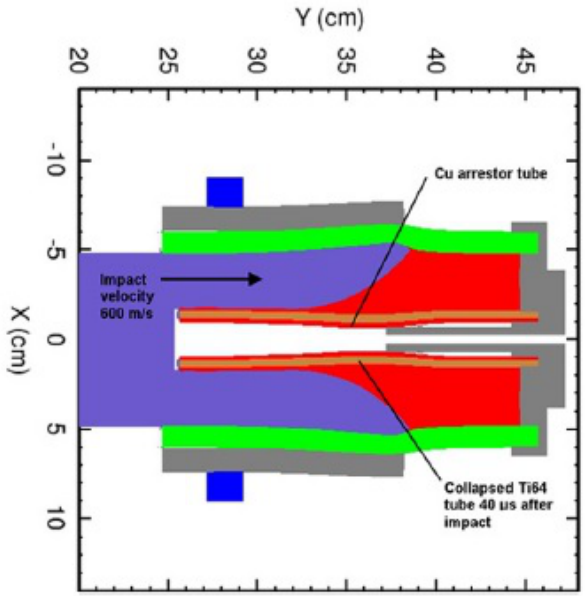

Figure 3.4: *Simulated response of the TWC collapse specimen 40μs after impact at 600 ms^{-1} [11].*

3.2 Sample Preparation and Analysis

All sectioning of the samples described in the following section was carried out using electrical discharge machining (EDM) to reduce the amount of additional strain introduced into the material.

3.2.1 Transmission Electron Microscopy and Scanning Transmission Electron Microscopy

Characterisation of all samples using 2-beam conditions was carried out on a JEOL 2100 LaB6 TEM at 200kV. Two beam conditions are obtained by tilting the TEM sample until only the straight-through beam and one diffracted beam are excited in a diffraction pattern. A bright field image is then obtained from this two beam condition diffraction pattern. Imaging by STEM of the compressed and shock loaded tantalum samples and the EDS analysis of the Ti6Al-4V samples was carried out on an FEI Tecnai F20 at 200kV. High angle anular dark field (HAADF) imaging was used when imaging the tantalum samples to remove bend contours from the images. EDS was used to map the distribution of aluminium and vanadium in the Ti6Al-4V adiabatic shear band samples in order to determine the features of the beta phase grains present.

Plate Impact Samples

TEM samples were prepared from the plate impact shocked specimens by first sectioning thin slices from the specimens and then trepanning 3 mm diameter discs from these slices. The discs were ground to a thickness of $\sim$200 μm and an electron transparent area generated by twin jet electropolishing. A solution of 33 % nitric acid and 66 % methanol was used for the copper samples and a solution of 4 % hydrofluoric acid, 10 % sulphuric acid and 86 % ethanol for the tantalum. The sample disc normals were chosen to be parallel to the shock loading direction in all cases.

Compressed Tantalum

Due to the small size of the compressed tantalum specimens, focused ion beam (FIB) milling was used to produce TEM samples. The samples were taken from the centre of the specimens, with the foil normal perpendicular to the loading direction. A schematic of the FIB sample orientations can be seen in Figure 3.5.

TWC Collapsed Ti6Al-4V

To ensure that the TEM samples contained the ASBs, the bulk specimens were etched in Kroll's reagent before milling to ensure easy identification of the ASBs. FIB milling was also used to produce TEM samples for the shock collapsed Ti6Al-4V. Samples were produced with foil normals parallel to the direction of propagation of the ASB and the radial axis of the TWC, and also with normals perpendicular to the propagation direction and parallel to the z-axis of the TWC. A schematic detailing the orientations of the TWC collapse FIB samples can be seen in Figure 3.6.

3.2.2 Scanning Electron Microscopy

After sectioning and mounting in bakelite, all SEM samples were ground using "wet and dry" silicon carbide papers of grades 800 to 2400. Following this, the samples were polished using diamond suspensions with grain sizes 6 μm, 3 μm and 1 μm. Finally they were subjected to polishing with OP-S polishing solutions for 40 minutes. The tantalum and Ti6Al-4V samples required the use of an activated solution of 96% OP-S, 2% NH_3

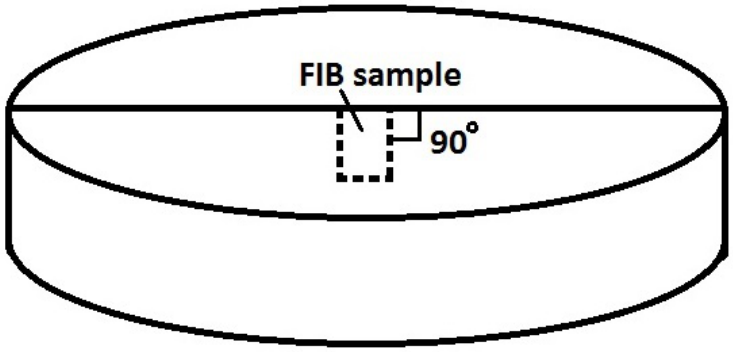

Figure 3.5: *Schematic detailing the orientations of the FIB samples taken from the compressed tantalum specimens. The FIB sample depicted is not to scale.*

and 2% H_2O_2, while the copper samples did not.

This polishing recipe was used to produce samples capable of generating a high indexing rate for electron back scattered diffraction (EBSD). For other techniques, such as hardness testing and prior to etching for use in SEM imaging, some of the later stages were removed to save time.

For SEM imaging, copper samples were etched in a solution of 50% nitric acid and water and Ti6Al-4V was etched in Kroll's reagent (2% HF, 10% HNO_3 and 88% H_2O). The etched samples were characterised at 15kV. EBSD analysis was carried out on all of the plate impact samples and all of the compressed tantalum samples using these beam voltages. All FIB samples produced were analysed using transmission Kikuchi diffraction (TKD) using a beam voltage of 30 kV.

All the scanning electron microscopy was carried out using a Tescan MIRA3 FEG SEM.

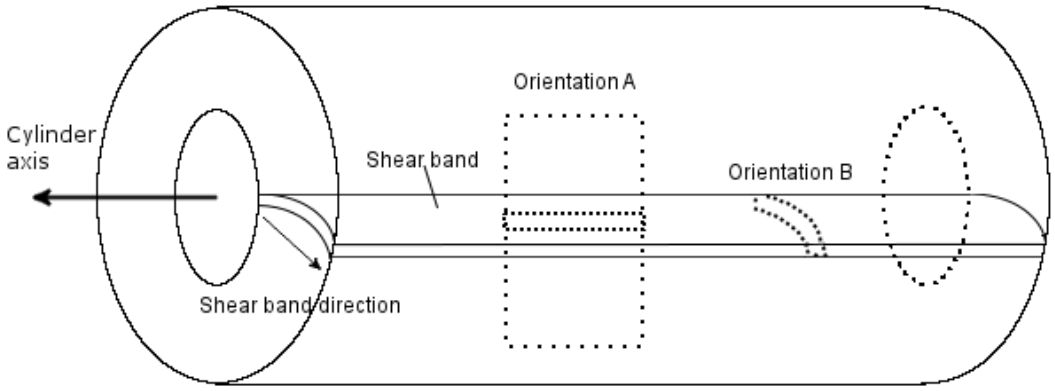

Figure 3.6: *Schematic detailing the orientations of the FIB samples taken from the TWC collapse specimen. The FIB samples depicted are not to scale.*

3.2.3 Hardness Testing

In order to test the efficacy of the momentum trapping apparatus used during the shock tests, hardness profiles were generated for the plate impact shock loaded copper and tantalum samples. The expected result was that if the specimens had seen loading by a simple planar shock wave, followed by a simple planar release wave, then the hardness response of the material should be largely uniform throughout the specimen. The specimens were sectioned to expose the cross-section. These samples were then polished using the same recipes as described in Section 3.2.2. A series of hardness measurements was taken with data points beginning 100 μm from the impact surface and moving towards the rear of the sample at intervals of 100 μm. Each data point was an average of 10 individual measurements. These measurements were taken using a peak force of 0.2 N on a Struers DuraScan.

When testing the hardness of the unshocked material (annealed copper, cold-rolled copper, residual strain tantalum and cold-rolled tantalum), 100 individual measurements were made in a square configuration and averaged. Due to the necessity of avoiding specimen edges with the indenter, measurements of the impact face of the shocked specimens were also obtained using 100 individual measurements taken parallel to the shock loading direction.

The compressed tantalum samples listed in Table 3.2 were subjected to full hardness mapping, with hardness measurements taken every 500 μm in both the x- and y-directions.

3.2.4 Compression Testing

Samples for compression testing were taken from: annealed copper, cold-rolled copper, residual strain tantalum, cold-rolled tantalum and all of the plate impact shock loaded specimens. Samples from the shocked specimens were taken from as close to the centre of the disc as possible. The compression samples were cylinders measuring 4.63 mm in diameter and between 4.3 and 5.0 mm in the z-direction. The samples were subjected to 20 % strain at a rate of 10^{-3} s^{-1}.

Chapter 4

The Effect of Pre-Shock Cold-Rolling on the Post-Shock Behaviour of Copper and Tantalum

4.1 Results

A series of plate impact experiments were carried out on annealed and cold-rolled copper and as-received and cold-rolled tantalum. These experiments were carried out in order to determine the effect of cold-rolling on the high loading rate response of two materials that display very different behaviours under high strain rate loading. The TEM investigation was undertaken to determine the difference between the post-shock microstructure of copper and tantalum with and without pre-shock cold-rolling. The compression tests described in the previous chapter were undertaken to investigate the effect of cold-rolling on the strain rate sensitivity of copper and tantalum. Hardness tests were carried out to confirm that the momentum trapping apparatus had been successful at preventing additional release waves from entering the shock loaded specimens. However, unexpected features in the hardness profiles necessitated further investigation into the variation in the shock loaded material along the loading direction. The thickness of the impactors used were calculated to produce peak pulse durations of 1 μs in all of

Hardness

Hardness values for the unshocked specimens were averaged from 100 individual measurements. Hardness profiles were taken for the shocked specimens, beginning at the impact face at intervals of 0.1 mm with each data point being the average of 10 individual measurements. All measurements were taken using a 0.2 kg load. A summary of the samples tested with average hardness values, or hardness ranges where appropriate can be found in Table 4.1. The experimental uncertainty quoted is the standard deviation of the hardness measurements that were averaged to produce the associated hardness value.

Cold-rolling the copper resulted in a 79% increase in hardness. The post-shock annealed specimen showed a 49% increase in hardness, whereas the post-shock cold-worked samples showed only a 7% increase at similar peak shock pressures. Increasing the peak shock pressure by 60% resulted in an increase in hardness of only 10%.

Hardness maps covering a quarter of the impact surface and rear surface of the annealed copper shock loaded to a peak pressure of 5.08 GPa, and the cold-rolled copper shock loaded to 5.96 GPa and 9.60 GPa were produced to investigate the possibility of inhomogeneities in the hardness of the specimens. χ^2 tests were carried out on the results from the hardness maps. The hypothesis used in the χ^2 test was based on the assumption that the hardness is constant throughout the measured surface and that this hardness is equal to the average hardness in that surface. The χ^2 values for all measured faces were unity, showing perfect agreement with the expected value. This shows that

Annealed\ Cold-Rolled	Peak Shock Pressure (GPa)	Vickers Hardness (HV)	Experimental Uncertainty (HV)	χ^2 Value from Hardness Map
Annealed	0	50.8	3.2	1
Annealed	5.08	71.5-79.9	2.9	1
Cold-Rolled	0	91.0	4.7	1
Cold-Rolled	5.87	92.5-101.5	3.5	1
Cold-Rolled	5.96	97.2	3.9	1
Cold-Rolled	9.60	99.7-114.5	4.5	1

Table 4.1: *Vickers hardness measurements of annealed and cold-worked copper, both shocked and unshocked. For specimens where a range is presented, the hardness varied through the specimen thickness.*

the schocked specimens. Any variations in this peak pulse duration will be discussed in Section 4.2.

4.1.1 Copper

Starting Material

The microstructure of the copper before cold-rolling and/or shock loading can be seen in Figure 4.1a. The microstructure observed in the annealed material shows almost no dislocations, or contrast features resulting from residual strain in the material.

The cold-rolled copper shown in Figure 4.1b was obtained directly from a supplier by AWE, so the exact degree and type of loading that the material had been subjected to was unknown. The assumption has been made that it has experienced a reduction in thickness by rolling of approximately 20%. The microstructure consists of equi-axed dislocation cells, with thick walls of tangled dislocations and cell interiors free of dislocations.

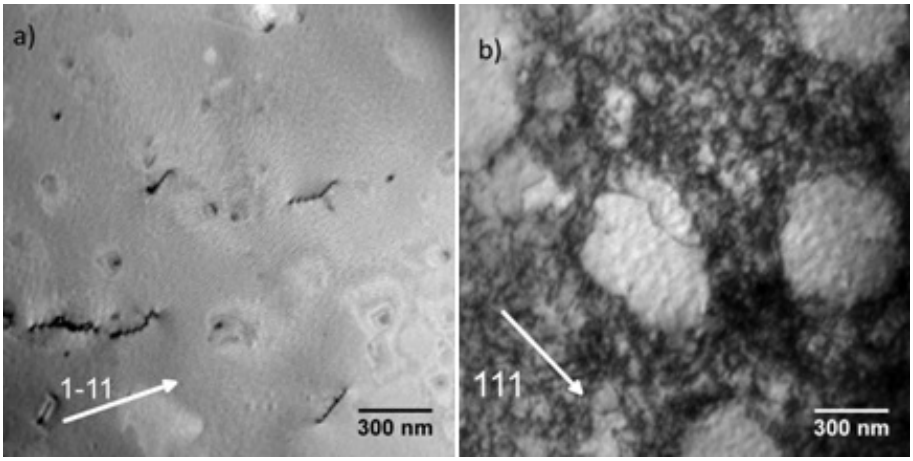

Figure 4.1: *Transmission Electron Microscopy images of a) the annealed and b) the cold-rolled copper pre-shock.*

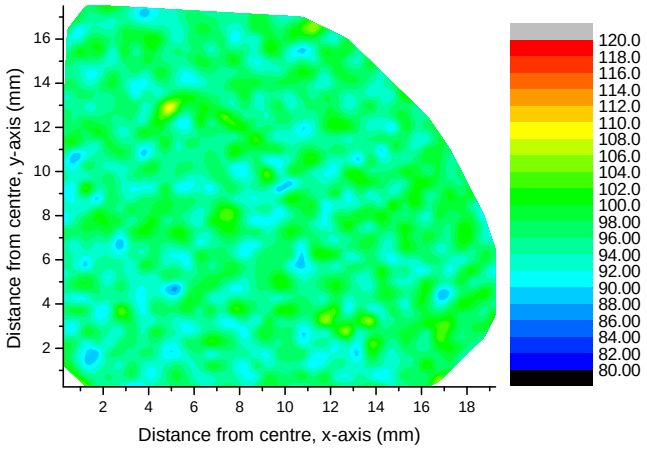

Figure 4.2: *Hardness contour map for the impact face of the cold-rolled copper specimen shock loaded to a peak pressure of 5.96 GPa.*

the hardness in the shock loaded specimens measured is constant across the impact and rear surfaces. A contour map derived from this procedure can be seen in Figure 4.2, which is representative of all of the other hardness maps. The only observable difference between the impact and rear surfaces of the specimens was a change in the average hardness. This was investigated by measuring the change in hardness with increased distance from the impact surface in the shock loaded specimens.

The hardness profiles in Figure 4.3 display two different shapes. In Figure 4.3c there is no correlation between hardness and distance from the impact face of the specimen. Among the remaining specimens the cold-rolled specimens show a largely constant hardness value until around 3 mm from the impact face. Beyond this point there is a linear increase in hardness towards the rear surfaces of the specimens. Before the point where the linear increase in hardness begins, the shocked annealed specimen, seen in Figure 4.3a, shows a linear decrease in hardness with increasing distance from the impact face. The annealed specimen also displays a linear increase in hardness from a point 3 mm from the impact face. The hardness and hardness profiles for all shocked and unshocked copper specimens can be seen relative to each other in Figure 4.4.

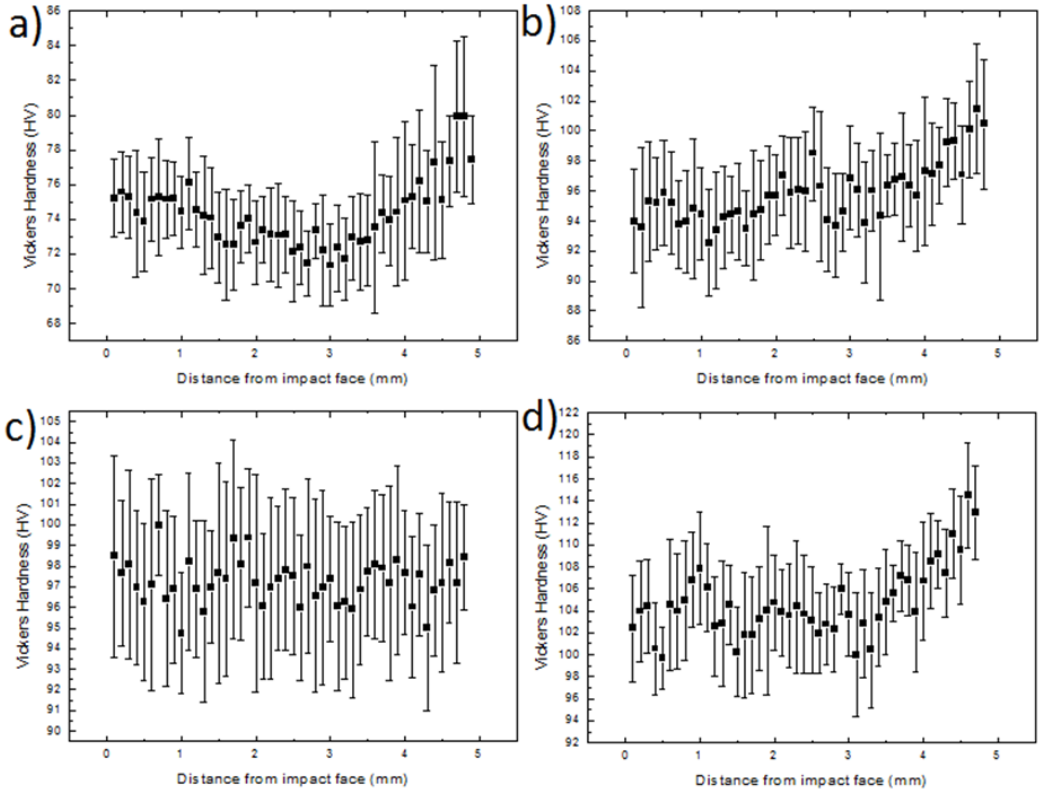

Figure 4.3: *Hardness profiles for: a)Annealed copper shock loaded to 5.08 GPa; b) Cold-rolled copper shock loaded to 5.87 GPa; c) Cold-rolled copper shock loaded to 5.96 GPa and d) Cold-rolled copper shock loaded to 9.60 GPa.*

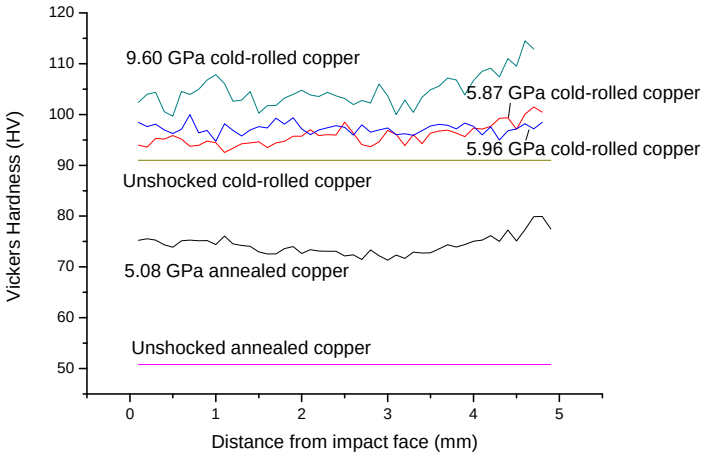

Figure 4.4: *Combined hardness profiles for all shocked and unshocked copper specimens.*

Compression Tests

Cylindrical samples 5 mm long and 5 mm in diameter were sectioned from the copper specimens using electrical discharge machining (EDM). They were compressed at a strain

rate of 1×10^{-3} s^{-1}. The resulting curves were plotted with an offset on the strain axis representing the residual strains (ϵ_r) introduced into the specimens by shock loading, or cold-rolling. The offset due to cold-rolling is described by the equation:

$$\epsilon_r = \frac{2}{\sqrt{3}}\epsilon_x \tag{4.1}$$

where ϵ_x is the strain introduced along the x-axis. In this case, the x-axis is defined as parallel to the loading direction and ϵ_x can be described by the equation:

$$\epsilon_x = ln\frac{w}{w_0} \tag{4.2}$$

where w_0 and w are the thickness of the material bar before and after rolling respectively. The y- and z-axes are perpendicular to the loading direction and the specimens have cylindrical symmetry around the x-axis. The offset due to shock loading is described by the equation:

$$\epsilon_r = \frac{4}{3}ln\frac{V}{V_0} \tag{4.3}$$

where V and V_0 are the initial and final specific volumes ($\frac{1}{\rho}$), within the shock wave, of the specimen respectively. The fraction $\frac{V}{V_0}$ can be obtained from the equations of state defined in Section 2.5.2 and can be calculated using the particle velocity and shock wave velocity in the plate impact experiment. This equation includes loading from both the shock and release waves and assumes that the degree of strain from each is equal and cumulative. Different equations are used to calculate the residual strain in the cold-rolled and shock loaded specimens, as the specimens have been subjected to different loading regimes. During cold-rolling $\epsilon_x \neq \epsilon_y = \epsilon_z \neq 0$, whereas during shock loading $\epsilon_x \neq \epsilon_y = \epsilon_z = 0$.

The stress-strain curve for the unshocked cold-rolled copper, shown in Figure 4.5a, lines up perfectly with the unshocked annealed copper, as would be expected after quasi-static deformation. Post shock, the annealed copper in Figure 4.5b has a yield strength greater than the flow stress of the annealed copper subjected to an equivalent level of strain at a much lower strain rate. The cold-worked copper samples

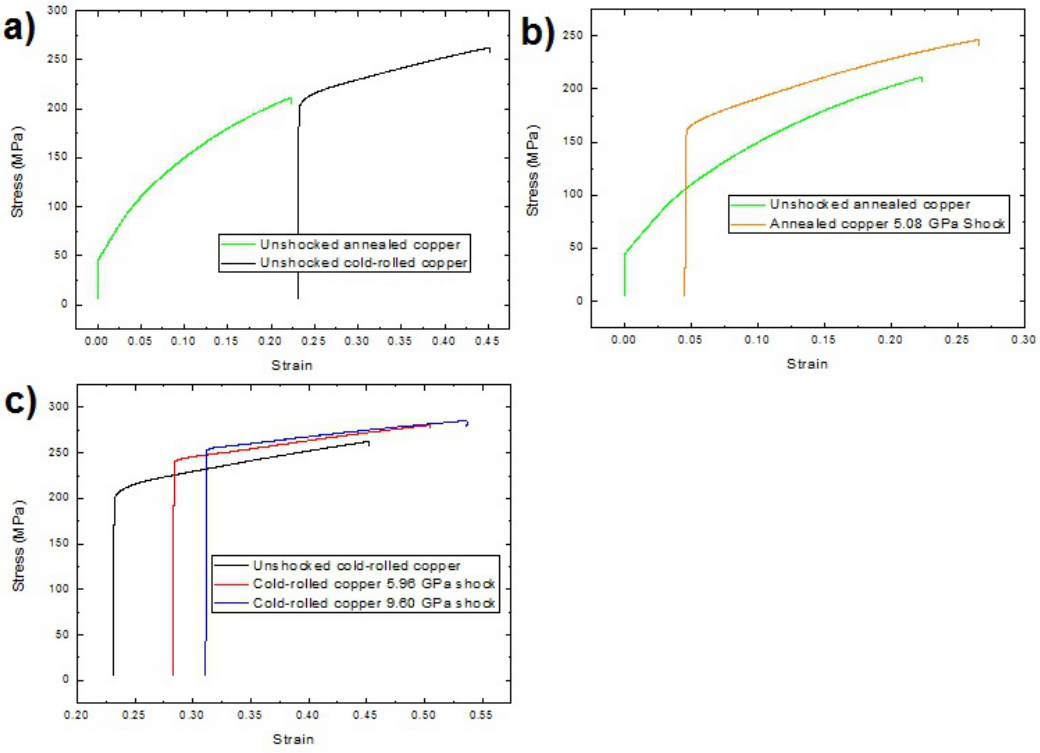

Figure 4.5: *Stress-strain curves of: a) unshocked annealed copper and unshocked cold-worked copper, b) unshocked annealed copper and annealed copper shock loaded to a peak pressure of 5.08 GPa, and c) unshocked cold-worked copper; cold-worked copper shock loaded to a peak pressure of 5.96 GPa and cold-worked copper shock loaded to a peak pressure of 9.60 GPa. The curves were obtained by compression at* 10^{-3} s^{-1}.

in Figure 4.5c show a slight increase in yield strength above the unshocked cold-rolled copper curve, but not to the same extent as shown in Figure 4.5c.

Transmission Electron Microscopy

The TEM bright field images shown in this section are representative of the microstructure of the specimen location they were taken from. Five samples each were taken to confirm the microstructures seen in Figure 4.6 and four samples were taken to confirm the microstructures seen in Figure 4.7.

The post-shock microstructure of the annealed and cold-rolled copper can be seen in Figures 4.6a and 4.6b respectively. These samples were taken from within 0.5 mm of the impact face. The post-shock annealed copper has developed the dislo-

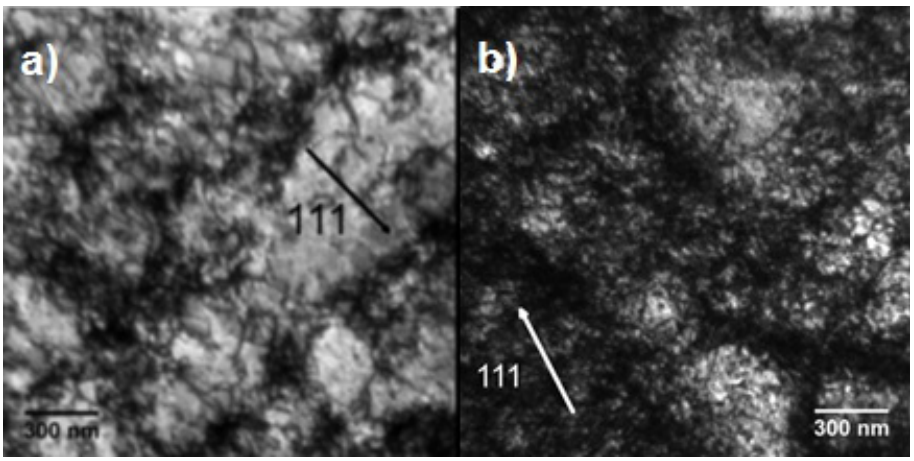

Figure 4.6: *Bright field Transmission Electron Microscopy images of a) annealed copper shock loaded to a peak pressure of 5.08 GPa and b) cold-rolled copper shock loaded to a peak pressure of 5.96 GPa.*

cation cell wall structure that is characteristic of shock loaded copper. The dislocation tangle walls are thinner than those observed in the cold-rolled copper in Figure 4.1b. The dislocation density inside the cells is not zero, but is still substantially lower than in the cell walls. The cold-rolled copper has also developed thinner dislocation cell walls post-shock. The dislocation density within the walls is much higher than that observed in the post-shock annealed specimen and the dislocation density within the cells is higher than in the post-shock annealed specimen's cells.

To investigate the hardness variations reported in Figure 4.3, TEM samples were taken from between 3 and 3.5 mm of the impact surface and within 0.5 mm of the rear surface of the annealed copper specimen shock loaded to a peak shock pressure of 5.08 GPa. The uncertainty in the precise origin of the samples arises from using an EDM to slice the shocked copper specimen. The slices taken from the specimen for electropolishing were 0.5 mm thick and so the thin area imaged could originate from anywhere in that 0.5 mm slice.

The images in Figure 4.7a and 4.7b were taken from between 3 and 3.5 mm of the impact surface and the rear surface of the specimen respectively and show very similar microstructures. They both display the dislocation cell structure seen above, which is characteristic of shock loaded copper. The main difference between the two

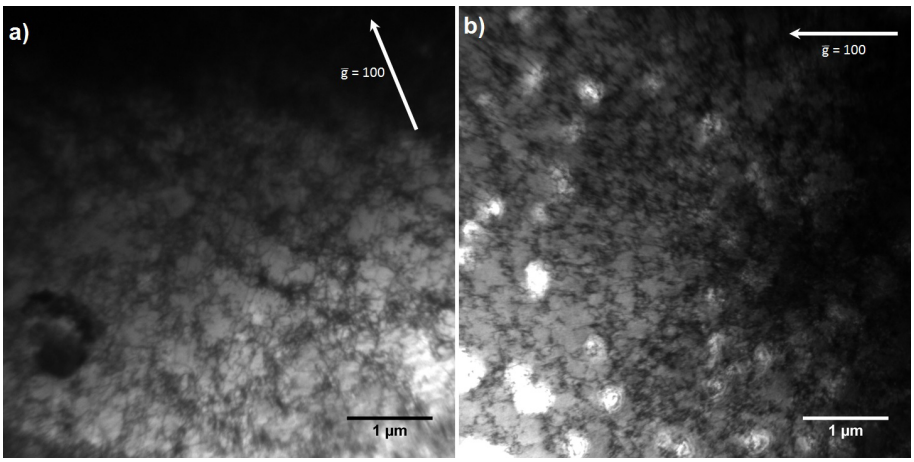

Figure 4.7: *Bright field Transmission Electron Microscopy images of annealed copper shock loaded to a peak pressure of 5.08 GPa. The samples were taken from a) between 3 and 3.5 mm from the impact surface and b) within 0.5 mm of the rear surface of the specimen.*

samples is the size of the dislocation cells that have formed. In the sample from the centre of the specimen, the dislocation cells are larger than those which have formed at the rear of the specimen. The dislocation cells from the centre of the specimen are 667 nm in diameter, while the cells from the rear of the specimen are 400 nm. The cell walls from the rear of the specimen also appear to be less dense in places than those from between 3 and 3.5 mm from the impact surface. This was determined to be linked the the peak pulse duration of the shock wave and will be discussed in greater detail in Section 4.2.

4.1.2 Tantalum

Starting Material

The microstructure of the tantalum before cold-rolling and/or shock loading can be seen in Figure 4.8a. Due to a lack of knowledge of the processes that this material was subjected to prior to purchasing, this material is referred to as "As-Received" tantalum. The microstructure observed in the as-received material consists of long, parallel, tangled dislocation cell walls, with an absence of dislocations in the spaces between. These walls suggest that the material has been subjected to some degree of cold-rolling during its lifetime, but the absence of obvious bend contours, or other strain effects in the TEM micrograph suggests that some degree of annealing has also taken place.

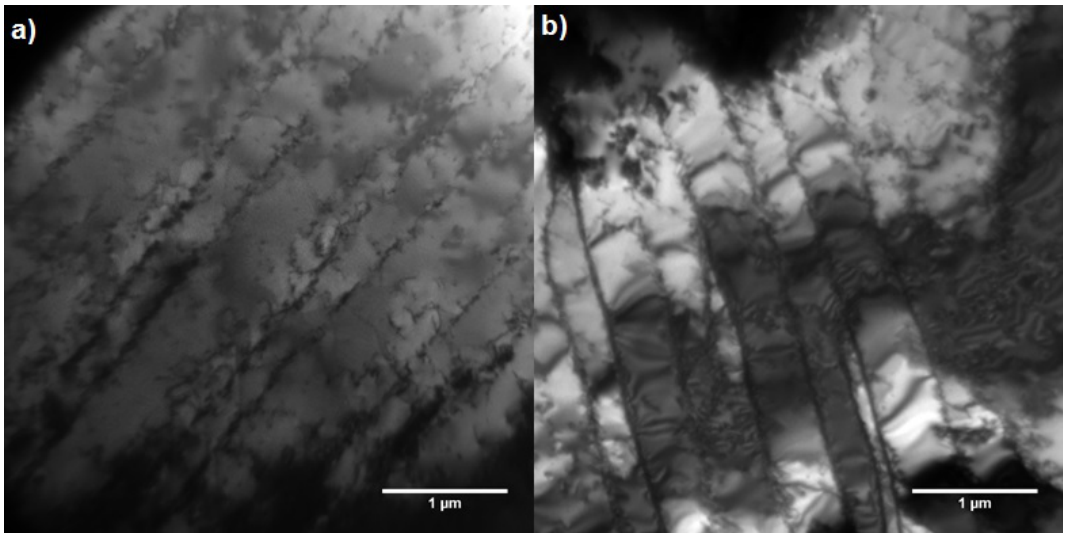

Figure 4.8: *Transmission Electron Microscopy images of a) the as-received and b) the cold-rolled tantalum pre-shock.*

The cold-rolled tantalum specimen observed in Figure 4.8b was subjected to a reduction in thickness by rolling of approximately 50%. The microstructure observed consists of long, straight, parallel sub-grain walls that are very dislocation dense. Bend contours are present throughout the sample, with orientation contrast often differing across the sub-grain boundary. The width of the sub-grains present in the unshocked cold-rolled tantalum are of the same order of magnitude as the distance between dislocation walls in the as-received tantalum, suggesting that the sub-grain walls developed from the dislocation walls. This matches the behaviour expected from 3-stage hardening in tantalum, as described in Section 2.3.2.

Hardness

Hardness values for the unshocked specimens were averaged from 100 individual measurements. Hardness profiles were taken for the shocked specimens, beginning at the impact face at intervals of 0.1 mm with each data point consisting of 10 individual measurements. All measurements were taken using a 0.2 kg load. A summary of the samples tested, with average hardness values, or hardness ranges where appropriate, can be found in Table 4.2.

As-Received\ Cold-Rolled	Peak Shock Pressure (GPa)	Vickers Hardness (HV)	Uncertainty (HV)	χ^2 Value from Hardness Map
As-Received	0	89.5	1.9	1
As-Received	7.20	113.3-129.1	8.5	1
Cold-Rolled	0	135.1	8.9	1
Cold-Rolled	7.20	119.1-136.8	7.4	0

Table 4.2: *Vickers hardness measurements of as-received and cold-worked tantalum, both shocked and unshocked. For specimens where a range is presented, the hardness varied throughout the specimens thickness.*

Cold-rolling the tantalum resulted in a 43% increase in hardness. The post-shock as-received specimen showed a 35% increase in hardness, whereas the post-shock cold-worked samples showed a 5% decrease at the same peak shock pressures.

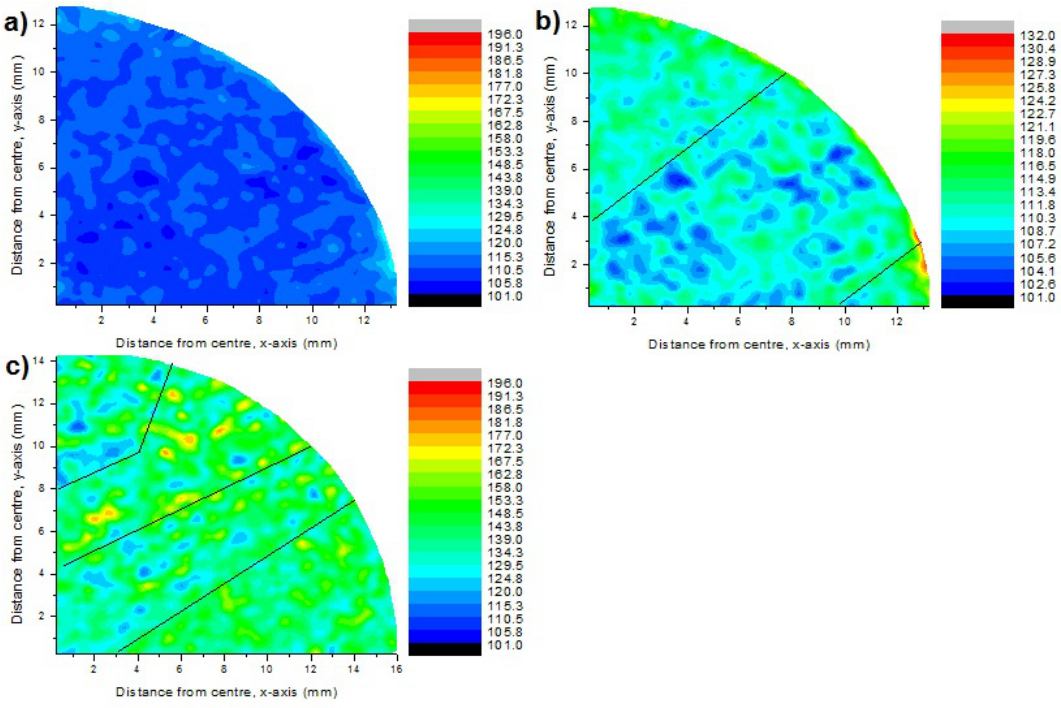

Figure 4.9: *Hardness contour map for the impact face of a) and b) as-received tantalum shock loaded to a peak pressure of 7.20 GPa and c) cold-rolled tantalum shock loaded to a peak pressure of 7.20 GPa. The as-received tantalum hardness contour maps have been presented with: a) the same hardness range as that used for the cold-rolled tantalum hardness map, to facilitate better comparison between the two maps and b) a hardness range between the maximum and minimum hardness values measured in the contour, to better identify variations in the hardness within the contour. Areas of similar hardness variation have been delineated by black lines to aid identification.*

Hardness maps covering a quarter of the impact surface of both the as-received and cold-rolled post-shock tantalum were produced to investigate the possibility of inhomogeneities in the hardness of the specimens. χ^2 tests were carried out on the results from the hardness maps. The hypothesis used in the χ^2 test was based on the assumption that the hardness is constant throughout the measured surface and that this hardness is equal to the average hardness in that surface. The χ^2 value for the as-received tantalum specimen was unity, showing perfect agreement with the expected value. This shows that the hardness of the shock loaded as-received specimen is constant across the impact surface. In contrast, the cold-rolled shock loaded specimen returned a χ^2 value approaching zero showing that significant deviations from the average hardness exist within the cold-rolled specimen. Contour maps derived from this procedure for both the as-received and cold-rolled specimens post-shock can be seen in Figure 4.9. Despite their very different χ^2 results, the two contours actually display somewhat similar features. Both of the specimens have variations in hardness forming loosely defined bands moving from one side of the specimen to the other. The main difference between these two contour maps is the extent of the hardness variation between the bands.

The hardness profiles in Figure 4.10 display two different shapes. In Figure 4.10b there is a linear decrease in hardness with increasing distance from the impact face. In Figure 4.10a there is a linear decrease in hardness with increasing distance from the impact face until around 3 mm from the impact face. Beyond this point there is a linear increase in hardness towards the rear surface of the specimen. The relative hardness

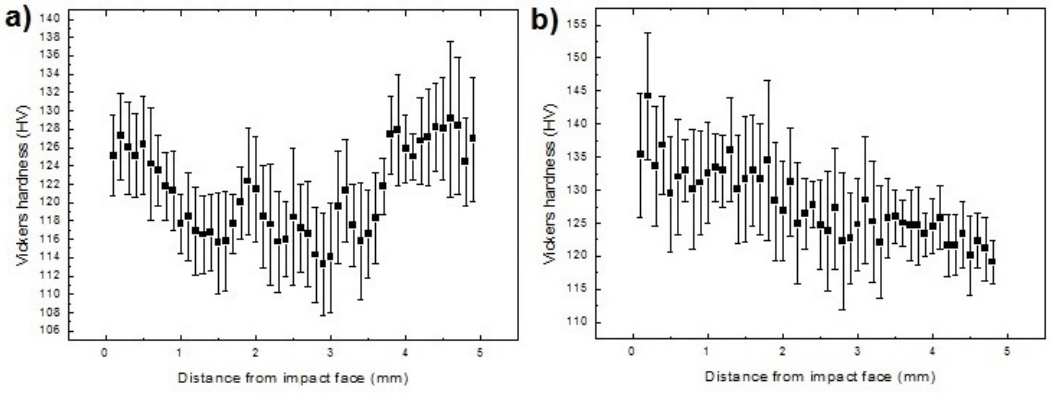

Figure 4.10: *Hardness profiles for: a) As-received tantalum shock loaded to 7.20 GPa and b) Cold-rolled tantalum shock loaded to 7.20 GPa.*

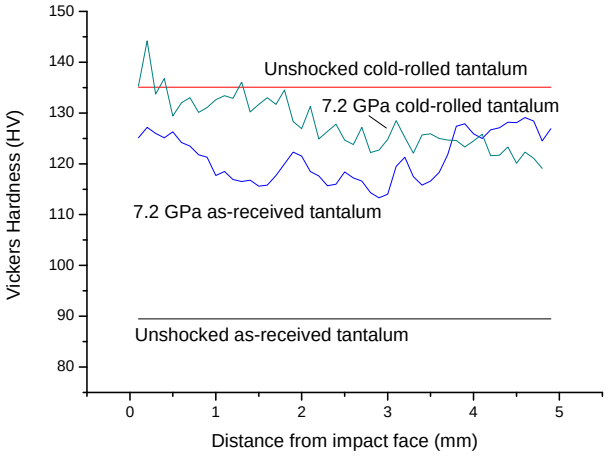

Figure 4.11: *Combined hardness profiles for all shocked and unshocked tantalum specimens.*

and hardness profiles for all shocked and unshocked tantalum specimens can be seen in Figure 4.11.

Compression Tests

Cylindrical samples 5 mm long and 5 mm in diameter were sectioned from the tantalum specimens using electrical discharge machining (EDM). They were compressed at a strain rate of 1×10^{-3} s^{-1}. The resulting curves were plotted with an offset in the same manner as the copper specimens described above.

Due to the large amount of strain applied by cold-rolling to the cold-rolled tantalum material and the relatively small amount of strain applied during compression testing, it is difficult to determine how well the unshocked annealed tantalum stress-strain curve lines up with the unshocked cold-rolled tantalum stress-strain curve. However, they appear to be largely consistent with each other.

In the case of the stress-strain curves for the as-received tantalum before and after shock, shown in Figure 4.12b, shock loading the tantalum has resulted in a yield stress that falls exactly on the stress-strain curve of the unshocked as-received tantalum.

The two curves immediately deviate from each other, with the flow stress for the shock loaded as-received material being higher than the unshocked. In the stress-strain curves for the cold-rolled tantalum, shown in Figure 4.12c, one of the shock loaded cold-rolled curves falls exactly onto the unshocked cold-rolled stress-strain curves, with the other sample falling slightly below the curves, with a reduced yield strength.

Scanning Transmission Electron Microscopy and Transmission Electron Microscopy

Scanning Transmission Electron Microscopy images of FIB samples taken from half-way between the impact surface and the rear surface of the shock loaded as-received and shock loaded cold-rolled tantalum specimens can be seen in Figures 4.13a and 4.13b respectively. These are representative of the microstructure of the tantalum from this location, as confirmed by an additional sample in each case. The post-shock as-received tantalum sample in Figure 4.13a shows almost no trace of the microstructure observed

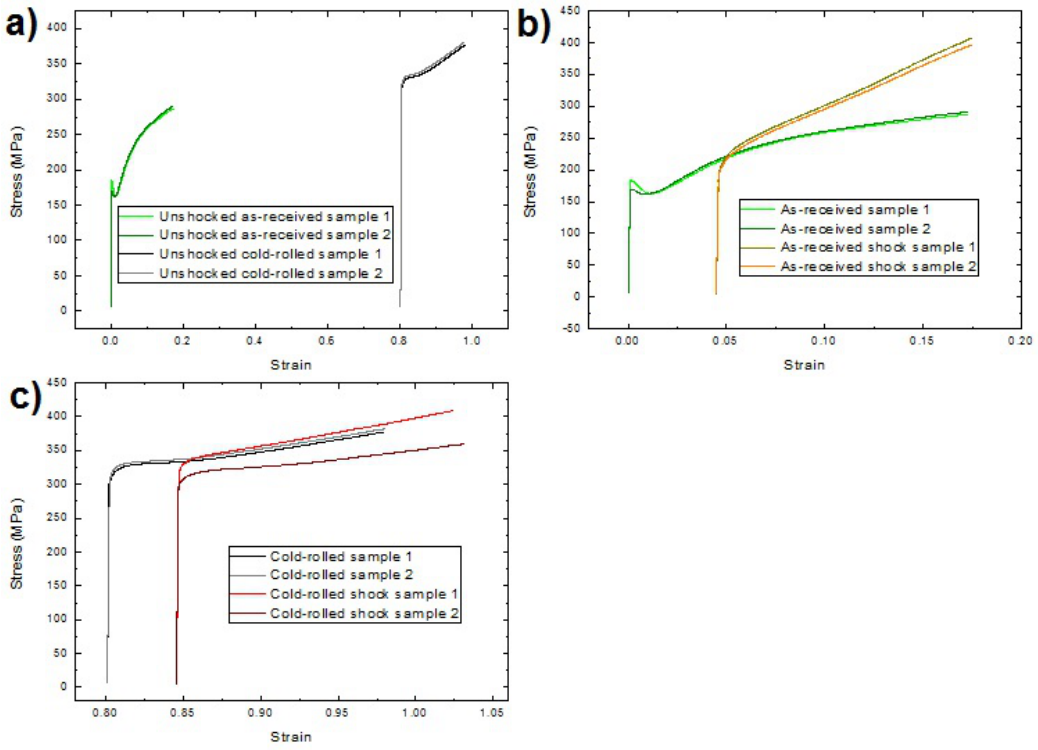

Figure 4.12: *Stress-strain curves of: a) unshocked as-received tantalum and unshocked cold-rolled tantalum, b) unshocked as-received tantalum and as-received tantalum shock loaded to a peak pressure of 7.20 GPa and c) unshocked cold-rolled tantalum and cold-rolled tantalum shock loaded to a peak pressure of 7.20 GPa. The curves were obtained by compression at* 10^{-3} s^{-1}.

in the pre-shock loaded as-received specimen. Some dislocation walls are present, but they do not possess the same dislocation density, or frequency as they did in the pre-shocked specimen. Similarly, the post-shock cold-rolled specimen seen in Figure 4.13b also shows no trace of the clearly defined sub-grain walls present in the pre-shock cold-rolled specimen. Again, some dislocation walls can be observed faintly in the sample, but it completely lacks the dense, parallel sub-grain walls shown in Figure 4.8b.

Due to variations in the hardness of the post-shock as-received tantalum specimen, STEM imaging was also carried out on material taken from the centre of the rear surface of the specimen. Figure 4.14 shows a microstructure that contains the same dense sub-grain walls as the pre-shock cold-rolled tantalum specimen, but without their regular parallel nature. In addition, dislocations appear to have nucleated within the sub-grains.

Back Scattered Electron Microscopy

BSE images were taken from the shocked tantalum specimens to give a wider view of the specimens' microstructure and to confirm whether the dislocation structures observed in

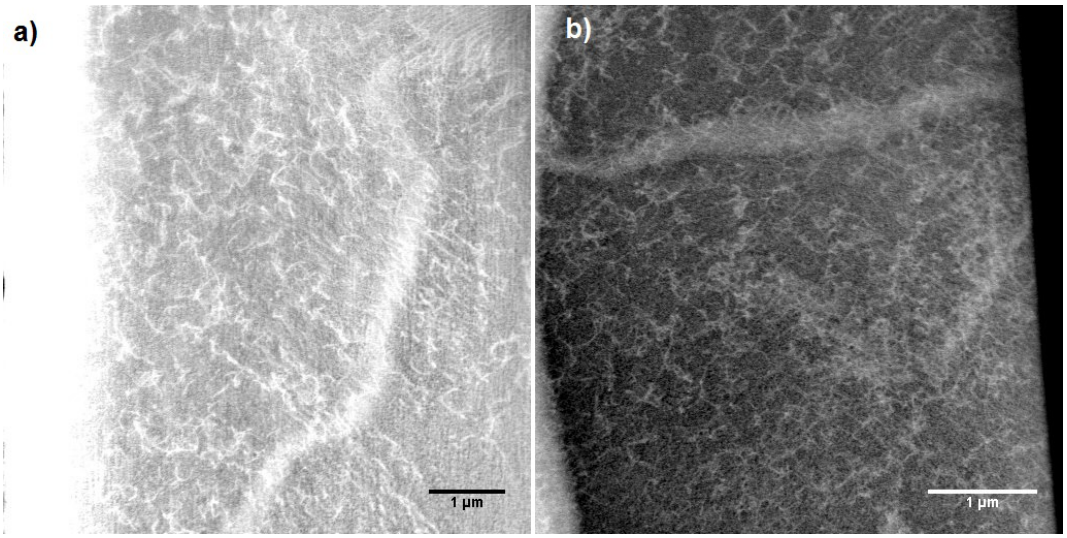

Figure 4.13: *Scanning Transmission Electron Microscopy images of a) as-received tantalum shock loaded to a peak pressure of 7.20 GPa and b) cold-rolled tantalum shock loaded to a peak pressure of 7.20 GPa. Both samples were taken from the centre of the shocked specimens, with the sample normal parallel to the loading direction.*

the FIB STEM samples are representative of the whole specimen. Figure 4.15a and 4.15b show the shock loaded as-received specimen at two different magnifications. Areas of contrast are visible within the grain, suggesting the presence of sub-grain walls. These do not appear to be regular and parallel like the walls observed within the unshocked cold-rolled tantalum and show some agreement with the microstructure shown in Figure 4.14. In contrast, the BSE images of the shock loaded cold-rolled tantalum shown in Figures 4.15c and 4.15d (also at two different magnifications) display the parallel cell walls observed in the unshocked cold-rolled tantalum.

Images were also taken using BSE of the shock loaded cold-rolled tantalum from different locations, to show variation in grain size across the tantalum specimen. These images are shown in Figure 4.16. The BSE images show a variation in grain size from around 60 μm up to 1 mm across the sample. The location of the grain size variations will not directly correlate to the variations detected in the hardness map in Figure 4.9, as the BSE images were taken after the hardness tests had taken place, necessitating a repeat of the grinding and polishing process to ensure good contrast in the BSE image.

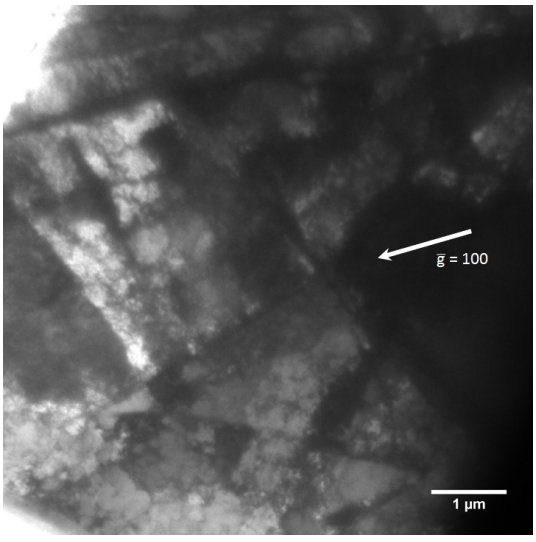

Figure 4.14: *Transmission Electron Microscopy image of as-received tantalum shock loaded to a peak pressure of 7.20 GPa. This sample was taken from the centre of the rear surface of the shocked specimen, with the sample normal parallel to the loading direction.*

Electron Backscattered Diffraction

Under BSE, the shock loaded as-received tantalum showed a large degree of orientation contrast in bands within the grains. This made identifying grain boundaries and determining average grain size, as above, very difficult. As a consequence, EBSD mapping was used to obtain grain size information from across the as-received shock loaded tantalum specimen. These maps are shown in Figure 4.17. The shock loaded as-received tantalum showed a much reduced range of grain sizes than the shock loaded cold-rolled tantalum, varying from 128 μm to 106 μm at different locations within the sample. This falls within the range of grain sizes observed for the shock loaded cold-rolled specimen. This supports the theory that the reason for hardness inhomogeneity being present in the

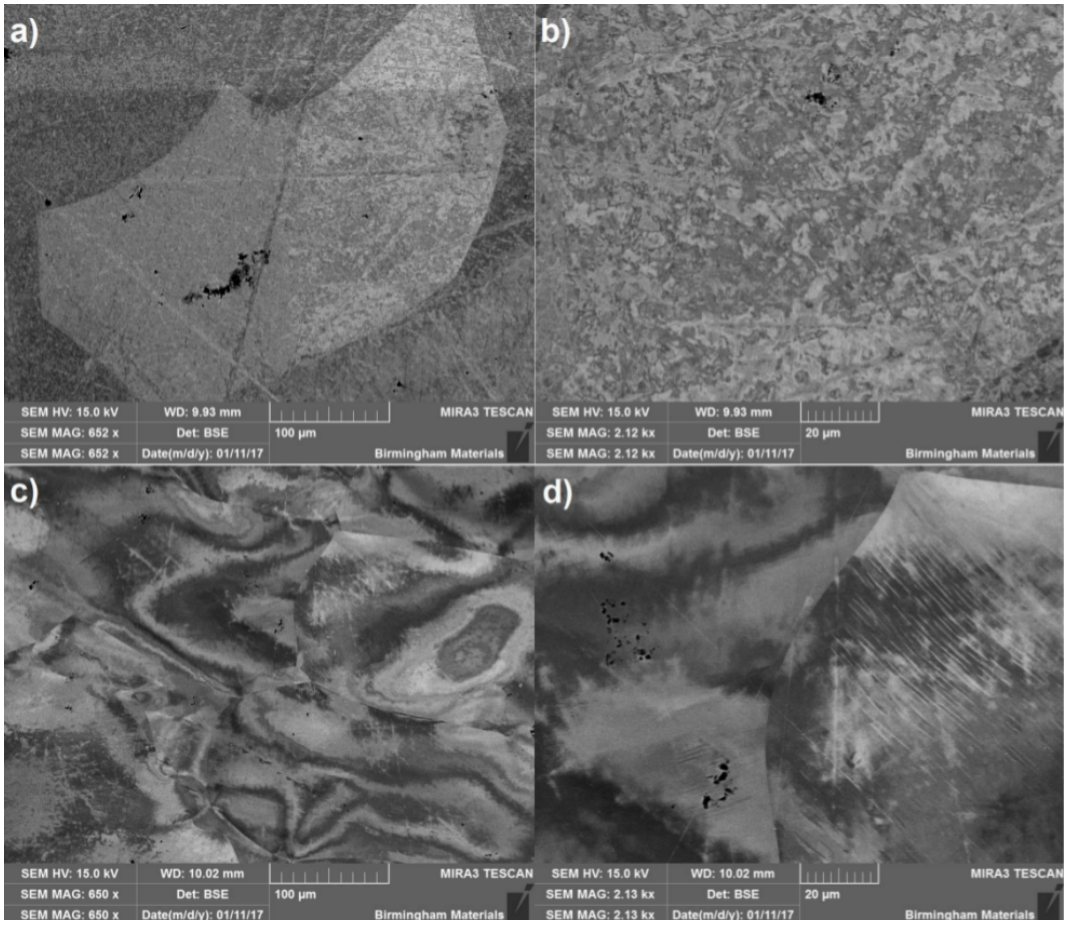

Figure 4.15: *Back Scattered Electron images of a) as-received tantalum shock loaded to a peak pressure of 7.20 GPa at 652 times magnification; b) as-received tantalum shock loaded to a peak pressure of 7.20 GPa at 2120 times magnification; c) cold-rolled tantalum shock loaded to a peak pressure of 7.20 GPa at 650 times magnification and d) cold-rolled tantalum shock loaded to a peak pressure of 7.20 GPa at 2130 times magnification.*

shock loaded cold-rolled tantalum and not the shock loaded as-received tantalum is the variation in the starting grain sizes of the two specimens. The shock loaded cold-rolled specimen appears to have been machined from material with a greater variation in grain size than the shock loaded as-received tantalum.

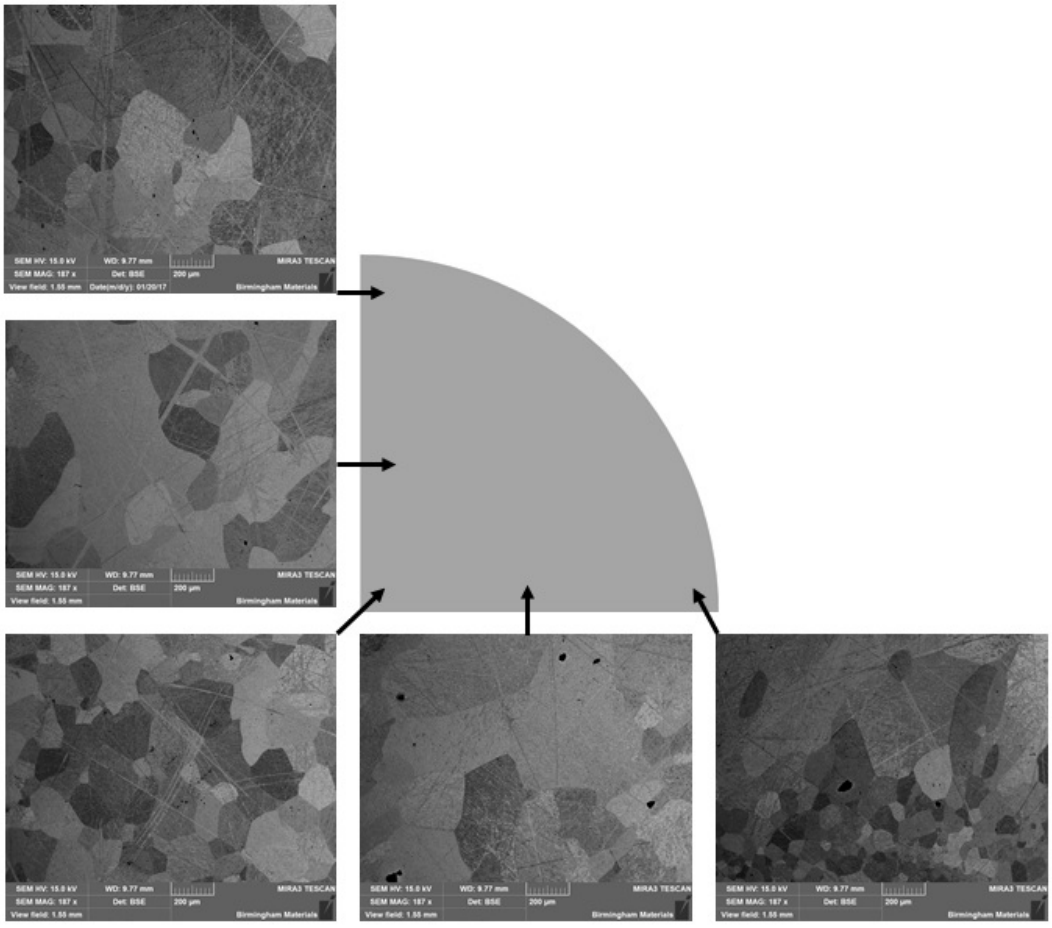

Figure 4.16: *Back Scattered Electron images of cold-rolled tantalum shock loaded to a peak pressure of 7.20 GPa. The images were taken from the impact face of a sample comprising a quarter of the shock loaded specimen.*

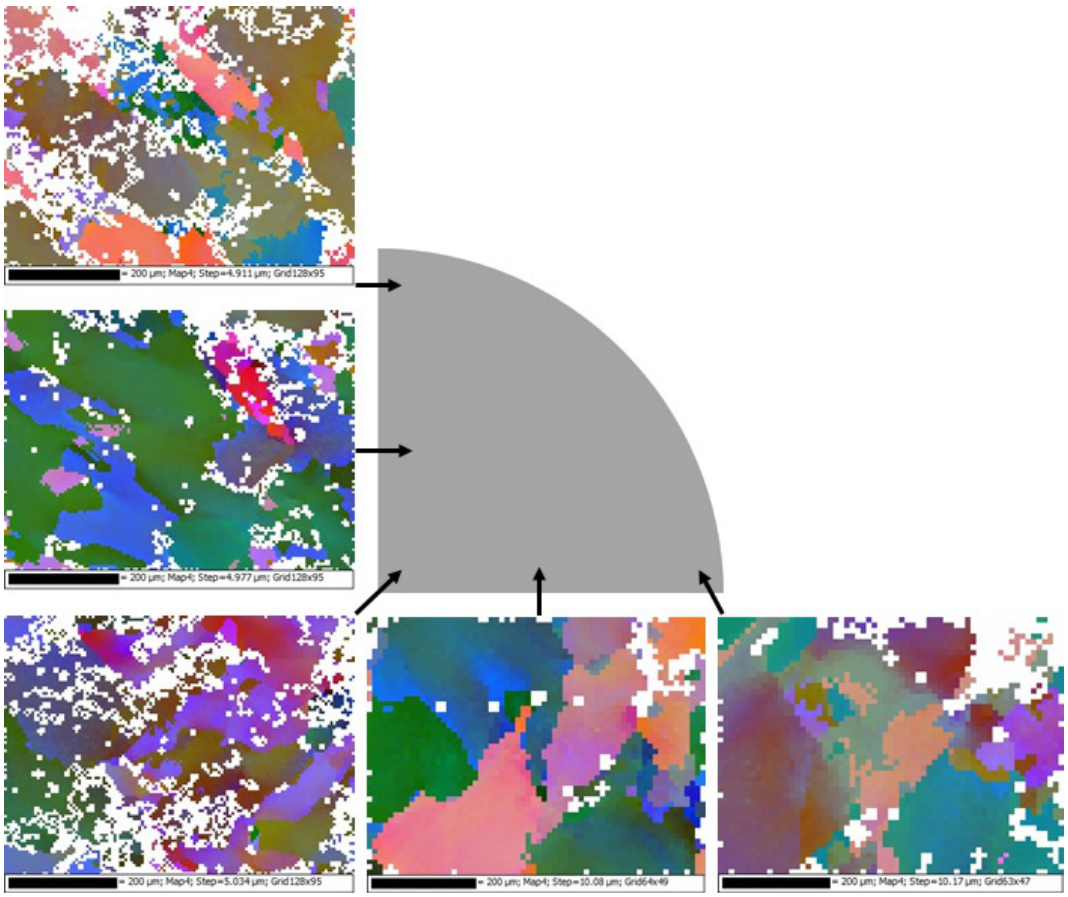

Figure 4.17: *Electron Backscattered Diffraction maps of as-received tantalum shock loaded to a peak pressure of 7.20 GPa. The images were taken from the impact face of a sample comprising a quarter of the shock loaded specimen.*

4.1.3 Results Summary

Copper

Copper starting material sees development of dislocation cells with wide cell walls and dislocation free interiors after cold-rolling to 20%.

The increase in hardness of annealed copper post-shock much higher than cold-rolled copper post-shock. Hardness response is proportionally much greater from the shock loading than from the cold-rolling. Hardness mapping with chi-squared testing showed negligible deviation from the average hardness. Hardness profiles showed a decrease in hardness from the front surface of the shock loaded annealed copper to the spall plane and a constant hardness in the shock loaded cold-rolled copper to the spall plane. For the annealed copper post-shock and the 5.87 and 9.60 GPa shock loaded cold-rolled copper, a linear increase in hardness began at the spall plane and continued to the rear of the specimens. Corrected for residual strain, the stress-strain curves of the annealed copper pre- and post-shock showed the standard path dependent behaviour, where the shock loaded annealed copper sample had a yield strength much higher than the flow stress of the unshocked annealed copper at the same strain. In contrast, the cold-rolled copper curves displayed much reduced sensitivity to loading rate relative to the annealed copper.

Post-shock, the annealed copper produced the standard shocked copper cell structure, with thinner walls than the cold-rolled copper. The shock loaded cold-rolled copper saw a tightening of the dislocation cell walls, as well as an increase in the dislocations present within the dislocation cells themselves. Comparing samples from the shock loaded annealed copper from the rear surface and from just beyond the spall plane. The samples from the rear surface of the specimen displayed smaller dislocation cells with less well defined walls. This was determined to be linked the the peak pulse duration of the shock wave and will be discussed in greater detail in Section 4.2.

Tantalum

Tantalum starting material had a series of parallel dislocation tangle walls, which firmed up into much denser sub-grain walls after cold-rolling to 50%.

The increase in hardness after shock loading of the cold-rolled tantalum was negligible when compared to the increase observed in the shock loaded annealed material. The hardness maps showed a difference in the chi-squared testing between the annealed and cold-rolled shocked material. The annealed shocked material showed a constant hardness throughout and the cold-rolled shocked material showed sizeable variations in the hardness. The contour maps showed definite areas with varying hardness in the cold-rolled shock loaded tantalum. The hardness profiles showed the same kind of decrease in hardness before the spall plane for both specimens. The annealed shock loaded specimen saw the same kind of linear hardness increase as some of the shock loaded copper specimens. Stress-strain curves showed no path dependency in either the as-received, or cold-rolled specimens. A small decrease in yield strength was observed for the shock loaded cold-rolled material.

No dislocation walls were observed in TEM samples taken from near the spall plane of the shock loaded as-received, or cold-rolled tantalum. A sample from the rear surface of the shock loaded as-received specimen showed evidence of the sub-grain walls observed in the starting cold-rolled material. A sample from the rear surface of the shock loaded as-received specimen showed evidence of the sub-grain walls observed in the starting cold-rolled material. BSE images of the shock loaded as-received and cold-rolled tantalum showed that variations in dislocation microstructure occurred across the shocked specimens. Both specimens were found to contain some form of sub-grain wall. The shock loaded as-received tantalum walls were found to be poorly defined and non-parallel. The shock loaded cold-rolled tantalum walls were very well defined and parallel, as observed in the cold-rolled tantalum starting material. BSE imaging was also used to confirm the variations in grain size in the shock loaded cold-rolled tantalum specimen. Grain sizes varied between 60 μm and 1 mm.

4.2 Discussion

4.2.1 Was Specimen Deformation Homogeneous Along the Loading Direction?

Copper

Hardness maps of the impact and rear surfaces of the shock loaded copper specimens were constructed. The main reason for this was to test how successful the lateral momentum trapping apparatus had been at preventing lateral release waves entering the specimen. This method arises from work carried out by Pang *et al.* [43] which discovered that shock loading tantalum without lateral momentum traps and allowing the lateral release wave into the specimen introduced a large amount of additional shear stress into the specimen and allowed the nucleation of twinning at peak pressures far below where it would be expected. The peak shock pressure twinning threshold is around 16 GPa [79], so no deformation twinning was expected in any of the shock loaded copper samples whose greatest peak shock pressure was 9.60 GPa. If lateral release waves had entered the shock loaded copper specimens, then the centre of the specimens would be released by the planar release wave from the rear of the impactor and a band of material around the outside of the specimen would have been released by the lateral release waves. It was assumed that the additional shear stress from the lateral release waves would be sufficient to nucleate twins around the outside band of the shock loaded specimen, which would then present as a harder band of material in the hardness maps. Even in the absence of twinning, a band of differing hardness would have likely presented itself regardless, due to the additional shear stress. The lack of this hardness band, combined with the absence of any deformation twins in the shocked specimens confirmed that no lateral release waves had entered the shock loaded specimens.

Tantalum

Similarly to the copper, hardness maps of the shock loaded tantalum specimens were constructed to investigate the efficacy of the lateral momentum traps. As with the copper specimens, the tantalum specimens showed no evidence of the deviant hardness

band expected in the case of the failure of the lateral momentum traps. However, there were additional features present in the shock loaded tantalum specimens that were not present in the copper specimens. Wide bands of differing hardness can be seen in the hardness maps from both the as-received and cold-rolled tantalum post-shock. It is known that during certain grain refinement processes tantalum can develop a bimodal grain structure [80]. This was confirmed using BSE imaging for the shock loaded cold-rolled tantalum, as shown in Figure 4.16. Bands of tantalum containing larger grains are softer than the areas containing smaller grains. Previous work investigating the effect of grain size on the response of materials to shock loading has found that grain size preferentially favours the creation of twins [81], which are not normally present at these peak shock pressures and are not observed in these specimens. Therefore, in the absence of any other method for inducing hardness variation in the specimens, these hardness variations are more likely to be the result of pre-shock processing in the tantalum. The difference between the harder and softer bands is much more pronounced in the post-shock cold-rolled tantalum. It is logical to assume that either the cold-rolling process has exacerbated the bimodal structure, resulting in a larger difference in grain size between the hard and soft bands, or that the change in microstructure induced by the cold-rolling that increases the hardness of the material has a greater impact on one of the types of band over the other. This variation in hardness is also likely responsible for the decreased hardness observed in the hardness profile for the shock loaded cold-rolled specimen discussed above. The profile was taken from the centre of the specimen, where some of the softest material can be found in the hardness map of the impact face.

4.2.2 How Was the Material Response to Shock Loading Affected by Cold-Rolling?

Copper

It is well known that copper responds to shock loading to a specific strain with an increased yield strength and better developed dislocation cell microstructure relative to quasi-static loading to the same specific strain, as discussed previously in Section 2.6.1. A material exhibiting different behaviour under different loading rates is sometimes referred to as being path dependent. This can be seen reflected in the hardness, stress-

strain curves and microscopy obtained from the shock loaded annealed copper presented in Section 4.1. The residual strain applied to the annealed copper can be calculated from the shock equations of state discussed in Section 2.5.2 and the impact velocity that the specimen is subjected to. This gives a residual strain of 4.5% for the annealed copper post-shock. That 4.5% strain resulted in an increase in hardness in the annealed specimen of 49%. Quasi-static loading up to 27%, as experienced by the cold-rolled copper, resulted in an increase in hardness of 79%. This increase in hardness is 1.6 times that produced by shock loading after 6 times the applied strain, showing a much greater increase in hardness at high loading rates than at quasi-static rates. This can also be seen reflected in the stress-strain curves shown in Figure 4.5. The shock loaded annealed copper shows a yield stress of 163 MPa. Taking the annealed copper to the same level of strain (4.5%), the flow stress measured is only 111 MPa, a much lower value. Finally, the well developed dislocation cell structure observed in the annealed copper specimen post-shock displays a far higher dislocation density and much thicker cell walls than would be expected in a copper specimen that had experienced the same 4.5% strain at a quasi-static rate. For reference, see Figure 4.18 copied from Hoffmann *et al.* [12].

In contrast, the cold-rolled shock loaded copper had a residual strain from shock

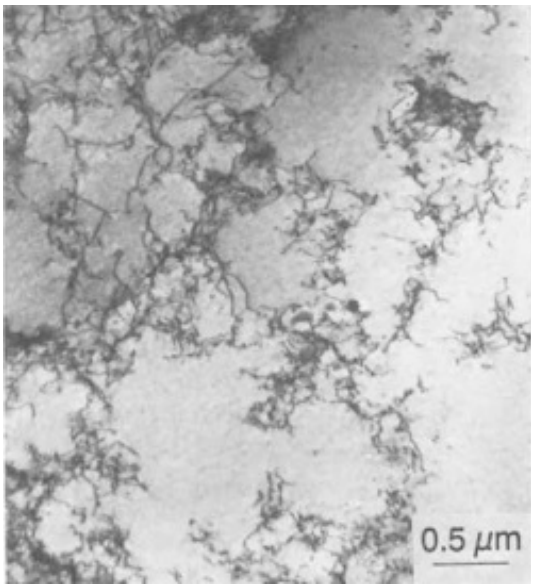

Figure 4.18: *TEM micrograph of copper subjected to 5% strain via tensile test [12].*

of 5.2% and saw an increase in hardness post-shock of 7%. This equates to an increase in hardness 0.14 times that of the initial cold-rolling from 0.17 times the applied strain, which is much closer to a ratio of 1:1, showing behaviour that is more path independent than the annealed copper. Similarly, increasing the peak shock pressure to introduce a strain of 8.0% saw a total increase in hardness of 17%, which is an increase in hardness of 0.35 times the initial cold-rolling from 0.27 times the applied strain. Which is again closer to parity than the shock loaded annealed copper. When offset to account for the residual strain in the specimens, the stress-strain curves for the pre-shock cold-rolled copper and the cold-rolled copper shock loaded to two different peak shock pressures show a much smaller increase in yield strength about the unshocked cold-rolled copper stress-strain curve. This indicates that pre-straining the material prior to shock loading decreases its sensitivity to high strain rate loading.

To investigate the reasons for this, it becomes necessary to revisit the explanation behind the large increase in yield strength and hardness experienced by the shock loaded annealed copper. As discussed in Section 2.6.1, the speed of the shock wave means that it is difficult to accommodate the applied strain by movement of dislocations, and the high strain rate also suppresses dynamic recovery in the specimen, preventing the loss of dislocations formed in the shock wave. The large number of dislocations formed reduces the mean free path between dislocation interaction in the material, leading to an increase in dislocation tangling. This has the effect of producing a well defined dislocation cell structure at a much lower level of applied strain than would be expected under quasi-static loading. In the most basic terms, the relatively large increase in yield strength and hardness is the result of a shift from a clean, annealed copper microstructure with very few dislocations to a well developed dislocation cell microstructure. Such a change is impossible for the cold-rolled copper, as the starting points are so radically different. Instead of the huge shift from no cell structure to well defined cell structure, there is a refining of and addition to the existing cell structure. The dislocations already present within the cell walls and cell interior migrate to form thinner, denser walls and additional dislocations formed in the shock wave also begin migrating to the cell walls. This is shown in Figure 4.6. No huge microstructural change is possible in the same way it is in the annealed copper and so additional strain introduced into the system by shock loading is very similar to the strain introduced by quasi-static loading. Another point

worth considering is that one of the factors contributing to the increased dislocation generation in the shock loaded annealed copper is potentially either no longer valid, or much mitigated. In shock loaded cold-rolled material the issue of dislocation motion being unable to keep up with the shock front is not as big of an impediment to strain being accommodated by moving dislocations. Pre-existing dislocations are present in large numbers throughout the specimen and can act to accommodate the strain applied by the shock wave, reducing the need for dislocation nucleation. However, the existence of yield points above the unshocked cold-rolled copper stress-strain curves (even if the distance is much lower than in the annealed copper case) demonstrates that a degree of strain rate sensitivity is still present in the material. This can be explained by the existence of dislocation free space within the dislocation cell structure in the cold-rolled copper. In this space dislocations can form during shock in the same way they would in annealed copper, introducing larger numbers of new dislocations than would be expected during quasi-static loading.

Another effect of cold-rolling prior to shock loading can be seen in the hardness profiles of the shock loaded copper specimens. There are also additional complications that appear in the profiles past a point 3 mm from the impact surface of the specimens which will be discussed in greater detail in Section 4.2.1. From the impact surface to 3 mm from the impact surface, the hardness profile of the annealed copper shock loaded to a peak pressure of 5.08 GPa sees a linear decrease in hardness with increasing distance from the impact surface. In contrast, the hardness profiles for the shock loaded cold-rolled copper specimens do not display the same decrease in hardness.

The decrease in hardness with increasing distance from the impact surface has been observed by Hsu *et al.* [82] and Meyers *et al.* [83] in nickel, which behaves almost identically to copper under shock loading. They found that the decrease in hardness with increased distance from the impact plane was caused by the attenuation of the shock wave within the specimen. A model was proposed to explain the magnitude of the attenuation, using point and line defect generation in the specimen and the rise in temperature experienced due to the motion of dislocations. This was found to be in agreement with the experimental results and is likely the cause of the linear decrease in

hardness in the shock loaded annealed copper specimen.

However, Hsu *et al.* [82] and Meyers *et al.* [83] also investigated the effect of pre-shock loading on the hardness profile and found that the pre-existing dislocation structure had no impact on the attenuation of the hardness with distance from the impact surface until a certain distance was reached. This distance seemed to coincide with the point at which the decreasing hardness in the shock loaded specimen reached the original hardness of the pre-shocked specimen, at which point the hardness became constant.

The reason for the disparity between the results included in this current report and previous work is unclear. Potentially, the scatter in the individual hardness values in the profiles, or the relatively shorter distances under consideration are obscuring a downward gradient, but this is unlikely given the clarity of the gradient in the shock loaded annealed specimen. The lack of an inverse relationship between hardness and distance from impact surface in the shock loaded cold-rolled copper suggests a lower amount of dislocation nucleation and motion occurs in the cold-rolled copper specimens during shock loading. This results in a decrease in the shock wave attenuation rate.

Tantalum

It is well known that tantalum responds to shock loading in a path dependent manner, in contrast to copper, as discussed in Section 2.6.2. This contrast between the strain rate sensitivity of copper and the strain rate insensitivity of tantalum has been previously explained as resulting from the difference in the Peierls stress in the two materials [42]. Due to the higher Peierls stress in tantalum, dislocation nucleation is restricted, limiting the amount of strain that can be accommodated by new dislocation nucleation and increasing the proportion of the applied strain that is accommodated by the movement of dislocations. Due to the non-planar nature of the screw dislocation cores in tantalum, their motion is heavily restricted. The Peierls stress experienced by the screw dislocations is an order of magnitude higher than experienced by the edge dislocations, which have a planar core [84]. This results in the free motion of the edge components

of dislocations, leaving behind the mostly stationary long, straight screw dislocations that are characteristic of deformed tantalum. This generation of a few long straight screw dislocations, rather than a large amount of free moving dislocations precludes the early formation of dislocation cells and higher than expected yield strength observed in copper. This does not mean that dislocation nucleation is forbidden during the shock loading of tantalum. It is clear from previous work in the field and the results presented in Section 4.1.2 that dislocation nucleation does occur, but the higher Peierls stress limits the extent to which this can occur and makes the kind of path dependent behaviour seen in materials like copper and nickel impossible.

This is most apparent when comparing the stress-strain curves of the as-received tantalum pre-shock and post-shock, shown in Figure 4.12. Whereas the yield strength of shock loaded copper is a lot higher than the flow stress of the pre-shock material at equivalent strains, the post-shock as-received tantalum yield stress is identical, to the equivalent flow stress in the pre-shock material. This trend continues when comparing the cold-rolled tantalum pre-shock and post-shock. The stress-strain curves show no difference between the material response to quasi-static and shock loading. For one of the samples there is a slight decrease in yield strength when compared to the flow stress of the unshocked material at an equivalent strain. Tantalum yield points sitting above and below the stress-strain curve of the unshocked material have been seen before by Gray [42] and are likely linked to the tendency of tantalum to form a bimodal grain structure after treatment [80]. If the compression samples were taken from areas of the specimen with larger grain sizes, this would influence the strain behaviour of the sample. However, this variance is largely negligible and comments related to the overall shape of the stress-strain curve are still valid.

The most obvious difference between the stress-strain curves of the as-received tantalum and the cold-rolled and shock loaded tantalum specimens is the absence of an upper and lower yield strength in the cold-rolled and shock loaded specimen curves. The existence of upper and lower yield points in a material usually arises from pre-existing dislocations being pinned by interstitials in the material. A critical amount of stress much be applied to the material in order for these dislocations to overcome this pinning

force. Work by Millett *et al.* [85] investigating the effect of cold-rolling on the shock profile of tantalum suggested that cold-rolling the tantalum prior to shock loading could act to disengage the pre-existing dislocations from the pinning interstitials and generate a larger number of mobile dislocations in the specimen. The absence of the upper and lower yield points in the stress-strain curve for cold-rolled tantalum would seem to support this conclusion. Moreover, the absence of the upper and lower yield points from the shock loaded as-received tantalum specimens suggests that the shock loading process performs much the same function, liberating pre-existing pinned dislocations from their pinning interstitials.

Another difference between the copper specimens and the tantalum specimens is the response of the hardness profiles to shock loading. Again the hardness profile behaviour at a distance greater than 3 mm from the impact surface will be discussed in greater detail in Section 4.2.3. Where the shock loaded copper specimens all showed an increase in hardness after shock loading, only the as-received tantalum increased in hardness relative to its unshocked material. Again, this may be related to the unfortunate tendency for tantalum to form a bimodal grain structure and as such the apparent decrease in hardness cannot be taken as significant. This is emphasized by the fact that, in the hardness maps taken from the impact face of the shock loaded cold-rolled tantalum, some of the areas measured showed a hardness as high as 195 HV, far in excess of the unshocked cold-rolled tantalum starting hardness.

The shock loaded as-received tantalum displays the same decrease in hardness from the impact surface of the specimen as observed in the front 3 mm of the shock loaded annealed copper. Tantalum has also been shown to experience shock wave attenuation, which occurs as a linear progression with distance from the impact surface [86], so this behaviour is consistent with the literature and emerges from the same underlying factors discussed above for copper.

The microstructure of the shock loaded cold-rolled tantalum seen in Figure 4.13b is very similar to the shock loaded as-received tantalum microstructure in Figure 4.13a. This is particularly surprising as the starting microstructure for the cold-rolled tantalum

observed in Figure 4.8b was very different from the starting structure of the as-received tantalum and indeed the structures in Figure 4.13. The structure evolution observed in the post-shock as-received tantalum is not surprising. A series of straight dislocations beginning to tangle, with some evidence of pre-existing dislocation walls is the kind of structure that would be expected after a small amount of strain is introduced into the starting as-received material. The fact that the shock loaded cold-rolled specimen shows no evidence of the sub-grain walls present in the starting material either indicates that the shock loading has completely removed the sub-grain structure from the specimen (which is highly unlikely), or that the microstructure observed at many locations in the cold-rolled specimen is not present throughout the entirety of the specimen. This goes some way towards explaining the large variations in hardness observed in the lateral hardness maps. The bands of increased hardness highlighted in Figure 4.9c likely represent the presence of areas of particularly well developed sub-grains and the areas of lowest hardness will likely have a microstructure more closely resembling the unshocked as-received material, with the majority of the hardness range displaying the microstructure seen in Figure 4.8. This is supported by the BSE images shown in Figure 4.15, which show a small degree of sub-grain development in the shock loaded as-received tantalum specimen and well developed sub-grain walls in the shock loaded cold-rolled specimen. The STEM images shown in Figure 4.13 show that neither of these microstructures are present everywhere in the material, but they are common enough to be found with little effort.

4.2.3 How Effective Were the Spall Plates?

Hardness profiles were generated for all shock loaded specimens in order to confirm that the specimens had been subjected to the same degree of loading along the total thickness of the specimen. For the copper specimen shock loaded to 5.96 GPa and the cold-rolled tantalum post-shock, this was shown to be the case, as the hardness measured remained constant throughout the specimen's thickness. In contrast, the profiles of the copper specimens shock loaded to peak pressures of 5.08 GPa, 5.87 GPa and 9.60 GPa, and the as-received tantalum post-shock showed a marked linear increase in hardness, beginning at 3 mm from the impact surface and continuing to the rear surface

of the specimen. The only known differences between the specimens that displayed this hardness increase and the specimen that did not was the momentum trapping apparatus used. The specimens with the constant hardness made use of the thin (in the case of the copper specimen shock loaded to a peak pressure of 5.08 GPa) and thick spall plate apparatus (in the case of the cold-rolled tantalum shock), whereas the specimens that displayed the hardness increase made use of the thick spall plate apparatus (in the case of the specimen shock loaded to a peak pressure of 5.96 GPa) and the cup apparatus (in the case of the specimens shock loaded to a peak pressure of 5.87 GPa and 9.60 GPa). Descriptions of the different momentum trapping apparatus used can be found in Section 3.1.1.

Due to the possible link between the spall plate apparatus and the change in hardness profile, wave diagrams were generated for the shock loading of the specimens with spall plates present and no spall plate present in the experimental setup. These can be seen in Figure 4.19. The shock wave properties used to generate the wave diagram were for the specimen shock loaded to a peak pressure of 5.87 GPa, but the expected wave behaviour will apply to all of the specimens. In the case of the wave diagram for the successful spall plate apparatus in Figure 4.19a, a planar shock wave is generated at the impact face, which then travels into both the impactor and the specimen at a speed of 4144 ms^{-1}. When the shock wave reaches the rear of the specimen, the spall plates prevent a release wave being generated. When the shock wave reaches the rear of the impactor, a planar release wave is generated, which moves back through the impactor and through the total thickness of the specimen, bringing it back down to ambient pressure. The release wave travels at a speed of 4414 ms^{-1}, which is higher than the shock wave speed, as the sound speed in the compressed material is higher owing to the increased density. Due to this difference in wave speeds, the release wave will slowly draw closer to the shock wave, reducing the total loading time through the thickness of the specimen, though not to a large extent.

When no successful spall apparatus is present, as shown in Figure 4.19b, the shock waves travel into the specimen and the impactor as in the previous case. However, without the spall plates, release waves are generated at the rear surfaces of both

the specimen and the impactor. The two release waves will interact at the spall plane, applying tension to the material in the plane. Further waves will then be generated by this area of tension, but the magnitudes of these are such that they can be safely ignored. In Figure 4.19 the spall plane is present at 2.9 mm from the impact surface. As in Figure 4.19a, the total loading time will see a slight linear decrease between the impact surface and the spall plane due to the increased speed of the release wave. However, in this case, the rear of the specimen will be released by the release wave originating from the rear surface of the specimen. From Figure 4.19 it can be seen that this results in a very different pattern in the total loading time. This will begin to decrease linearly from

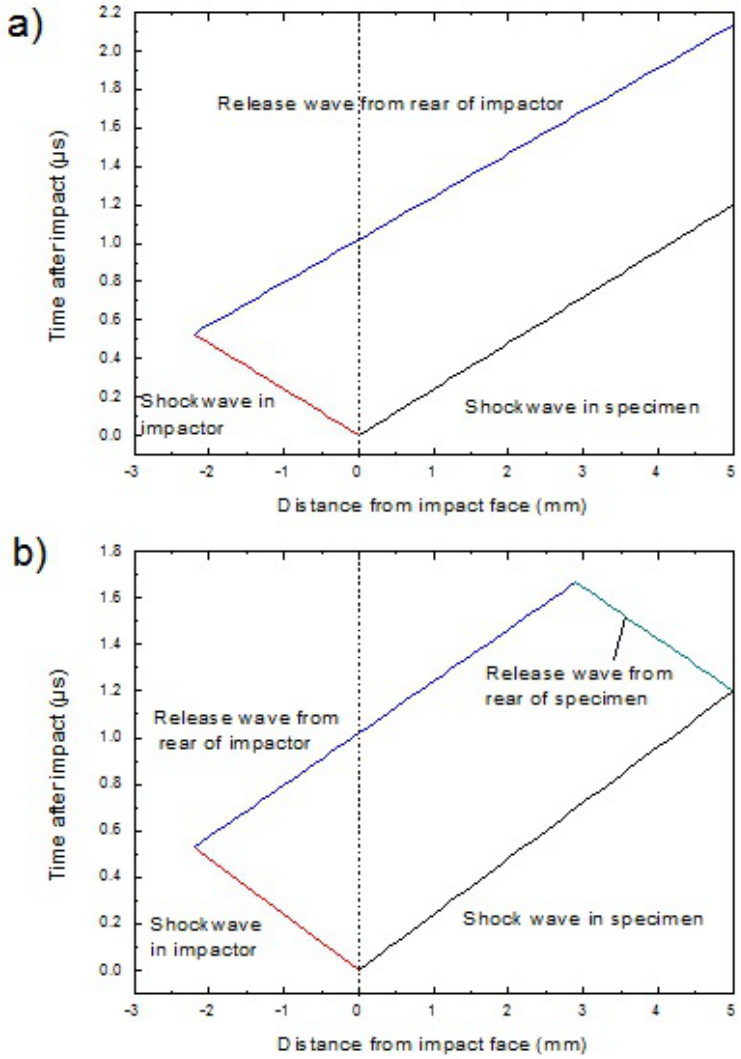

Figure 4.19: *Wave diagram of the shock loaded specimens a) including a spall plate and b) not including a spall plate.*

the spall plane towards the rear surface of the specimen, where it will be effectively zero, with the release wave bringing the material back to ambient pressure almost as soon as compression has occurred.

Copper

The loading time of the shock loaded copper specimens calculated from wave diagrams similar to Figure 4.19 can be seen in Figure 4.20. From this graph it can be seen that the location of the spall plane, where the loading time begins to linearly decrease from 1 μs to zero, coincides with the point on the hardness profiles where the Vickers hardness begins to linearly increase. This confirms that the linear increase in hardness observed is linked to a failure of the spall plates. Sencer *et al.* [87] investigating the effect of a shorter duration "Taylor wave-like" triangular pulse on copper found that the decreased loading duration resulted in an increase in the yield strength of the material. Work by Moin and Murr [88] on nickel found that, for loading durations $\leq$1 μs and peak pressures $\leq$6.6 GPa, an increase in the loading duration resulted in an increase in the size of the dislocation cells, with better defined walls. This is mirrored by the TEM images in Figure 4.7, comparing the microstructure of annealed copper shock loaded to 5.08 GPa from between 3 and 3.5 mm from the impact surface and from the rear surface of the

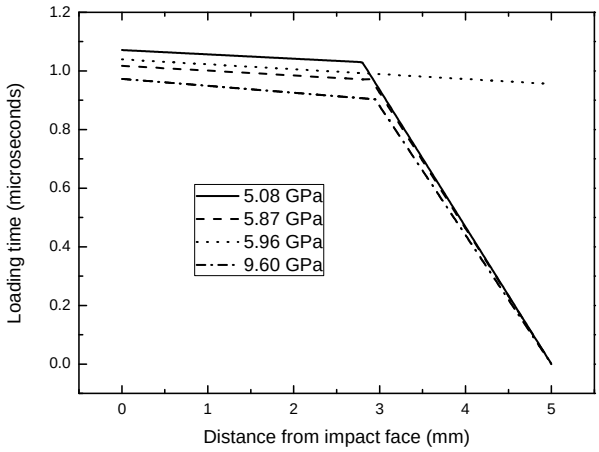

Figure 4.20: *Variation in the peak loading time of the shock loaded copper specimens with increased distance from the impact surface.*

specimen.

A decrease in dislocation cell size is also accompanied by an increase in the dislocation density [87]. The decrease in the loading duration also provides less time for dislocations formed in the shock wave to migrate to the cell walls and for recovery to occur within the material. This is supported by the TEM images in Figure 4.7, which show a less relaxed microstructure in the low loading time material than in the higher loading time material. This combination of lower cell size, increasing dislocation density and less relaxed microstructure for the lower loading rate combine to produce the inverse linear dependence between loading time and resulting material hardness observed in the shock loaded copper specimen hardness profiles.

The existence of this inverse linear dependence in even the shock loaded cold-rolled copper specimens and the shock loaded tantalum specimens shows that this effect occurs regardless of the strain rate sensitivity of the material and is purely linked to the loading duration and the peak shock pressure. In the case of the cold-rolled copper shock loaded to 5.87 GPa and 9.60 GPa, the peak shock pressure is increased by 1.63 times and the gradient of the inverse linear dependence between the pulse duration and the hardness increases by 1.73 times. Comparing shock loaded annealed copper to the cold-rolled copper shock loaded to 9.60 GPa produces a very similar result. This shows that the peak shock pressure applied has a direct impact on the sensitivity of copper (regardless of the pre-shock condition of the material) to loading duration.

This is likely linked to the reduction in dislocation cell diameter produced by an increase in the peak shock pressure. The even smaller cells will be accompanied by a greater dislocation density and will evidence a greater hardness increase at the rear of the specimen. The greater drop in hardness with increasing loading time may be the result of dislocations generated at the centre of the dislocation cells requiring less time to migrate to the cell walls, meaning that a much greater proportion of the loading cycle can be spent settling into a more relaxed microstructure than at lower peak shock pressures.

Tantalum

As mentioned in the previous section, loading duration sensitivity is independent of any kind of strain rate sensitivity. This applies to the two different origins of strain rate insensitivity: the inability of the cold-rolled copper to produce a well defined dislocation cell structure at relatively low applied strains in the way that shock loaded annealed copper does, and the high Peierls stress limiting of dislocation nucleation and non-conservative motion that restricts tantalum.

Little work has been carried out on the effect of pulse duration on the shock response of bcc metals in general and tantalum in particular. What work has been carried out on bcc metals, such as molybdenum, has been at much higher peak shock pressures than are under discussion in this report [81]. Those investigations found that an increase in pulse duration cause an increase in twinning density in the material, which would result in an increase in hardness. These conclusions can be largely discounted when discussing the current results. Not only are the shock pressures under discussion lower than the expected twinning nucleation threshold of tantalum (and indeed, no twinning was detected in either of the shock loaded tantalum specimens), but molybdenum actually displays evidence of strain rate sensitivity [89], which is absent from tantalum.

The contrast between the STEM image of shock loaded as-received tantalum taken 3.0 mm from the impact face in Figure 4.13a and the TEM image of shock loaded as-received tantalum taken from the rear surface of the specimen in Figure 4.14 would seem to explain the difference in hardness between the middle of the specimen and the rear of the specimen. The formation of sub-grain walls is a textbook example of 3-stage hardening in tantalum and advancing stages of hardening towards the rear of the specimen would explain the hardness profile. However, the difficulty arises when trying to link the increase in hardness and the development of the sub-grain structure with the decrease in the loading duration that is the likely cause of the hardness increase in the shock loaded copper specimens. A decrease in loading duration at the same (or fractionally reduced) peak shock pressure cannot produce a better defined microstructure. This can be seen practically in the shock loaded annealed copper microstructure at the rear of the specimen. At this point it would be tempting to blame this disparity on the

bimodal grain size of the tantalum. However, it has been shown that the hardness variation across a planar surface within the shock loaded as-received tantalum specimen with plane normal to the loading direction is negligible. Unless the specimen sees a sudden change in lateral hardness distribution between the impact surface of the specimen and the rear surface it is likely that the increased hardness at the rear of the specimen is constant across the rear surface of the specimen. In which case, the microstructure observed is most likely representative of the microstructure across the rear of the specimen.

Spall plate apparatus

In order to try to understand what aspect of the spall plate apparatuses is resulting in the failure to trap the rear surface release waves, a summary of the different conditions experienced by the shocked specimens is shown in Table 4.3. The different spall plate apparatuses are described in greater detail in Section 3.1.1. The results from Table 4.3 are slightly mixed. The material under shock load does not seem to affect the likeliness of spall failure. Both of the annealed, or as-received specimens have experienced spall failure and successful captures of a rear surface release wave have only occurred in cold-rolled material. However, spall failure has also occurred in cold-rolled material. Spall failure has occurred at multiple peak shock pressures. Within the shock loaded copper set it would appear as if the design of the spall plate apparatus provides an answer, as only the thin spall apparatus has successfully captured the rear surface release wave. However, in the shock loaded tantalum specimens, the thick spall apparatus was shown to be capable of successfully capturing the rear surface release wave.

Material	Pre-shock processing	Peak Shock Pressure (GPa)	Spall plate apparatus	Spall plate failure (Y\N)
Tantalum	As-received	7.20	Thick spall	Y
Tantalum	Cold-rolled	7.20	Thick spall	N
Copper	Annealed	5.08	Thick spall	Y
Copper	Cold-rolled	5.87	Thin spall	Y
Copper	Cold-rolled	5.96	Cup	N
Copper	Cold-rolled	9.60	Cup	Y

Table 4.3: *Summary of loading conditions for shock loaded specimens, including whether the spall apparatus used was successful, or not.*

The only consistent conclusion that can be drawn from Table 4.3 is that different spall plate apparatuses require different levels of care when implementing their designs. The thin spall apparatus has been the most consistent; the thick spall has provided both good and bad results and the cup apparatus has failed for every specimen investigated. However, the lack of repeat experiments for the thin spall apparatus and the small sample sizes for the other two mean that this conclusion must be taken with a grain of salt.

4.3 Conclusions

In order to investigate the effect of cold-rolling on the mechanical and microstructural response of copper and tantalum, a series of copper and tantalum specimens were subjected to plate impact experiments. An annealed copper specimen was shock loaded to a peak pressure of 5.08 GPa. The cold-rolled copper specimens were shock loaded to peak pressures of 5.87 GPa, 5.96 GPa and 9.60 GPa. Both of the shock loaded tantalum specimens were shock loaded to a peak pressure of 7.20 GPa. Momentum trapping apparatus, consisting of lateral momentum trapping rings and spall plates, was used to prevent lateral release waves and release waves from the rear of the shocked specimens from entering the specimens.

Compression tests on the shock loaded copper and tantalum specimens were carried out to investigate the effect of cold-rolling on the path dependence of the two materials. It was found that shock loaded cold-rolled copper shows much reduced path dependence, in contrast to shock loaded annealed copper. This was attributed to the inability of cold-rolled copper to experience the same kind of complete change in microstructure at relatively low strains that shock loaded annealed copper does and the movement of pre-existing dislocations to accommodate strain applied via a shock wave. Some strain rate sensitivity is observed, which is thought to have arisen from the dislocation free cell interiors. Shock loaded cold-rolled tantalum also displays no path dependence, matching the behaviour of the shock loaded as-received tantalum. However, it was observed that both of the shock loaded tantalum specimens showed a drop in the yield stress when compared to the flow stress of their unshocked material at equivalent strains. It was posited that this drop was due to the freeing up of pinned dislocations, and the creation of new, unpinned dislocations during shock.

Hardness maps of the shock loaded copper and tantalum specimens were created in order to check the efficacy of the lateral momentum traps. The absence of a ring of increased hardness around the outside diameter of any of the shocked specimens is taken as confirmation that the lateral momentum traps had succeeded in preventing the lateral release waves from entering the specimens. There is no discernible difference between the various shock loaded copper specimens. The main difference between the hardness

mapping for the copper and tantalum specimens is the existence of varying areas of hardness in the shock loaded tantalum specimens. These variations are negligible in the shock loaded as-received specimens, but in the shock loaded cold-rolled specimens they contribute to a significant deviation from the mean. This is taken to be a result of the known tendency of tantalum to form a bimodal grain size structure after grain refinement.

Hardness profiles of the shock loaded copper and tantalum specimens were created in order to confirm that the specimens had experienced the same loading cycle through their entire thickness. It was found that a series of specimens (including the shock loaded annealed copper, shock loaded cold-rolled copper shock loaded to peak pressures of 5.87 GPa and 9.60 GPa and the shock loaded as-received tantalum) displayed a linear increase in hardness beginning at a point 3 mm from the impact face and continuing to the rear surface of the specimens. Investigations into the wave behaviour within the specimens with and without spall plates found that the point at which the increase in hardness began coincided with the spall plane of the specimens. In addition to this, it was found that the hardness increase was inversely proportional to the loading duration of the shock pulse. This was confirmed by microstructural analysis, which found that the dislocation structure at the rear of the shock loaded annealed copper specimen displayed a reduced dislocation cell diameter and less well defined cell walls, which has been previously linked with a decrease in shock loading duration [88]. The behaviour of tantalum in this regime is less well understood. While the microstructure observed at the rear of the shock loaded as-received tantalum specimen does match the increase in hardness, it is unclear how a decrease in loading duration would have produced this microstructure.

It has also been confirmed that both shock loaded copper and tantalum specimens experience shock wave attenuation during loading. However, it was observed that cold-rolling the copper prior to shock seemed to remove or decrease this behaviour.

Chapter 5

The effect of strain rate and temperature on compression of tantalum

5.1 Results

A series of compression tests on tantalum were carried out by Dr. Alex Worley (at the time a PhD student), Dr. Paul Hooper and Prof. John Dear of the Department of Mechanical Engineering, Imperial College London with the assistance of Dr. Jeremy Millett and Mr. Glenn Whiteman of AWE, Aldermaston. The tantalum samples were compressed at a range of strain rates and temperatures to investigate the mechanical response of tantalum under different loading conditions. The stress-strain curves obtained from these samples have not been previously investigated. For this thesis these samples were then investigated using hardness testing and electron microscopy to determine the post-deformation behaviour of tantalum. The tantalum used for these samples is the same as the as-received tantalum shown in Figure 4.8 in Section 4.1.2.

The naming convention adopted here is the sample element followed by the power in the strain rate, and the temperature the compression was carried out at. This is to aid in the identification of sample deformation conditions; a summary of the compression conditions alongside the sample names can be found in Table 5.2.

5.1.1 Stress-Strain Curves

The stress-strain curves obtained from the quasi-statically compressed tantalum can be seen in Figure 5.1. The yield strength of the samples increases with decreasing temperature and increasing strain rate. The increase in yield strength is greater for an increase in temperature from 20°C to 170°C than it is for a decrease in strain rate from 10^{-1} s^{-1} to 10^{-3} s^{-1}. Although the compressions carried out at different strain rates at constant temperatures result in different yield strengths, the two stress-strain curves for Ta-120 and Ta-320 overlap towards the end of the curve. Pronounced shoulders can be seen on all four stress-strain curves. These curves become less pronounced with increasing temperature during compression.

The yield strengths and the stresses applied at the highest strain achieved for the compressed samples can be found alongside the average hardnesses of the samples post-compression in Table 5.1.

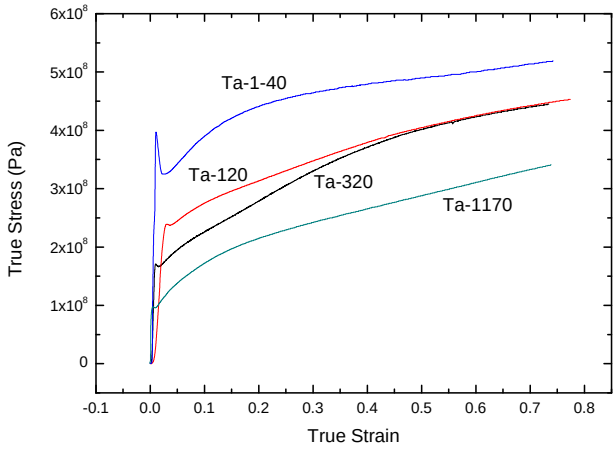

Figure 5.1: *Stress strain curves for compressed tantalum samples under a range of loading conditions. Data obtained by Worley* et al.

		$\dot{\epsilon} \rightarrow$		
		10^{-3} s^{-1}	10^{-1} s^{-1}	2×10^{3} s^{-1}
↑	170°C		152	
T	20°C	157	141	126
	-40°C		140	
	HV			
↑	170°C		350	
T	20°C	440	440	
	-40°C		520	
	MPa(σ_F)			
↑	170°C		100	
T	20°C	170	240	620
	-40°C		400	
	MPa(σ_Y)			

Table 5.1: *Average hardnesses obtained from the compressed tantalum samples. The stress applied at the highest strain achieved (σ_F) and the yield stresses (σ_Y) of the compressed tantalum samples measured during compression.*

5.1.2 Hardness

Hardness maps of the full circular cross-section of each of the compressed samples mentioned in Section 3.1.2 were obtained. The average hardnesses of each sample can be found in Table 5.2 along with the hardness range and the results of a χ^2 test with the hypothesis that the hardness was equal to the average and constant across the sample.

The average hardness values can be seen to fall into three distinct groups. sample Ta320 has the lowest hardness, followed by the group of Ta-1-40 and Ta-120, and the group of Ta-1170 and Ta-320 has the highest. The results of the χ^2 test to investi-

Sample Label	Strain %	Strain Rate (s^{-1})	Temperature (°C)	Vickers Hardness (HV)	Hardness Range (HV)	χ^2
Ta-320	70	10^{-3}	20	157.25±15	95	0.0
Ta-120	70	10^{-1}	20	141.21±16	86	0.0
Ta-1-40	70	10^{-1}	-40	140.19±13	82	0.01
Ta-1170	70	10^{-1}	170	152.24±12	81	0.93
Ta320	19	2×10^{3}	20	126.22±9	72	1.0

Table 5.2: *Average hardnesses obtained from the compressed tantalum samples. Hardness range refers to the difference between the maximum and minimum hardnesses measured. The hypothesis for the χ^2 distribution was that the hardness was constant across the sample and equal to the average hardness.*

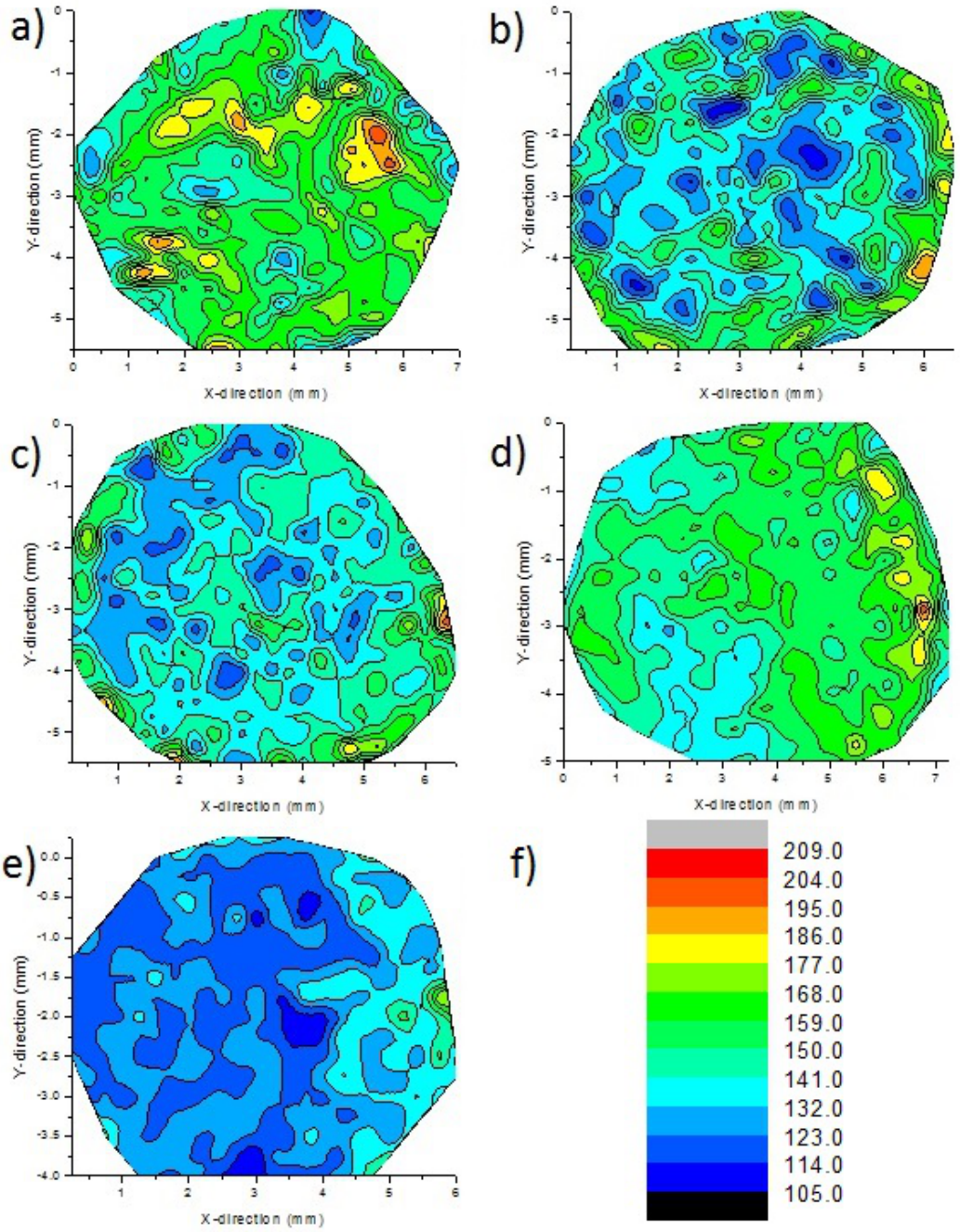

Figure 5.2: *Vickers hardness contours of compressed tantalum samples. a) Ta-320, b) Ta-120, c) Ta-1-40, d) Ta-1170, e) Ta320 and f) the key. The range of hardness used in the contours was kept constant for all samples to allow for better comparison. The distance between each measurement in both the x- and y-axis was 250 μm.*

gate whether the hardness is constant over the cross-sectional area of the samples reveal that the lower strain rate and lower temperature samples (Ta-120, Ta-1-40 and Ta-320) have a very inhomogeneous hardness distribution. In contrast, the higher temperature, low strain rate sample (Ta-1170) and the high strain rate sample (Ta320) have a largely constant hardness. These hardness distributions can be seen reflected in the hardness contour maps shown in Figure 5.2. Both Figures 5.2d and 5.2e show a largely homogeneous hardness distribution aside from some hardness variation towards the right hand side of the figures. This is likely due to the sample surface and the compression platen, or incident bar not being perfectly parallel to each other. In contrast, Figures 5.2a, 5.2b and 5.2c show localised peaks in hardness.

5.1.3 Back Scattered Electron Images

The compressed tantalum samples were imaged using BSE in part to avoid the necessity of using a highly concentrated HF solution to etch the samples and also to obtain a wider view of the microstructure within the tantalum grains than is possible under STEM.

The images in Figures 5.3 and 5.4 show representative microstructures of the compressed tantalum samples at around 650 times magnification and around 2110 times magnification respectively. Figures 5.3b, 5.3c, 5.3e and to a lesser extent 5.3a show the presence of strain gradients in grains throughout the sample. These features are present in all of the room temperature and lower samples, but are absent from sample Ta-1170 in Figure 5.3d. Figures 5.4b and 5.4c show sub-grain structures, with long, thin, parallel sub-grains spanning the width of the grains throughout samples Ta-120 and Ta-1-40. This parallel sub-grain structure is present in sample Ta-320, as seen in Figure 5.4a, but the sub-grain walls see a larger degree of variation from a straight line than in Figures 5.4b and 5.4c. Figure 5.4d shows a sub-grain structure in the higher temperature Ta-1170 sample, but lacking the distinctly parallel nature of the sub-grains present in Figures 5.4b and 5.4c. Sample Ta320 does not display at all the kind of sub grain structure present in the other samples. It can be seen in Figure 5.3e and 5.4e that Ta320 contains multiple twins throughout the sample.

The contrast present in Figures 5.3 and 5.4 emerges from the sensitivity of the BSE intensity to crystal orientation near the Bragg angle. The BSE intensity reaches a minimum close to the Bragg angle, so the BSE intensity will increase as the orientation moves away from this minimum point until the BSE intensity plateaus. In the context of grains containing a strain gradient and therefore varying degrees of mis-orientation across the grain, this will result in a varying BSE intensity dependent on the orientation of the grain, provided that the crystal orientation is close to the Bragg angle.

5.1.4 Scanning Transmission Electron Microscopy

The FIB samples were obtained from the centre of the compressed tantalum samples, with the film normal parallel to the radial axis of the cylindrical samples. See Figure 3.5 for a schematic diagram.

The Scanning Transmission Electron Microscope images in Figure 5.5 all show increased dislocation density when compared to the initial as-received material as seen in Figure 4.8. After this they fall into three distinct groups: Figures 5.5a-c, which correspond to samples Ta-320, Ta-120 and Ta-1-40, show a series of parallel, dense dislocation cell walls bordering long, thin sub-grains. The spacing between sub-grain walls has some variation between samples and within the same sample, but the average spacing is of the order of 100s of nanometres. This matches the size of the sub-grains shown in Figures 5.4a and 5.4b. The spacing of the original dislocation tangle walls was 660 nm, so there has been some reduction in the wall spacing during deformation. New dislocations have formed between the sub-grain walls and, in some cases, are beginning to form new dislocation walls. Figure 5.5d shows sample Ta-1170, which contains the same kind of dense sub-grain walls, but not regular and parallel as the other low strain rate samples. New dislocations are also present within the interior of these sub-grains and the formation of new dislocation cell walls appears to be more advanced than in the lower temperature, lower strain-rate samples. Finally, the SHPB sample seen in Figure 5.5e is entirely lacking the dense sub-grain walls seen in the other samples. Instead, traces of the pre-existing loose dislocation walls can be seen, obscured by the newly formed dislocations present.

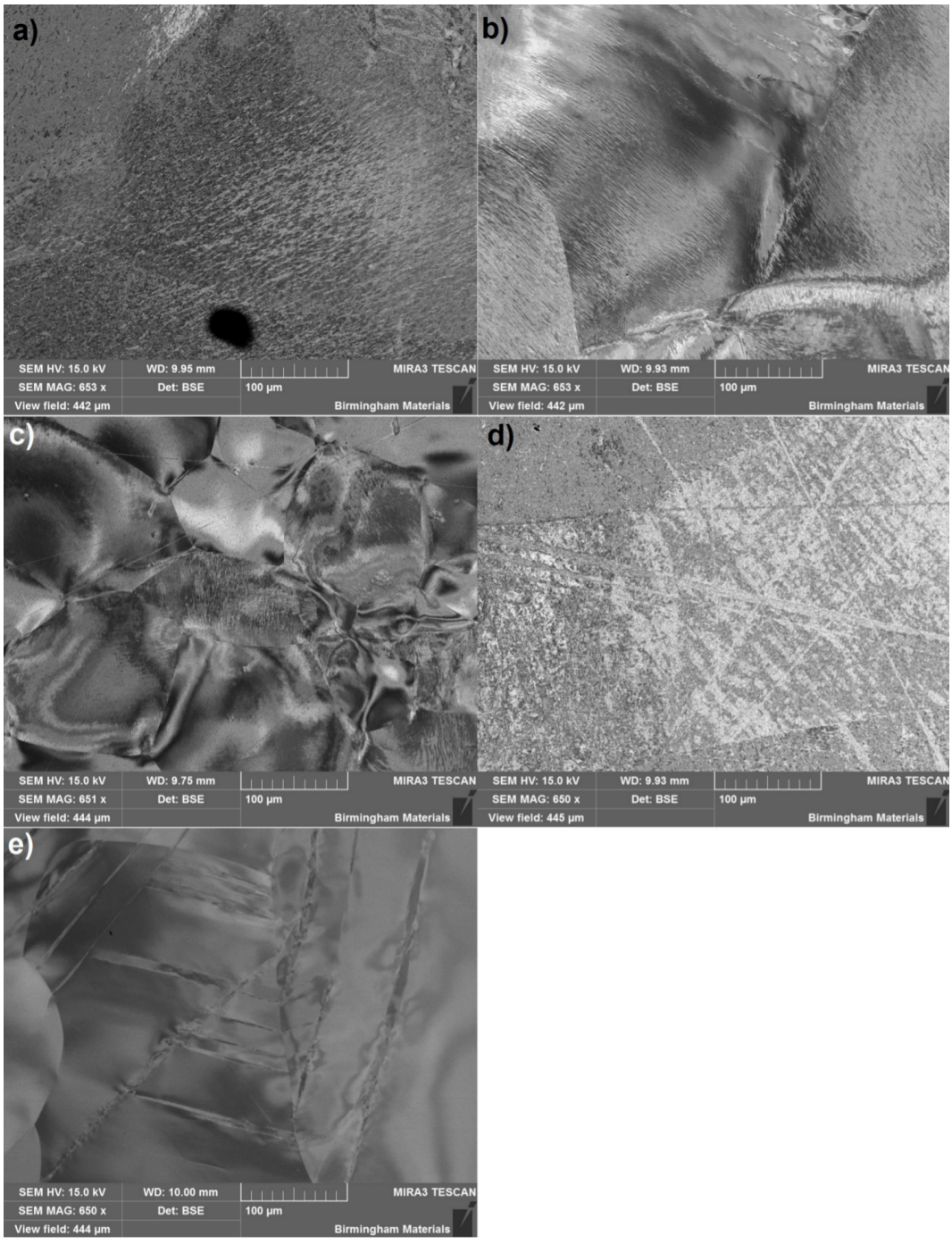

Figure 5.3: *Back scattered electron images of compressed tantalum samples. a) Ta-320, b) Ta-120, c) Ta-1-40, d) Ta-1170 and e) Ta320.*

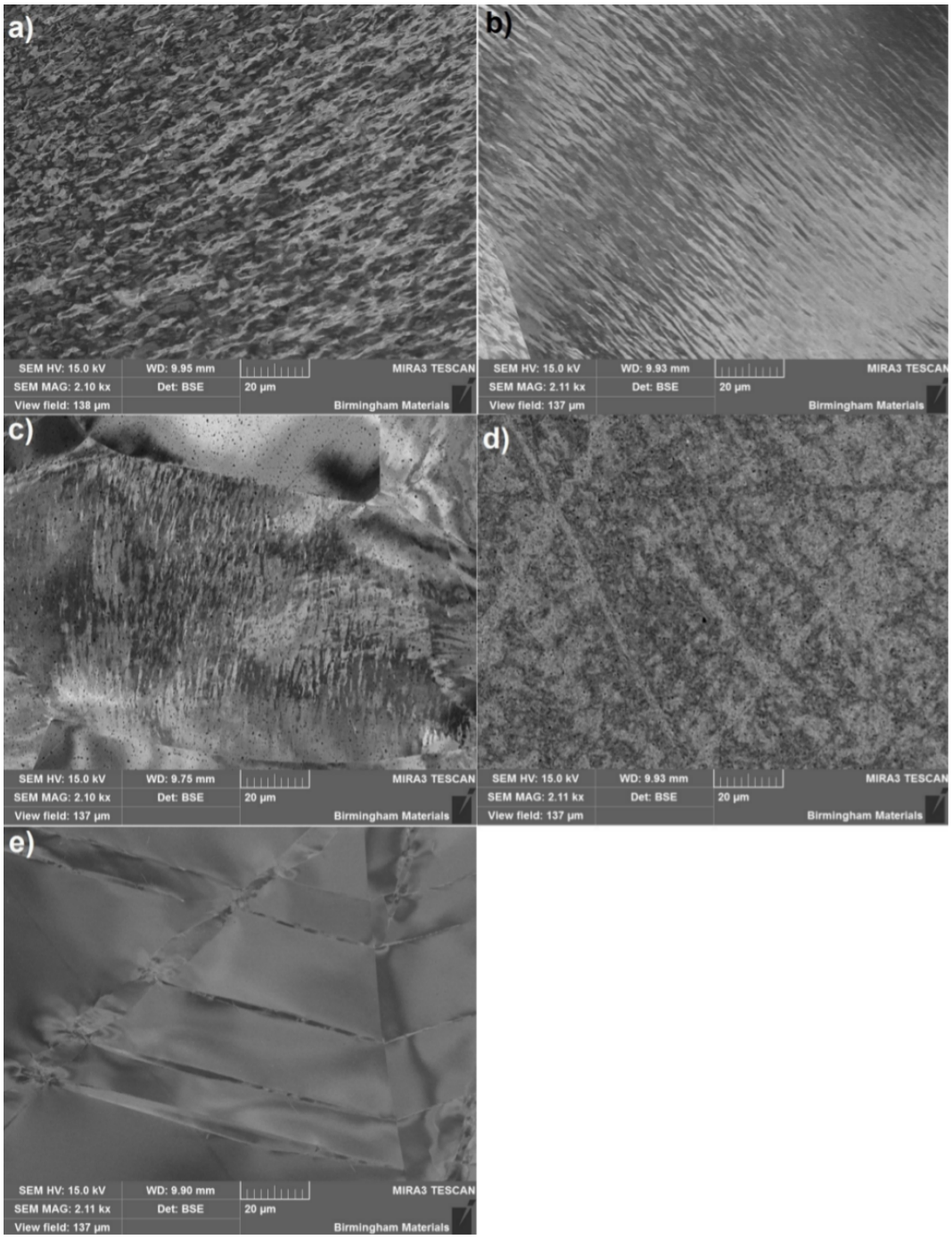

Figure 5.4: *Back scattered electron images of compressed tantalum samples. a) Ta-320, b) Ta-120, c) Ta-1-40, d) Ta-1170 and e) Ta320.*

5.1.5 Transmission Kikuchi Diffraction

TKD was used to measure the mis-orientation angle (MA) between the sub-grains formed in the compressed tantalum samples. The FIB samples taken from samples Ta-120 and Ta-320 were investigated. MAs were measured for seven sub-grain boundaries in Ta-120

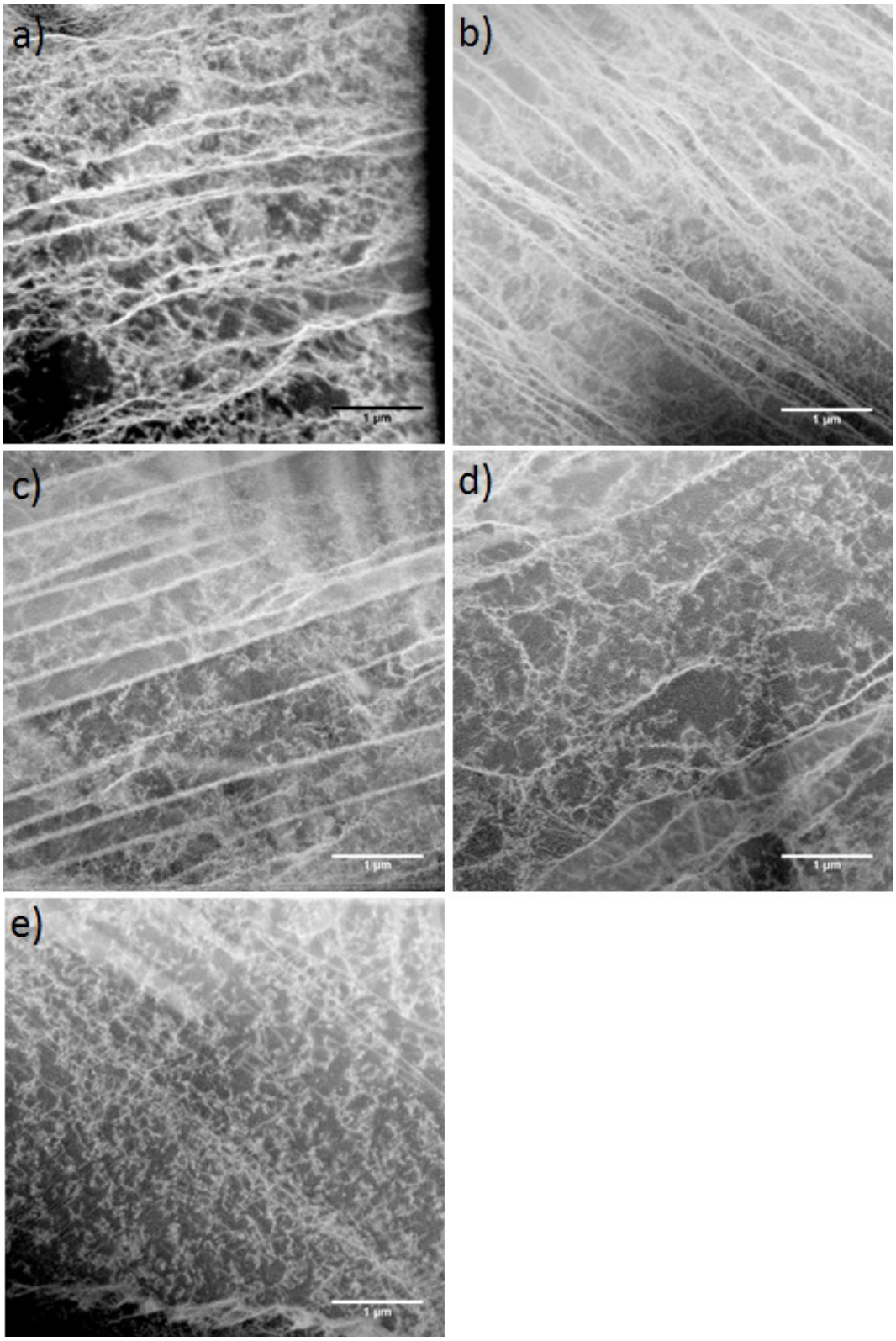

Figure 5.5: *Scanning Transmission Electron Microscopy images of compressed tantalum samples. a) Ta-320, b) Ta-120, c) Ta-1-40, d) Ta-1170 and e) Ta320. The STEM samples were prepared using a FIB capable SEM.*

and Ta-320. These are: $\text{MA}_{Ta-320} = 3.25^\circ$ and $\text{MA}_{Ta-120} = 3.01^\circ$. This confirms that the sub-grain walls are very low angle grain boundaries.

5.1.6 Electron Backscatter Diffraction

EBSD was used to measure grain size variations in the compressed tantalum samples. This decision was made to avoid the necessity of using highly concentrated hydrofluoric acid for sample etching. EBSD maps of the compressed samples can be seen in Figure 5.6. The first thing that is immediately apparent is that the grain sizes vary substantially between the five tantalum samples. The largest grains are present in the Ta-320 sample in Figure 5.6a, which are in excess of 1600 μm. In contrast, the smallest grains are present in the Ta-1-40 sample seen in Figure 5.6c, which are 136 μm. Under certain rolling and grain refinement conditions, Ta can develop a bimodal grain structure [80], so it is likely that the grain size variation observed was present in the samples prior to compression. Unfortunately, the samples were only available for investigation using electron microscopy after compression had taken place, so no grain size investigation of the undeformed samples was possible.

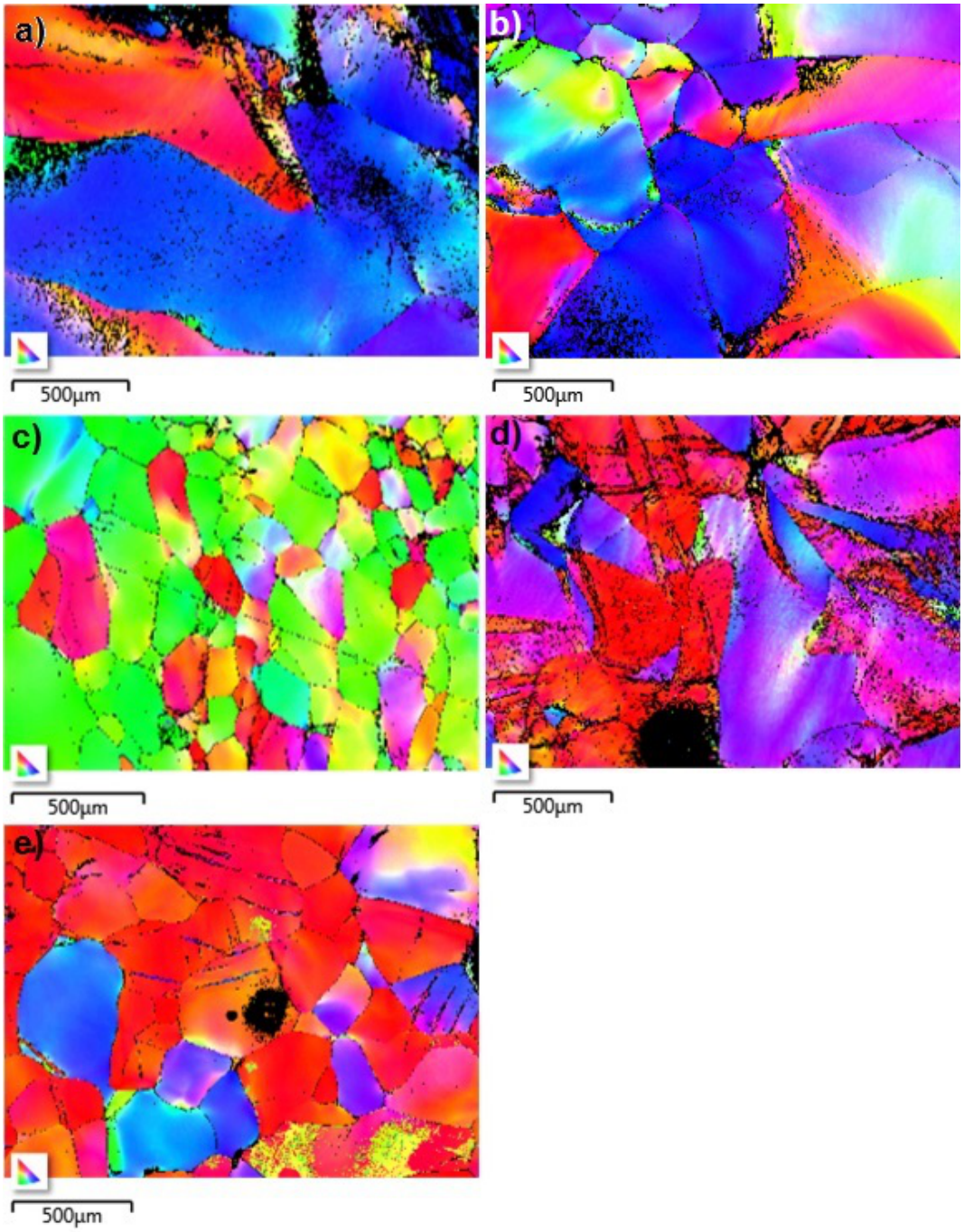

Figure 5.6: *EBSD maps of compressed tantalum samples. a) Ta-320, b) Ta-120, c) Ta-1-40, d) Ta-1170 and e) Ta320.*

5.1.7 Results Summary

A decrease in strain rate resulted in an increase in average hardness. Decreasing the temperature during loading resulted in a decrease in hardness. Hardness maps displayed homogeneous hardness for SHPB compression and for compression at higher temperature. Lower temperature quasi-static loading produced inhomogeneous hardness maps.

BSE imaging shows variations in microstructure on the larger scale. Ta-120 and Ta-1-40 have regular, parallel sub-grain walls across the width of their grains. Ta-320 has sub-grains across the width of its grains, but lacking some of the straight parallel nature of those seen in Ta-120 and Ta-1-40. Ta-1170 shows some orientation contrast pointing to the existence of sub-grains, but nowhere near as obvious or as regimented as the lower temperature quasi-statically loaded samples. Ta320 shows twinning throughout and no evidence of sub-grains.

STEM was used to investigate the dislocation microstructure of the compressed tantalum samples. Ta-320, Ta-120 and Ta-1-40 showed parallel sub-grain walls with dislocations present within the sub grains. Ta-1170 showed sub-grains, but lacking some of the parallel nature of the lower temperature samples and better defined dislocation cells forming within the sub-grains. Ta320 showed pre-existing dislocation walls which have not tightened into sub-grain walls and homogeneous dislocations generated during deformation.

5.2 Discussion

A series of polycrystalline tantalum samples were subjected to compression under a range of different strain rates and temperatures. The samples were then investigated to determine the effect of strain rate and temperature on the development of the microstructures of the samples. A summary of the loading conditions of the samples, along with the naming convention used can be found in Table 5.2. The starting material for the compressed samples is the same as the unshocked as-received tantalum discussed in the previous chapter. The microstructure for this starting material is shown in Figure 4.8a.

The dislocation microstructures of the five samples under investigation fall into three rough categories. Ta-320, Ta-120 and Ta-1-40 all show very similar parallel sub-grain walls in Figures 5.3a-c and 5.4a-c, with Ta-320 acting as a slight outsider, with a less well defined parallel structure. Ta-1170 shows some sub-grain development, but non-parallel and lacking the well-defined orientation contrast seen in the previous three samples, as shown in Figures 5.3d and 5.4d. Finally, Ta320, the SHPB impacted sample, shows no evidence of sub-grain development and displays profuse twinning throughout the sample, as shown in Figures 5.4e and 5.3e.

5.2.1 Explaining the Differences Between the Quasi-Statically Compressed Tantalum Samples

After deformation, Ta-1-40, Ta-320 and Ta-120 all show the same kind of microstructure. The parallel dislocation tangle walls observed in the starting material have tightened into parallel sub-grain walls. In addition, further dislocation generation has occurred within the sub-grains, resulting in a larger density of the straight dislocations and dislocation debris that is characteristic of tantalum deformation. All three samples have very similar sub-grain widths, which are hundreds of nanometres across, slightly narrower than the dislocation tangle walls observed in the starting material, but still of the same order of magnitude. This is consistent with the three-stage hardening process in tantalum proceeding from the starting material microstructure of long dislocation tangle walls.

From Figures 5.3a-c and 5.4a-c, it can be seen that these sub-grains are long, stretching across the entire width of a single grain, or a large portion thereof. In contrast, the sub-grain walls observed in Ta-1170 are less regular and parallel than those observed in the lower temperature deformation samples and the dislocations generated within the sub-grains have begun to form dislocation cell walls. From the BSE image in Figure 5.4d the sub-grains in Ta-1170 are less sharply defined, suggesting that the sub-grain walls in Ta-1170 represent a smaller mis-orientation than the other quasi-static compression samples and that a larger degree of the plastic strain has been accommodated by the dislocation generation and the formation of dislocation tangle walls within the sub-grains. This is likely a result of the increased thermal energy allowing the dislocations and sub-grain walls to overcome the high Peierls barrier to the movement of screw dislocations in tantalum and attain a greater degree of mobility.

The stress-strain curves obtained from the quasi-statically compressed tantalum samples shown in Figure 5.1 display the increase in yield strength with increasing strain rate and decreasing temperature expected from the literature. Both the strain rate sensitivity and the temperature sensitivity have been said to result from the high Peierls stress and the high dislocation drag coefficient in tantalum and other bcc metals. In addition, work by Carpenter and Baker [90] suggests that the dislocation-interstitial interaction is also responsible for a degree of the yield strength's sensitivity to temperature. Smialek and Mitchell [91] found that the introduction of interstitials, namely carbon, oxygen and nitrogen, affected the temperature sensitivity of the yield strength in tantalum at temperatures less than 170°C. Effectively, an increase in temperature makes it easier to overcome thermal activation barriers to dislocation motion. In terms of strain rate sensitivity, Stainier *et al.* [92] put forward a model that described the effect of an increase in temperature and strain rate on the the Peierls stress in a material. Peierls stress decreased with increasing temperature up to a critical value, at which Peierls stress becomes constant. Increasing the strain rate has the effect of raising this critical temperature, effectively performing the same function as decreasing the temperature of the material.

The upper and lower yield points in the stress-strain curve of Ta-1-40 emerge

from the same factors that produced the same upper and lower yield points in the stress-strain curves for the as-received tantalum, as discussed in Chapter 4. The presence of pinning interstitials in the material requires that the dislocations first break free from the interstitials before plastic deformation can take place. An increase in the temperature during deformation can be seen to have the effect of reducing the difference between these yield points until they merge into a single point in Ta-1170. This is a result of an increase in thermal energy helping the dislocations to break free from their pinning interstitials. This effect is similar to that seen in the cold-rolled tantalum stress-strain curves observed in Chapter 4, except via increased temperature, not cold-rolling.

The stress-strain curves of Ta-120 and Ta-320 also show an interesting feature. After an initial difference in yield strength (attributed to the link between strain rate and yield strength discussed above) the two curves merge at around 45% strain. This suggests that the increased loading time experienced by Ta-320 results in an increased work hardening rate relative to Ta-120. However, this does not result in the Ta-320 stress-strain curve overtaking the Ta-120 curve; instead, the two curves merge and follow the same path. This suggests that the end point for a stress-strain curve in a tantalum sample (with a specific starting microstructure) is linked to the temperature during deformation.

The hardnesses of the quasi-statically compressed tantalum samples fall into two groups despite all four samples having been subjected to the same degree of plastic strain: Ta-140 and Ta-120 have hardnesses around 45 HV and Ta-320 and Ta-1170 have hardnesses around 55 HV. This initially seems unusual, as an increase in σ_Y and σ_F between samples does not translate into an increase in hardness in the final material. The same is true of samples with the same σ_F. However, this can be explained by the pinning of dislocations by interstitials. The effect of temperature on the migration of interstitials to dislocations is investigated by Carpenter and Baker, by measuring the damping rate of oscillation achieved by a sample held in tension and then release [90]. They found that two types of interstitial-dislocation interactions occurred at two different temperature ranges within the range of 0-100°C. Between 0-25°C, the movement of interstitials to dislocations was limited to a reorganisation of nearby interstitials by

short range migration, resulting in a weak pinning of the dislocations. In contrast, temperatures between 75-100°C enabled more long range interstitial movement, resulting in much stronger pinning of the dislocations. Unfortunately, Carpenter and Baker's study did not extend to the upper and lower temperature ranges under investigation in this thesis, but it is a safe assumption that the increased temperature applied to Ta-1170 will also facilitate the kind of long distance interstitial diffusion observed at higher temperatures by Carpenter and Baker. This would explain the higher hardness observed in Ta-1170. Conversely it is likely that the reduced temperature experienced by Ta-1-40 will result in the weaker, short range interstitial migration observed at lower temperatures. It is also possible that the reduced temperature would hinder even the short range interstitial migration, resulting in an even lower hardness. This could then be offset by the smaller grain size observed in Ta-1-40 relative to Ta-120, increasing the hardness of Ta-1-40 to match T-120. Another possible explanation for the similar hardnesses of Ta-120 and Ta-1-40 is that the samples resting at room temperature for months between the compression tests and the hardness measurements allowed the short range diffusion of interstitials to dislocations to occur in the absence of an applied stress.

The difference in hardness between Ta-120 and Ta-320 can also be explained in terms of interstitial pinning. As the temperature during compression is the same for both samples, the difference in hardness must arise from the change in strain rate. During the cold-rolling applied to the tantalum starting material discussed in Chapter 4, the applied strain acts to free dislocations from their pinning interstitials, removing the upper and lower yield points in a stress-strain curve. After freeing the dislocations from interstitial pinning, the interstitials will continue to migrate through the material and will eventually interact with any dislocations they come into contact with. A lower strain rate deformation will result in the sample experiencing an applied stress for a longer period of time. This will give the interstitials more time to migrate to the dislocations and pin them.

The variation in the hardnesses of the quasi-statically compressed samples showed very different behaviour between Ta-1170 and the lower temperature samples. For Ta-1170, the hardness was found to be uniform across a circular cross-section of the sample

and equal to the average hardness of the sample. In contrast, the lower temperature quasi-statically deformed samples showed complete inhomogeneity in the hardness across the circular cross-sections. This is separated from the rest of the hardness discussion as it seems to correlate with the microstructure of the quasi-statically compressed samples. There is a direct link between the existence of the well defined sub-grains within the sample microstructure and the inhomogeneity in the hardness maps. Observing the sub-grains in Figure 5.3a-c, it can be seen that, while the sub-grains in some grains do share a common orientation along their length, other sub-grains in other grains have different orientations. This indicates that the sub-grain orientation is not simply parallel or perpendicular to the rolling used in the refinement of the tantalum, but is instead more likely determined by the direction in which the dislocation walls were geometrically necessary for each grain orientation during loading. This will then result in a variety of sub-grain orientations and potentially spacings throughout the samples for different grain orientations and would result in the large variation in hardness within the samples.

5.2.2 Why is the Split Hopkinson Pressure Bar Sample so Different?

An SHPB, which is described in greater detail in Section 2.5.5, is an apparatus for testing the response of materials to high strain rates. In this case it was used to compress the sample at a loading rate higher than quasi-static loading, but lower than the shock loading discussed in the previous chapter. From Table 5.2, the hardness of the SHPB sample is far less than for the samples compressed at a more quasi-static rate. This reduced hardness can be explained by a number of factors. Firstly and most simply, the plastic strain applied to the sample via the SHPB compression is 19%, which is substantially lower than the 70% plastic strain applied to the other, quasi-static samples. This will result in a reduction in the work hardening undergone by sample Ta320. Secondly, the increased strain rate experienced by Ta320 will have a similar effect to the increased strain rate experienced by Ta-120 with respect to Ta-320, where an increased strain rate will result in less time under loading, which will result in less time for the pinning interstitials to migrate to the dislocations in the material. This will act to decrease the hardness of the sample. Thirdly, the combination of the reduced time and the reduced strain will impede the formation of the sub-grain walls, as the amount of time available

for dislocations to migrate to the cell walls will be reduced and the total amount of dislocation motion due to plastic strain will be reduced.

Figures 5.3e, 5.4e and 5.6e show that twinning has occurred throughout Ta320. This is unusual, as the twinning nucleation peak pressure in shock loading has been found to be around 35 GPa in laser shocked monocrystalline tantalum [7], though the peak pressure pulse duration in this case would be of the order of 10 ns, potentially increasing the necessary peak pressure required for twinning nucleation. The peak pressure experienced by Ta320 in the SHPB impact is only 640 MPa. Pang *et al* [43] found that the introduction of a lateral release wave into a specimen increased the shear stress experienced by the specimen and resulted in twinning nucleation at a peak shock pressure of 6 GPa. SHPB impacts usually do not include momentum trapping apparatus and this was true for sample Ta320. However, the peak pressure introduced by the SHPB is still an order of magnitude lower than that used in previous shock experiments in which twinning nucleation has occurred.

As with sample Ta-1170, the hardness map of Ta320 shows completely homogeneous hardness across the circular cross-section of the sample. A hypothesis was postulated above that the hardness inhomogeneity was due to the sub-grain structure resulting in different hardness values from different orientations, due to different dislocation wall separations being geometrically necessary during the rolling experienced by the as-received material. If this is the case, then the lack of sub-grain walls in Ta320, which occurs due to the reduced strain and reduced loading time experienced by the sample, would explain the homogeneous hardness observed in Ta320.

5.3 Conclusions

In order to investigate the effect of varying strain rate and temperature of tantalum during compression, a series of tantalum samples were subjected to quasi-static compression at 10^{-3}s^{-1} at 20°C and at 10^{-1}s^{-1} at -40°C, 20°C and 170°C. In addition, a compression test was carried out using an SHPB at 2×10^{3}s^{-1} at 20°C.

The stress-strain curves generated by the compression tests confirmed that an increase in the strain rate and a decrease in temperature during deformation increased the yield strength of the sample during compression. An average of the sample hardnesses over their circular cross section showed that a decrease in strain rate and an increase in temperature resulted in an increase in hardness. This was thought to be due to interstitial pinning effects. An increase in temperature increased the distance that interstitials could migrate during deformation, allowing stronger pinning effects to take place. A decrease in strain rate increased the time that the samples were under compression, allowing more time for interstitials to migrate to and pin dislocations. The substantially lower hardness of Ta320 was thought to be a combination of its increased strain rate and the much lower plastic strain applied. Hardness inhomogeneity across the circular cross-section of the samples was only observed in samples that displayed a sub-grain microstructure. This led to the hypothesis that the geometrically necessary dislocation tangle walls produced during the refinement of the as-received tantalum varied with grain orientation throughout the sample, producing a change in hardness with grain orientation due to varying sub-grain wall spacing. A detailed survey of the sub-grain walls was not carried out, so this cannot be unambiguously confirmed.

The SHPB sample displayed twinning throughout the sample at peak pressures far below the twinning nucleation threshold in tantalum. The presence of twinning in the sample was tentatively attributed to the introduction of lateral release waves after loading by the SHPB, leading to an increase in the shear stress experienced by the sample, although the peak pressure applied to Ta320 was still an order of magnitude lower than previous experiments in which twinning nucleation had occurred.

Chapter 6

Shear bands generated in titanium 6Al-4V by thick walled cylinder collapse using a gas gun

6.1 Results

6.1.1 Scanning Electron Microscopy

Secondary electron (SE) images of the ASBs in the thick walled cylinder collapse specimen were taken from Orientations A and B, as defined in Figure 3.3. The beta phase appears brighter than the surrounding alpha phase. This is due to preferential etching of the alpha phase resulting in slightly raised beta phase grains. This, along with the apparent slight curvature of the beta grains results in an increase in signal brightness from the secondary electron (SE) image due to the so-called "edge effect". Backscattered electron (BSE) imaging reveals the same difference in brightness, due to the increased concentrations of the higher atomic weight elements vanadium and iron in the beta phase grains, resulting in a brighter beta phase. Figures 6.1a, 6.1b and 6.1c allow comparison of the titanium 6Al-4V microstructures outside of the ASB in both orientations. The microstructure outside the ASB in Figure 6.1 has seen far less deformation than the material within the ASB. After localisation occurs the shear bands will act to accommodate most of the strain applied during the TWC collapse. The material outside the ASB will have seen a small degree of homogeneous deformation and can

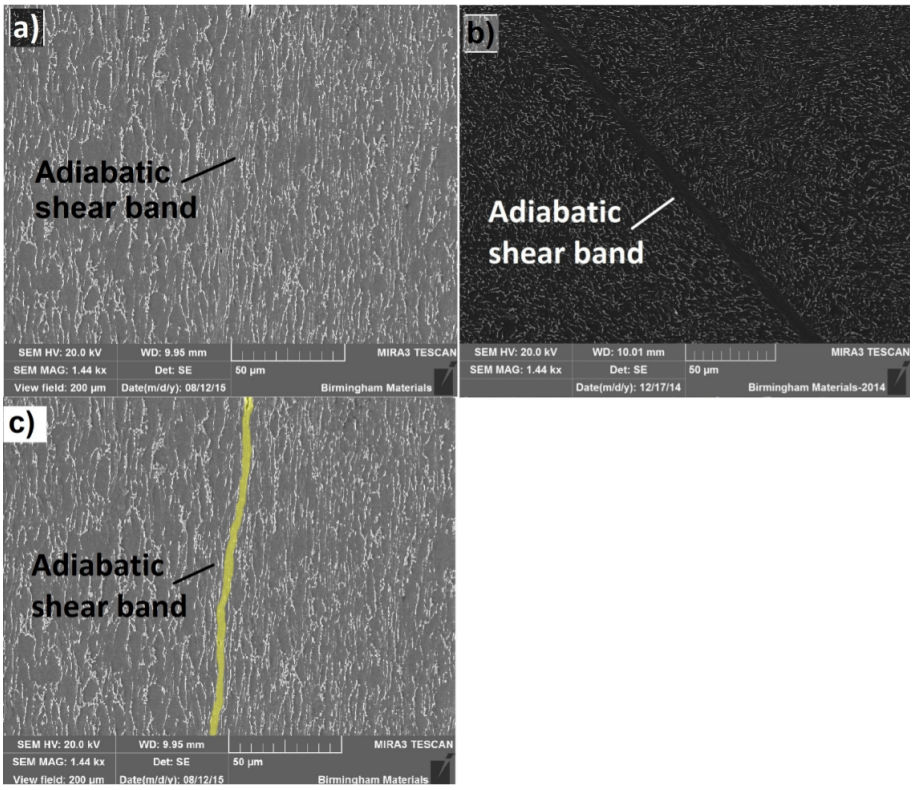

Figure 6.1: *Secondary electron SEM from two shear bands produced during the TWC collapse experiment. The lighter grains are titanium 6Al-4V beta phase and the darker grains are alpha phase. The images were taken from: a) and c) Orientation A and b) Orientation B, as defined in Figure 3.6. The image in c) contains the shear band from c) highlighted for easier detection.*

be taken as being mostly representative of the grain structure of the starting material. Figure 6.1a shows undeformed material with elliptical alpha grains. This is taken from Orientation A, which has the image normal perpendicular to the rolling direction of the original bar stock. Figure 6.1b shows undeformed material with elongated beta grains between either alpha grains, or alpha lath colonies. This is taken from Orientation B, which has the image normal parallel to the rolling direction of the original bar stock.

In Figure 6.1b the image normal is perpendicular to the propagation direction of the ASB. The sharp contrast between the ASB and the undeformed material allows clear identification of the ASB. The morphology of the ASB from this orientation is of a clean, smooth line. In contrast, the ASB observed in Figure 6.1a, from Orientation A, is more difficult to identify. The ASB was then highlighted in Figure 6.1c for easier identification. The path of the ASB also lacks the clear directionality observed in Orientation B. A 3D schematic of this effect can be seen in Figure 6.3. The ASB when

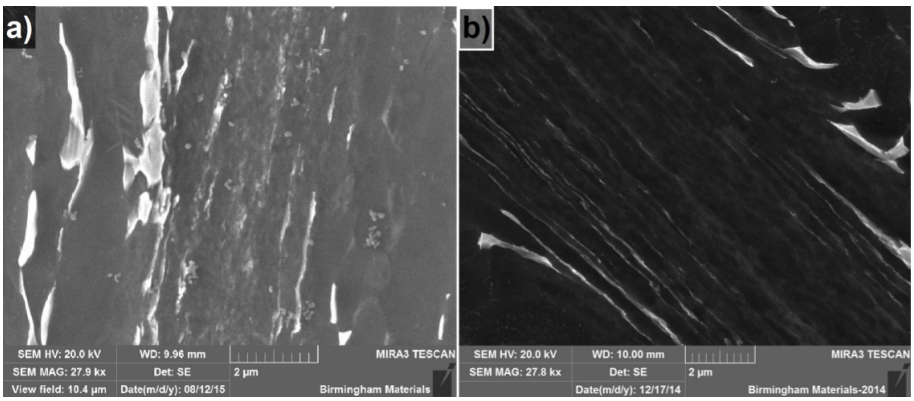

Figure 6.2: *Secondary electron SEM from two shear bands produced during the TWC collapse experiment showing the morphology of the interior of the shear bands. The lighter grains are titanium 6Al-4V beta phase and the darker grains are alpha phase. The images were taken from: a) Orientation A and b) Orientation B, as defined in Figure 3.6.*

observed from Orientation A seems to preferentially pass through alpha grains, avoiding crossing alpha-beta gain boundaries where possible.

Examining the microstructure of the ASB itself using SEM, it can be seen in

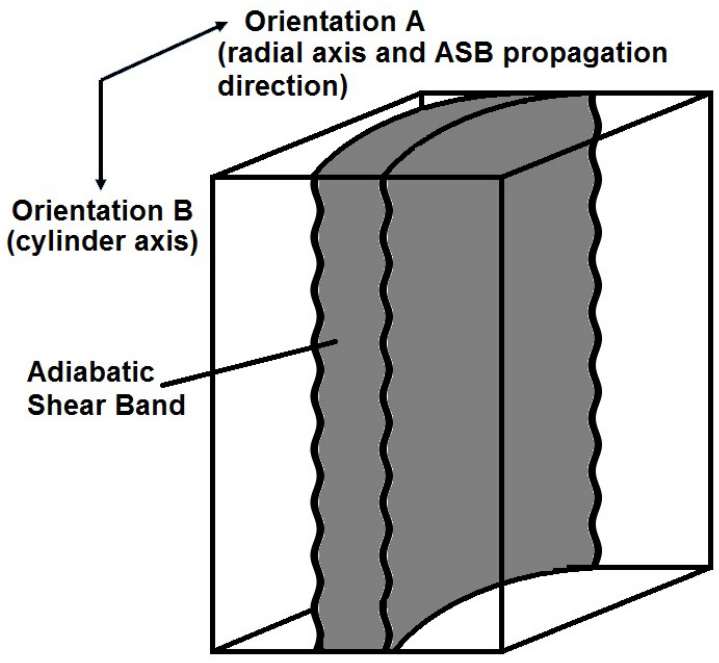

Figure 6.3: *Schematic of the overall morphology of an ASB in a TWC collapse specimen. The orientation directions used in the Figure correspond to the beam direction used when obtaining an image taken in that orientation. For example: when taking an image showing the ASB propagating along the cylindrical axis, the beam direction will be aligned with the arrow labelled as Orientation A.*

Figure 6.2b that the ASB displays the elongation of grains along the ASB propagation direction characteristic of ASBs. The sharp delineation between undeformed material and heavily deformed material within the ASB is also far more apparent at the higher magnification. Figure 6.2a completely lacks this grain elongation. The beta grains decrease in size within the ASB and become fragmented.

6.1.2 Transmission Kikuchi Diffraction

Transmission Kikuchi Diffraction (TKD) was applied to a FIB sample taken from the TWC collapse specimen from Orientation A. The orientation, phase and strain data obtained can be seen in Figure 6.4. The highly deformed nature of the ASB and difficulties with the FIB sample preparation procedure resulted in a low indexing rate for the FIB sample, but some useful conclusions can be drawn from the data obtained. Figure 6.4a displays an orientation map for alpha and beta grains inside the ASB. Multiple sub-micron sized grains are present and the sample shows no noticeable texture in the area imaged. The grain shape is largely equiaxed, though some more elongated grains are present, aligned with the rolling direction of the original bar stock and the cylindrical axis of the TWC.

In the phase map shown in Figure 6.4d the phases present can be seen to be alpha and beta, in the same proportions as the original, undeformed, material. No additional phases have been formed through the creation and propagation of the ASB. Lines of sub-micron grains of beta phase can be seen, oriented along the original bar stock loading direction. These are likely the remains of the beta grains adjacent to the elongated alpha grains observed in the undeformed material in Figure 6.1b. The orientation mapping of the beta phase in Figure 6.4b shows that the lines of sub-micron beta phase grains show no common orientation. Assuming that these beta phase grains belonged to a single beta grain with a single orientation prior to the formation of the ASB, this suggests that the beta grains have seen fragmentation and rotation during the deformation introduced during the formation of the ASB.

Figure 6.4e shows in more detail the grain morphology within the ASB. Multiple

equiaxed sub-micron grains are present throughout, along with a small number of grains of both alpha and beta, elongated in the rolling direction of the original bar stock. The average grain size in the deformed area of the sample is ≈150 nm.

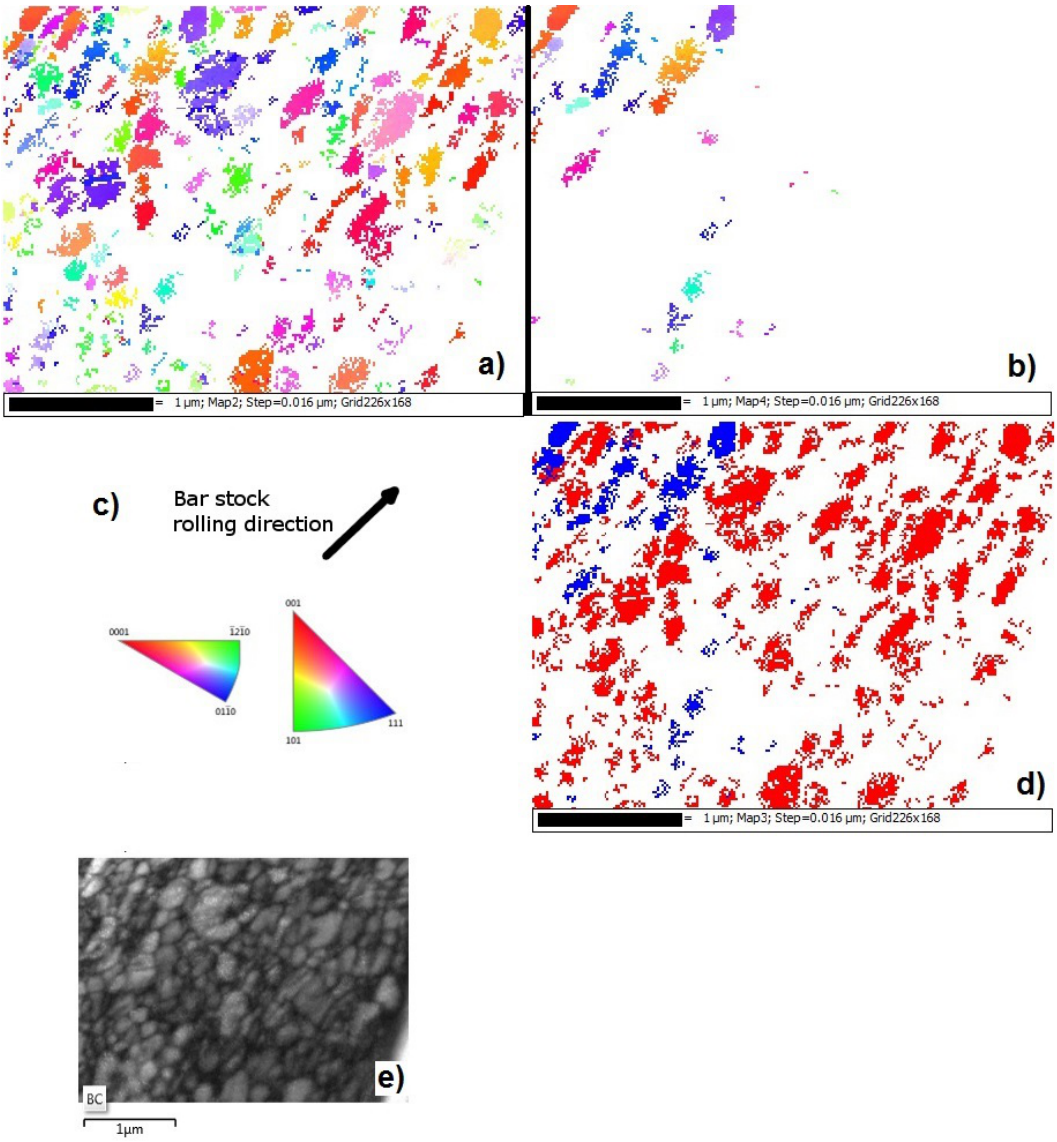

Figure 6.4: *Transmission Kikuchi Diffraction maps of a FIB sample taken from within the ASB from Orientation A, showing: a) orientation mapping of alpha and beta phases; b) orientation mapping of beta phase; c) the rolling direction of the original bar stock and the key for the orientation maps; d) phase contrast (showing alpha grains in red and beta grains in blue), and e) band contrast (or strain mapping). The radial direction of the TWC and the starting propagation direction of the ASB is parallel to the image normal.*

6.1.3 Transmission Electron Microscopy

TEM images of the ASB FIB samples can be seen in Figure 6.5. The boundary between the undeformed material and the inside of the ASB can be clearly seen on the right hand side of the ASB imaged in Figure 6.5 and less clearly (but still present) on the left hand side. These have been indicated by arrows for easier identification. The interior of the ASB appears to be composed of multiple sub-micron grains, many present as equi-axed grains, though some longer, thinner grains are present towards the outside of the ASB. However, the highly deformed nature of the material at the centre of the ASB and damage introduced by the FIB milling process make it difficult to obtain a clear low

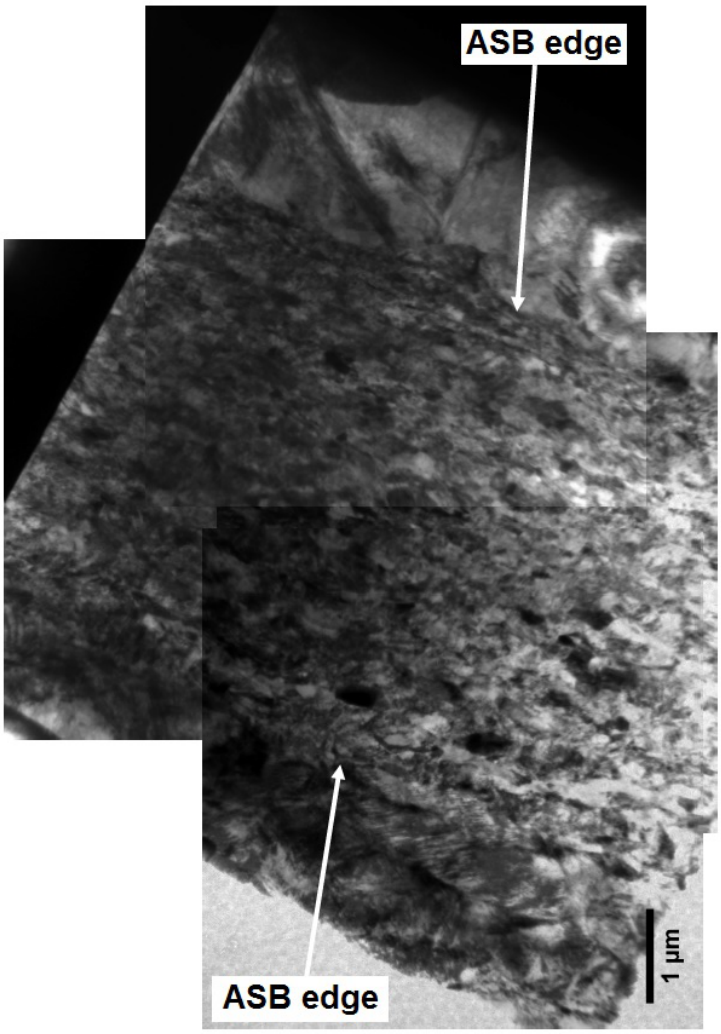

Figure 6.5: *Bright field TEM image of an ASB taken from Orientation A. The edges of the ASB are labelled for easier identification.*

magnification image. The presence of the sub-micron grains was confirmed by use of Selected Area Diffraction (SAD). An SADP was obtained using a selected area aperture that selected a circular area on the sample with diameter 790 nm. The selected area and resulting diffraction pattern can be seen in Figures 6.6a and 6.6b respectively. The SADP shows a series of rings, suggesting that multiple grains with different orientations are present within the selected area. This confirms that the grains present within the ASB are smaller than the selected area of 790 nm and that the grains present within this selected area exhibit very little texture.

Due to the nanometre scale of the grains within the ASB, it was impossible to obtain two beam conditions for the sample within the ASB. However, it was still possible to identify microstructural features within the nano-grains. While no dislocations were found in any of the grains imaged, twinning was detected throughout the heavily deformed ASB region in all of the samples. An example of the twins can be seen in Figure 6.7.

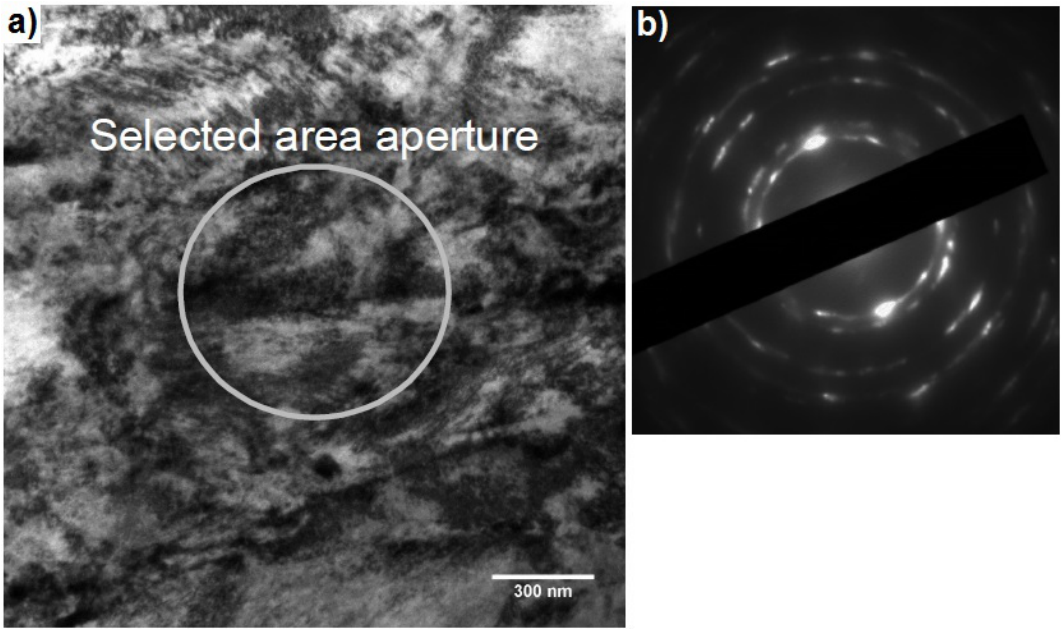

Figure 6.6: *a) Bright field TEM image showing a selected area within an ASB and b) SADP obtained from selected area shown in b).*

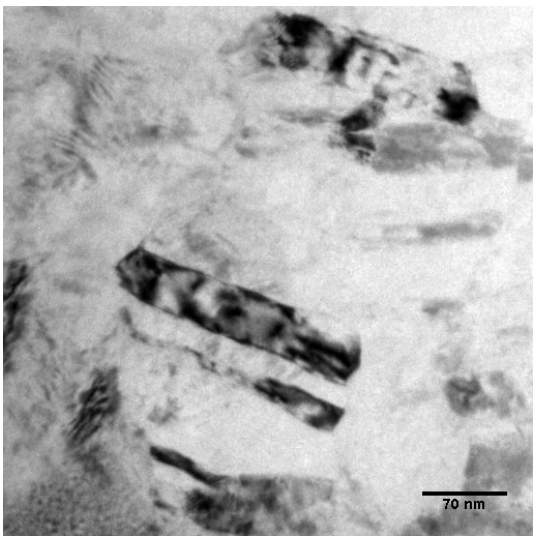

Figure 6.7: *Bright field TEM image showing a nano-grain from the interior of the ASB from Orientation A containing twins.*

6.1.4 Electron Dispersive X-ray Spectroscopy

Qualitative EDS maps were obtained using STEM from FIB samples taken from ASBs in both Orientation A and B. Figures 6.8 and 6.9 show the HAADF images, vanadium signals and aluminium signals taken at both orientations at different magnifications using an STEM. The beta phase appears as a decrease in intensity in the aluminium signal and an increase in intensity in the vanadium signal. The beta phase is also a lighter colour than the alpha grains in the HAADF STEM image, due to the higher percentage of the heavier elements vanadium and iron in the beta phase, resulting in greater scattering of the incident electrons.

Figure 6.8 shows the sample from Orientation A, which has an image normal parallel to the propagation direction of the ASB. At the outer edge of the ASB the beta grains have become much narrower than the undeformed grains outside the ASB. Within the centre of the ASB, where the material has undergone the greatest amount of strain, these grains have continued to narrow and have begun to fragment. In the EDS maps, these appear as single narrow grains. Determining orientation is impossible using EDS, but these are likely the same kind of feature as the long clusters of sub-micron beta grains observed in Figure 6.4. The sub-micron grain structure can also be seen in the STEM images shown in Figures 6.8a, 6.8d and 6.8g.

Figure 6.9 shows the sample from Orientation B, which has an image normal perpendicular to the propagation direction of the ASB. At the edge of the ASB it is clear where the path of the ASB has intersected a beta phase grain with its longest axis at an angle to the ASB propagation direction. This grain has been heavily deformed so that its longest axis now follows the propagation direction of the ASB. The resulting narrow, elongated grains continue to be present towards the centre of the ASB, increasing in density. At the very centre of the ASB, where the strain experienced by the grain is

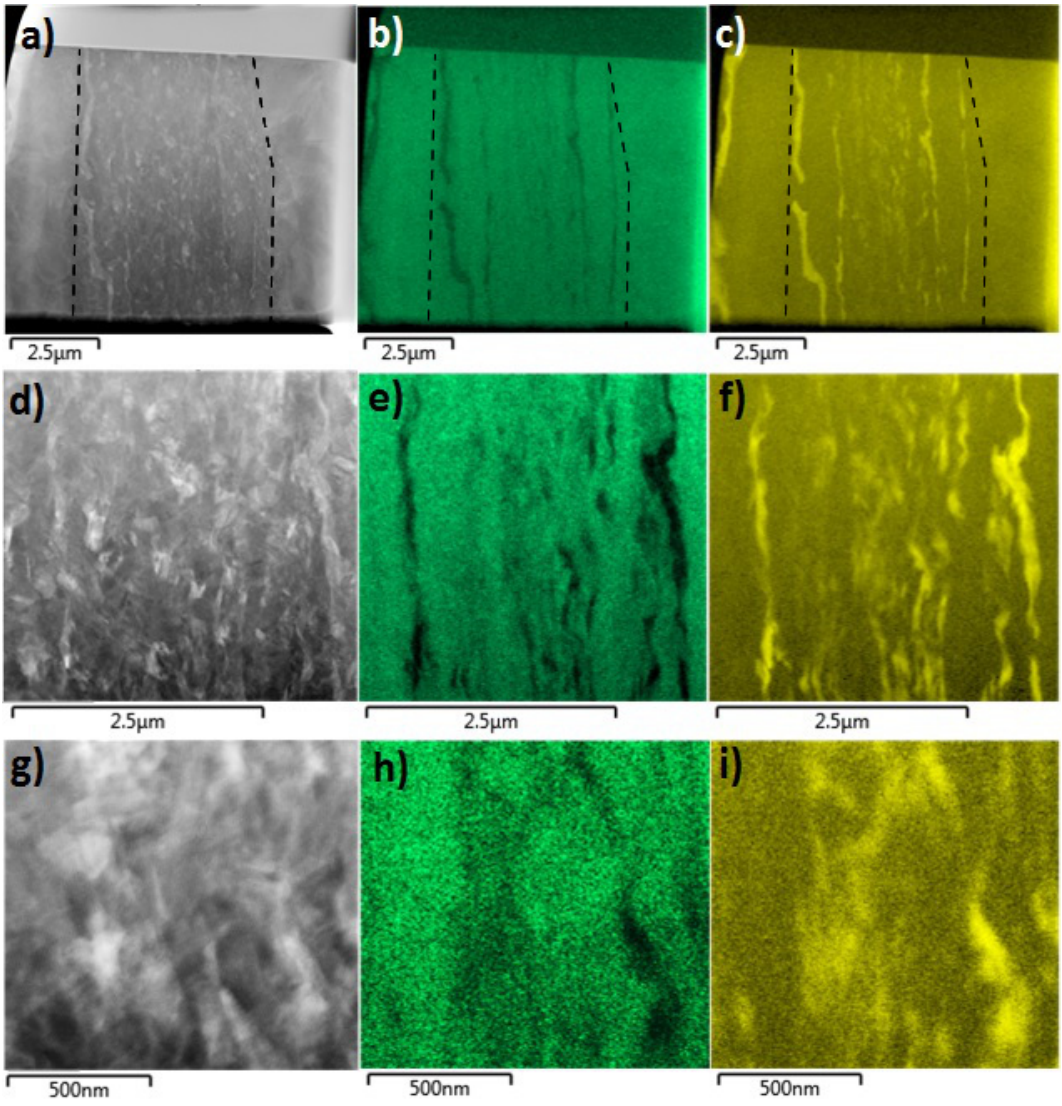

Figure 6.8: *Images taken from Orientation A using: a), d) and g) HAADF images; b), e) and h) the Aluminium signal from the EDS detector, and c), f) and i) the Vanadium signal from the EDS detector. The dashed lines in a), b) and c) show the edges of the shear band.*

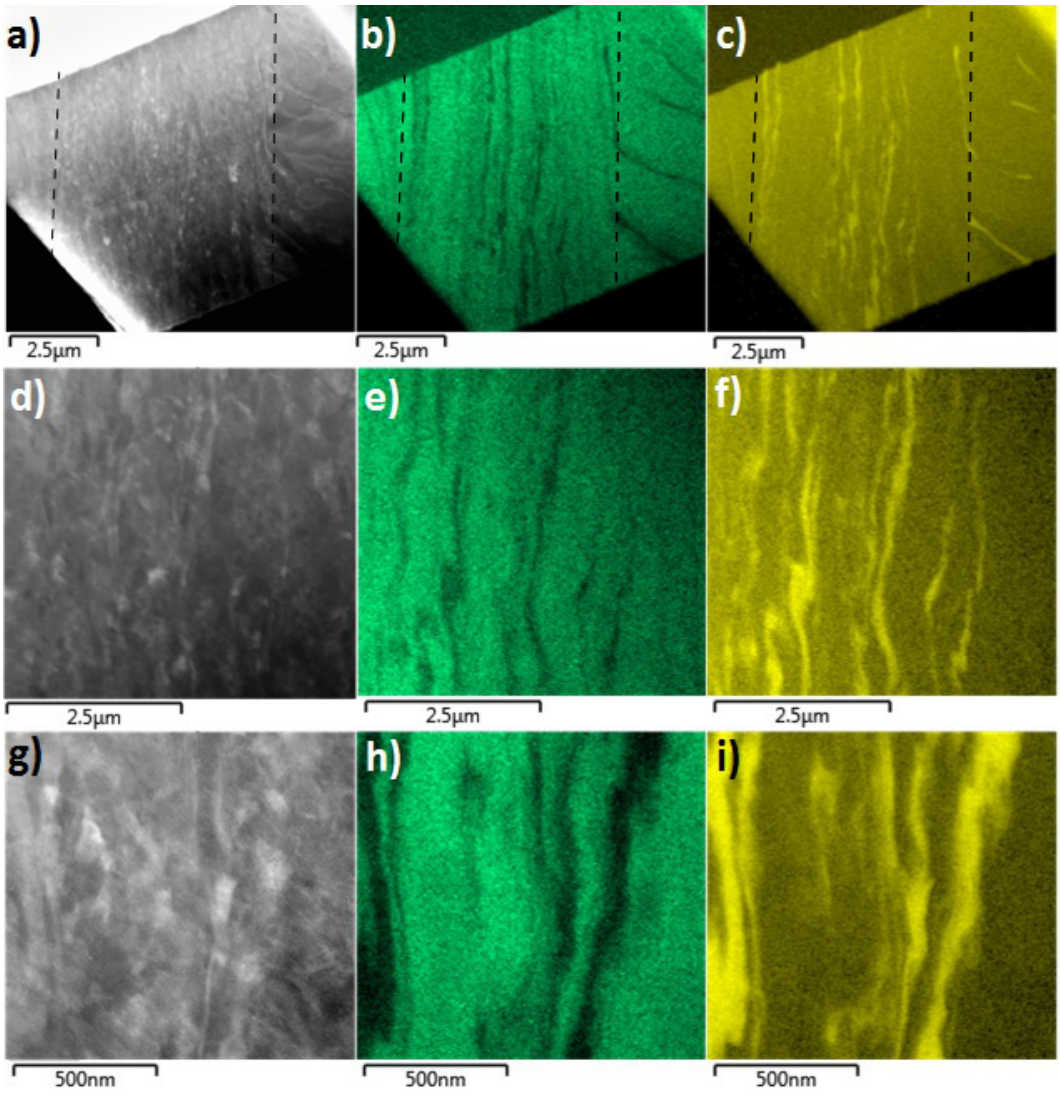

Figure 6.9: *Images taken from Orientation B using: a), d) and g) HAADF images; b), e) and h) the Aluminium signal from the EDS detector, and c), f) and i) the Vanadium signal from the EDS detector. The dashed lines in a), b) and c) show the edges of the shear band.*

highest, the beta grains become even narrower and begin to fragment. A 3D schematic derived from this data can be seen in Figure 6.10.

The microstructures visible from Orientation A and B are in some ways very similar. Both show elongated beta grains aligned with the edges of the ASB. However, this is entirely coincidental as the elongated beta grains in each orientation are generated in very different ways. The elongated beta grains seen from Orientation A are a result of the rolling direction used to produce the original titanium 6Al-4V bar stock and have become shorter and narrower within the shear band. The elongated grains seen

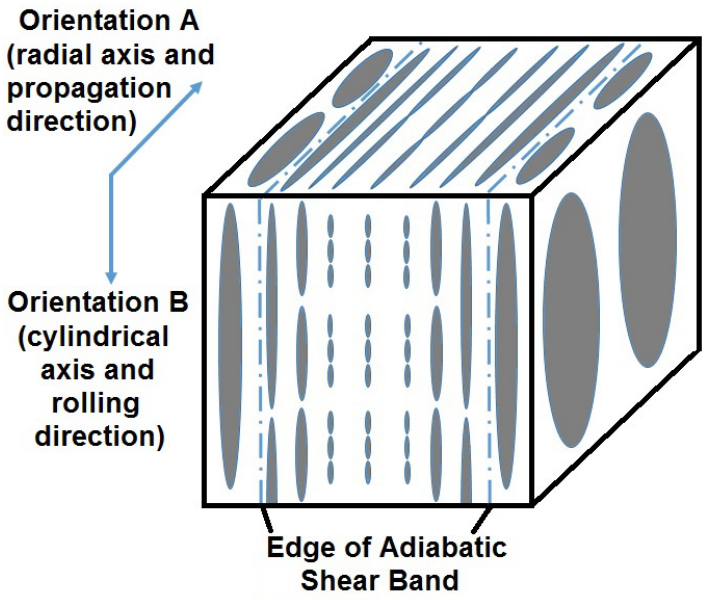

Figure 6.10: *Schematic of the 3D microstructure of the ASB derived from the EDS mapping. The grey ellipses represent the beta grains. No alpha grains are shown as no microstructure information for the alpha phase was derived from the EDS STEM mapping. The orientation directions used in the Figure correspond to the beam direction used when obtaining an image taken in that orientation. For example: when taking an image showing the ASB propagating along the cylindrical axis, the beam direction will be aligned with the arrow labelled as Orientation A.*

from Orientation B are a result of the shear strain applied in the radial direction of the TWC. If the titanium 6Al-4V starting material had been more homogeneous and did not have an elliptical grain structure when viewed from Orientation A, then the EDS map of Orientation A would not show elongated beta grains aligned with the ASB.

6.1.5 Results Summary

The relatively undeformed material outside the ASB is taken to be representative of the starting material before the collapse of the TWC. The length of the original bar stock is parallel to the z-axis of the TWC. This can be seen in Figure 6.1, where Figure 6.1a taken from Orientation A (as defined in Figure 3.6) shows largely equi-axed alpha grains, with beta grains present between and Figure 6.1b shows more ovoid alpha grains, again with beta grains present in between. The rolling process used to generate the bar stock has produced a lengthening of the grains in the direction of rolling.

SEM images of the ASB show a clean, curving band with a definite direction along its path of propagation (Orientation B) and a much less well defined band showing multiple changes in direction along the z-axis of the TWC collapsed cylinder (Orientation A). Higher magnification images from the same orientations show elongated beta grains present along the path of propagation and no such elongation present in the image taken from Orientation A.

TKD mapping of a FIB sample taken from the ASB from Orientation A shows alpha and beta grains mixing within the ASB. No noticeable texture can be observed. The microstructure is composed of sub-micron grains with an average diameter of 150 nm. Clusters of beta phase grains can be seen aligned with the TWC z-axis. The sub-micron grains within these clusters have no common orientation. The proportion of alpha and beta phase within the ASB is the same as in the relatively undeformed material outside the ASB.

TEM images of the ASB taken from Orientation A show a clear line between the exterior and interior of the ASB. The microstructure within the ASB appears to be composed of a mixture of sub-micron equi-axed grains and more elongated grains tens of nanometres across. More detailed investigation within the ASB is made difficult by ion beam damage from the FIB sample preparation and the large degree of strain experienced by the material. The presence of multiple sub-micron grains was confirmed by the existence of a circular diffraction pattern within the ASB, reminiscent of a powder diffraction pattern and indicating the presence of multiple grains within the area selected

by the SAD aperture. Twinning was also detected throughout the ASB within individual sub-micron grains.

EDS maps of the ASBs were obtained from STEM imaging from Orientations A and B in order to better image the morphology of the beta grains within the ASBs. From Orientation A the beta grains were shown to reduce in both thickness and length within the ASB. This increased towards the centre of the ASB as the amount of strain experienced increased, with the grains eventually beginning to fragment. In contrast, the beta grains in Orientation B showed a change in orientation along their length, becoming thinner. At the centre of the ASB, the grains were at their thinnest and seemed to be beginning to fragment.

6.2 Discussion

The main purpose behind the TWC collapse experiment reported in the previous section was to ascertain whether a shaped impactor fired from a gas gun would produce the same response in a collapsed TWC specimen as explosive collapse. However, previous work investigating ASBs in TWC collapse experiments tended to focus on the evolution of the ASB, in what is described in Figure 3.6 as Orientation B, as the ASB propagates in the radial direction of the TWC. In this report, attention has also been given to the ASB in Orientation A, which is perpendicular to Orientation B. From Orientation A, the ASB can be seen propagating along the z-axis, or cylindrical axis of the TWC.

How Does the Adiabatic Shear Band Appear when Viewed from Orientation A and Orientation B?

As described in Section 2.7.4, during the collapse of a TWC, the ASB nucleates at the inner surface of the cylinder where the shear stress is the highest. Initially, the ASB propagation direction will be parallel with the radial axis of the TWC. As the ASB propagates through the specimen in the radial direction, the direction of propagation curves towards the direction of highest shear stress, which is at 45° to the radial direction. The SEM image shown in Figure 6.1a, taken from Orientation B, is at too high a magnification to see this curve in full, but the strong sense of directionality can still be seen. The curve shows no deviation in its path, even though that path has intersected with multiple alpha and beta grains. This is due to the path of the curve being dictated by macroscopic external forces, not the internal structure of the specimen. As the ASB accommodates more strain, the band will become wider, with the material at the centre of the band having been under strain for a longer period of time. The ASB observed from Orientation A is around 5 μm wide and the ASB observed from Orientation B is around 10 μm wide.

In contrast, the SEM image shown in Figures 6.1b and 6.1c, taken from Orientation A displays none of that kind of directionality. Instead, the ASB snakes backwards and forwards, running parallel with the length of the relatively undeformed beta grains outside of the ASB. An explanation of this behaviour comes from both the sites at

which ASB nucleation can occur and the loading state of the TWC specimen. As stated in Section 2.7.3, shear band nucleation occurs when homogeneous deformation becomes localised and the heat generated by deformation makes deformation easier. Macrostructural factors, such as the geometry of the loading apparatus, can affect the ASB nucleation sites, as mentioned above for the TWC collapse specimen seen from Orientation B. For example, in the TWC collapse experiment, the maximum shear stress is experienced at the inner surface of the cylinder, ensuring that ASB nucleation occurs there. Microstructural factors affecting localisation can include: grain size effects, geometrical softening and dislocation pileups at grain boundaries. During the TWC collapse, the stress applied to the specimen should be completely radial, with the stress and strain along the cylindrical axis equal to zero. This loading regime means that the effect of macrostructural factors on the ASB when observed from Orientation A will be the nucleation point of the ASB, i.e. its nucleation on the inner surface of the TWC. In the absence of macrostructural effects dictating the propagation direction of the ASB as observed in Orientation B, propagation is dominated by microstructural effects. This is the origin of the snaking path of the ASB in Orientation A. As there is no direction with the greatest shear stress to guide the ASB's direction of propagation, the band will proceed along the path of least resistance. In the case of the ASB shown in Figure 6.1b and 6.1c, this appears to involve travelling along the longer axis of the elongated alpha grains produced during the formation of the bar-stock and minimising travel across grain boundaries. A 3-dimensional representation of this macroscopic behaviour (not including grains) is shown in Figure 6.3.

Differences between Orientation A and Orientation B can also be seen in the interior microstructure of the ASB. Figures 6.2a and 6.2b show the shear band seen from Orientations A and B respectively. From Orientation B, the beta phase, visible within the grain as lighter coloured areas, has been stretched in the direction of shear band propagation. In contrast, in Orientation A the beta grains do not see the same kind of stretching. Longer beta grains aligned with the direction of the shear band propagation are still present, but these are parallel to the beta grains present within the relatively undeformed material outside of the shear band. These beta grains within the shear band appear to be shorter and narrower than those observed outside the shear band.

This behaviour is matched by the microstructure on the inside of the shear band observed in the EDS maps taken from both Orientations A and B, shown in Figures 6.8 and 6.9. The EDS maps taken from Orientation A showed the beta grains becoming smaller and thinner within the shear band. This decrease in size continued with decreasing distance from the centre of the shear band, with the beta grains imaged becoming smaller and eventually seeming to fragment into smaller grains. In contrast, the beta grains observed from Orientation B were seen to change orientation upon contact with the edges of the shear band, becoming narrower like the grains observed from Orientation A, but also being stretched along the length of the shear band. As with Orientation A, this also became more extreme towards the centre of the shear band. The beta grains are closer together towards the centre of the band and the beginning of fragmentation of the grains is also observed at the centre of the band, where the shear strain experienced by the material is greatest. A 3-dimensional representation of the microstructure within the shear band is shown in Figure 6.10.

These features suggest that the microstructure within the ASB is entirely dominated by the shearing of the Ti 6Al-4V in the radial direction, observed in Orientation B. If the nucleation of the shear band begins at a single point on the interior of the TWC, then ASB propagation must occur in both the radial direction, from the interior surface of the TWC to the exterior surface of the TWC, and along the z-axis of the TWC, starting from a nucleation point and proceeding along the length of the TWC. As discussed above, the propagation in the radial direction (as observed from Orientation B) is driven by the macrostructural factor of the geometry of the TWC. The propagation along the z-axis of the TWC (as oberved in Orientation A) effectively proceeds because the tip of the ASB when observed from Orientation A provides a point of localised strain which can act as a nucleation point for an ASB that will propagate in the radial direction. Phrased another way, an ASB observed at the inner wall of the collapsed TWC from Orientation A is a series of nucleation points for specific segments of shear bands whose primary shear strain is perpendicular to the z-axis of the TWC. The propagation of the ASB along the z-axis produces no noticeable deformation in the band in and of itself that is not a result of shear in the radial direction.

How Does the Microstructure Develop within the Adiabatic Shear Band?

Meyers *et al.* [9] proposed that the strain localisation necessary for the creation and propagation of an ASB was facilitated by dynamic recrystallisation. This requires a temperature in excess of around 40% of the melting point of the material, though Meyers *et al.* found evidence of recrystallisation in ASBs around 100°C lower than expected in ASBs generated using the hat shaped apparatus [9]. For Ti6Al-4V the expected recrystallisation temperature is $0.4T_M$, which is 670°C in titanium 6Al-4V.

Recrystallisation was found to have occurred in the ASBs investigated in the collapsed TWC specimen under investigation in this thesis. Figures 6.4 and 6.6 both show evidence of sub-micron grains around 150 nm across present in the ASBs. Further evidence of recrystallisation can be seen when comparing Figures 6.4b and 6.4c. The lines of beta grains seen in Figure 6.4c correspond to the elongated beta signals in Figure 6.8, where the beta grains aligned along the z-axis of the TWC have been stretched along the radial direction of the TWC. Figure 6.4b shows that these clusters of sub-micron grains show mis-orientation between the sub-micron grains. This is consistent with the fragmentation of these grains by dynamic recrystallisation via sub-grain rotation. Some evidence of the fragmentation of grains at the centre of the ASB is also visible in Figure 6.8, but the lack of orientation data makes it more difficult to determine the difference between an elongated beta grain and an elongated cluster of sub-micron beta grains. Figure 6.7 shows an example of a sub-micron grain containing an annealing twin. These twins are present throughout the ASB. Annealing twins form during recrystallisation and can help to direct the formation of the new microstructure.

Comparing the TKD phase map in Figure 6.4c and the relatively undeformed material in Figures 6.1a and 6.1b, it can be seen that the proportion of alpha and beta phase is unchanged within the ASB. This indicates that the highest temperature within the shear band during deformation is lower than the alpha-beta to beta transition in Ti 6Al-4V. This is 991°C. This puts the maximum temperature in the ASB during deformation between 670°C and 991°C in order for dynamic recrystallisation to occur without a change in the alpha and beta ratio. The lower end of this range is higher than previous measurements of ASB temperatures in Ti 6Al-4V, with Liao and Duffy [59] recording

a maximum temperature of 550°C. However, recrystallisation had occurred within the sample being measured, so this may not be the true temperature within the ASB. It is likely that this lower than expected temperature is a result of the infrared detector being used averaging the shear band temperature with that of the cooler, surrounding undeformed material.

It is worth noting that Me-Bar and Shechtman [72] observed phase transformation in ASBs generated by ballistic impact in Ti 6Al-4V. This suggests the potential for higher temperatures in ASBs. It may be that this is a result of the more complicated loading regime introduced by the ballistic test in comparison to the TWC collapse test.

6.3 Conclusions

A thick walled cylinder specimen composed of titanium 6Al-4V was collapsed at a high strain rate using a shaped projectile fired from a single stage gas gun. This experiment was carried out to examine the effectiveness of a new method of adiabatic shear band generation and to further investigate the three dimensional macroscopic and microscopic structure of shear bands generated within a collapsing TWC.

SEM imaging was used to investigate the macrostructural behaviour of the ASB from two orthogonal directions. It was found that the ASB propagation in the radial direction was dominated by geometrical factors in the loading process, with the propagation path guided entirely by the direction of greatest shear stress in a collapsing TWC. The ASB observed from Orientation B showed no sensitivity to the alpha and beta grains that were intersected along its path of propagation. Evidence of the dominance of geometrical factors in the TWC collapse can also be seen when observing the ASB from Orientation A, although in this case, the propagation path of the ASB along the z-axis of the TWC showed no obvious directionality and instead followed the path of least resistance through the specimen. This is entirely consistent with the loading regime experienced by the TWC, in which the stress and strain along the z-axis of the collapsing TWC are ideally zero. This is also seen on a smaller scale in the microstructure within the ASB, as shown by EDS, where beta grains observed from Orientation A are shown to become shorter and narrower within the shear band and beta grains observed from Orientation B become narrower, but also substantially longer within the shear band. This is a consequence of the beta grains being stretched along the shear band propagation direction along the radial axis of the TWC.

TKD and TEM were used to investigate how the microstructure within the ASB had developed. The grain size within the ASB had reduced to around 150 nm. Lines of sub-micron beta grains were observed in the TKD maps with mis-orientation between the grains. This suggests that sub-grain rotation has occurred during the formation of the sub-micron grains. These lines of mis-orientated sub-micron grains are equivalent to the beta grains with reduced length and thickness observed within the ASB from Orientation A. Annealing twins were also observed in sub-micron grains throughout the

ASB. This was found to be consistent with previous theories of ASB development.

Chapter 7

Overall Conclusions

Viewed individually, the separate chapters of this thesis appear to bear very little relation to each other. Three different metals (copper, tantalum and titanium 6Al-4V) are subjected to four different loading regimes (gas gun impact, SHPB, quasistatic compression and TWC collapse) at a range of strain rates, temperatures and maximum stresses. However, when a wider view is taken, a common thread emerges of the response of materials to loading being controlled by the impulse applied during that loading process.

At the rear half of a number of the shock loaded copper and tantalum specimens, a decrease in impulse due to a decrease in loading time hampered the recovery process and led to an increase in hardness.

The post-deformation behaviour of the quasistatically compressed tantalum specimens can be, in part, lined to the impulse applied. With varying strain rate, an increase in impulse by decreasing the strain rate resulted in increased interstitial mobility, leading to a greater decree of dislocation pinning, ultimately increasing the final hardness of the compressed specimens.

Although not linked directly to the initial loading impulse applied to the specimen, the lack of momentum trapping apparatus around the SHPB specimen allowed the introduction of lateral release waves into the specimen. This increased the total shear stress experienced by the specimen and enabled the generation of twins when the initial

applied stress was much lower than the expected twinning threshold.

Finally, ASBs, by virtue of being more complicated deformation features than either twins, dislocations, or even dislocation cells, require higher time scales to nucleate and then propagate.

The three metals are also linked by their use as model materials. In the cases of copper and tantalum, they are frequently used as model materials for the fcc and bcc structures respectively. Titanium 6Al-4V complicates the situation somewhat by being an alloy, not simply an hcp metal, but its perfect suitability for use in investigating the generation of ASBs puts it among the same company as the previous metals. Therefore, setting these materials side by side gives a useful overview into the response of different material structures to high strain rate loading.

Chapter 8

Future work

8.0.1 Plate Impact Shock Loading

The responses of annealed copper and tantalum to high loading rate impacts have been investigated over a wide range of peak shock pressures. In order to make a full appraisal of the effect of pre-working on the materials (cold-rolling prior to shock loading), a complementary series of shock loading experiments on cold-rolled copper and tantalum must be performed over an equivalent range of peak shock pressures.

The conclusion reached with respect to the linear increase in hardness shown towards the rear surface of some of the shock loaded copper and tantalum samples was that failures in the spall plates produced a linear decrease in peak loading time towards the rear surface of the specimen. The most obvious test of this hypothesis is to carry out a series of shock loading experiments using momentum trapping rings, but no spall plates, and to investigate the hardness profiles of the shock loaded specimens produced. This would lend weight to the failed spall plate hypothesis and also allow comparison between a specimen with a failed spall plate and a specimen with no spall plate. For example, a circumstance in which a shock loaded specimen with no spall plates showed an increase in damage in the spall plane relative to a specimen with a failed spall plate would suggest that the spall plate has only partially failed. This complicates the loading regime experienced by a specimen with a failed spall plate and decreases the reproducibility of the experiment.

If the increasing hardness profile can be reproduced consistently in the future, then this opens up further potential avenues of investigation. Previous investigations into the effects of peak pulse duration on materials controlled the pulse duration by using a thinner impactor, reducing the time between the shock wave entering the material and the release wave entering the material. Making use of a decreasing pulse duration with a known decay rate within the specimen would allow multiple pulse durations to be investigated with a single shock loading experiment. A thinner impactor also results in a less stable shock wave, so being able to investigate very low pulse durations without resorting to a very thin impactor would have definite advantages. FIB sample preparation would allow multiple samples to be taken from areas of known pulse duration from a single shock loaded specimen.

8.0.2 Compressed Tantalum

The range of compressed tantalum samples extends beyond the five samples investigated in this thesis. A full matrix of the quasi-statically compressed samples exists, including all combinations of the two quasi-static loading rates and the three temperatures used. In addition, all compression experiments were carried out on the cold-rolled tantalum material described in Chapter 4. Due to time constraints, it was impossible to investigate all available samples, but this would constitute a substantial and valuable survey of the response of tantalum to loading under various conditions.

One of the main disadvantages when discussing the SHPB sample was that comparisons between the quasi-statically compressed samples and the SHPB sample were difficult to make due to the large difference in applied strain. To solve this problem, a series of compression tests of tantalum should be carried out that mirror the existing sample set, but are limited to a plastic strain of 19% in order to match the SHBP test.

8.0.3 Adiabatic Shear Bands

Investigation into the interior of the ASBs from a TWC collapse experiment would be improved by high indexing rate TKD imaging of shear bands from both Orientation A and Orientation B. Three-dimensional imaging using either a RoboMet, or FIB milling for imaging the interior of the ASB would also be valuable.

The specimen investigated in this thesis contained fully formed ASBs that stretched from the interior surface of the TWC to the exterior surface and, in some cases, were beginning to show void nucleation. A collapsed TWC subjected to lower strains would hopefully contain less well developed ASBs, allowing FIB milling to be used in investigating the tip of an ASB, potentially enabling a full microscopic investigation of the ASB formation process.

References

[1] D. Hull and D. J. Bacon. *Introduction to Dislocations*. Elsevier, Amsterdam, fifth edition, 2011.

[2] W. A. Spitzig and T. E. Mitchell. Crystals Deformed in Tension at 373 K. *Acta Metallurgica*, 14:1311–1323, 1966.

[3] M. A. Meyers. *Dynamic Behavior of Materials*. Wiley-Interscience, New York, 1994.

[4] C. S. Smith. Metallographic Studies of Metals after Explosive Shock. *Transaction of the Metallurgical Society of AIME*, 212:574–589, 1958.

[5] E. Hornbogen. Shock-Induced Dislocations. *Acta Metallurgica*, 10:978–980, 1962.

[6] M. A. Meyers. A Mechanism for Dislocation Generation in Shock-Wave Deformation. *Scripta Metallurgica*, 12:21–26, 1978.

[7] C. H. Lu, B. A. Remington, B. R. Maddox, B. Kad, H. S. Park, S. T. Prisbrey, R. Luo, and M. A. Meyers. Laser Compression of Monocrystalline Tantalum. In *AIP Conference Proceedings*, pages 1391–1394, 2012.

[8] L. M. Barker, M. Shahinpoor, and L. C. Chhabildas. Experimental and Diagnostic Techniques. In J. R. Asay and M. Shahinpoor, editors, *High-Pressure Shock Compression of Condensed Matter*, pages 43–73. Springer Science + Business Media, New York, 1986.

[9] M. A. Meyers, G. Subhash, B. K. Kad, and L. Prasad. Evolution of Microstructure and Shear-Band Formation in Alpha-hcp Titanium. *Mechanics of Materials*, 17:175–193, 1994.

[10] V. F. Nesterenko, M. A. Meyers, and T. W. Wright. Self-Organisation in the Initiation of Adiabatic Shear Bands. *Acta Materialia*, 46:327–340, 1998.

[11] R. E. Winter, S. M. Stirk, E. J. Harris, D. J. Chapman, and D. E. Eakins. A Technique for Studying the Response of Materials to High Rate, High Strain Deformation. *International Journal of Impact Engineering*, 97:116–126, 2016.

[12] G. Hoffmann, O. Ottinger, and H.-J. Christ. The influence of mechanical prehistory on the cyclic stres-strain response and microstructure of single-phase metallic materials. In K.-T. Rie, H. W. Grunling, G. Konig, P. Neumann, H. Nowack, K.-H. Schwalbe, and T. Seeger, editors, *Low Cycle Fatigue and Elasto-Plastic Behaviour of Materials - 3*, pages 106–111. Elsevier Science Publishers Ltd, Oxford, 1992.

[13] N. K. Bourne. Materials' Physics in Extremes: Akrology. *Metallurgical and Materials Transactions A*, 42:2975–2984, 2011.

[14] J. R. Harris. Copper and Shipping in the Eighteenth Century. *The Economic History Review*, 19:550–568, 2008.

[15] P. S. Follansbee and G. T. Gray III. Plastic Deformation of Shock Prestrained Copper. *Materials Science and Engineering*, A138:23–31, 1991.

[16] M. A. Meyers, F. Gregori, B. K. Kad, M. S. Schneider, D. H. Kalantar, B. A. Remington, G. Ravichandran, T. Boehly, and J. S. Wark. Laser-Induced Shock Compression of Monocrystalline Copper: Characterization and Analysis. *Solid State Phenomena*, 35-36:1–18, 1993.

[17] Z. S. Basinski. Thermally Activated Glide in Face-Centred Cubic Metals and its Application to the Theory of Strain Hardening. *Philosophical Magazine*, 4:393–432, 1959.

[18] V. Caballero and S. K. Varma. Effect of Stacking Fault Energy and Strain Rate on the Microstructural Evolution During Room Temperature Tensile Testing in Cu and Cu-Al Dilute Alloys. *Journal of Materials Science*, 34:461–468, 1999.

[19] A. D. Rollett and U. F. Kocks. A Review of the Stages of Work Hardening. *Solid State Phenomena*, 35-36:1–18, 1993.

[20] J. F. Byron. Plastic Deformation of Tantalum Single Crystals: II. The Orientation Dependence of Yield. *Journal of Less Common Metals*, 14:201–210, 1968.

[21] T. E. Mitchell and W. A. Spitzig. Three-Stage Hardening in Tantalum Single Crystals. *Acta Metallurgica*, 13:1169–1179, 1965.

[22] R. Boyer, E. W. Collings, and G. Welsch. *Materials Properties Handbook: Titanium Alloys*. Materials Park, OH, 1994.

[23] E. A. Brandes, editor. *Smithells Metals Reference Book*. Butterworths, London, sixth edition, 1983.

[24] R. Komanduri and B. F. von Turkovich. New Observations on the Mechanism of Chip Formation when Machining Titanium Alloys. *Wear*, 69:179–188, 1981.

[25] Y. Karpat. Temperature Dependent Flow Strengthening of Titanium Alloy Ti6Al4V: An Investigation Using Finite Element Simulation of Machining. *Journal of Materials Processing Technology*, 211:737–749, 2010.

[26] G. Lutjering. Influence of Processing on Microstructure and Mechanical Properties of $(\alpha + \beta)$ Titanium Alloys. *Materials Science and Engineering*, 243:32–45, 1998.

[27] F. W. Wood and P. A. Romans. Segregation of Alpha and Beta Stabilizers in Titanium. *Materials Science and Engineering*, 10:182–185, 1972.

[28] N. Bourne. *Materials in Mechanical Extremes: Fundamentals and Applications*. Cambridge University Press, Cambridge, first edition, 2013.

[29] J. A. Zukas. *Introduction to Hydrocodes*. Elsevier, Amsterdam, 2004.

[30] W. E. Carrington and M. L. V. Gayler. Changes in Microstructure Caused by Deformation under Impact at High-Striking Velocities. *Proceedings of the Royal Society*, 194 A:323–331, 1948.

[31] F. C. Frank. On the Equations of Motion of Crystal Dislocations. *Proceedings of the Physics Society A*, 62:131–134, 1949.

[32] J. D. Eshelby. Supersonic Dislocations and Dislocations in Dispersive Media. *Proceedings of the Physics Society B*, 69:1013–1019, 1956.

[33] J. G. Avery and T. R. Porter. Comparisons of the Ballistic Impact Response of Metals and Composites for Military Aircraft Applications. In L. B. Greszczuk, editor,

Foreign Object Impact Damage to Composites, pages 3–29. American Society for Testing and Materials, North Wales, 1975.

[34] S. P. Timothy and I. M. Hutchings. Structure of Adiabatic Shear Bands in a Titanium Alloy. *Acta Metallurgica*, 33:667–676, 1985.

[35] M. A. Meyers and H.-R. Pak. Observation of an Adiabatic Shear Band in Titanium by High-Voltage Transmission Electron Microscopy. *Acta Metallurgica*, 34:2493–2499, 1986.

[36] P. C. Chou, J. Hashemi, A. Chou, and H. C. Rogers. Experimentation and Finite Element Simulation of Adiabatic Shear Bands in Controlled Penetration Impact. *International Journal of Impact Engineering*, 11:305–321, 1991.

[37] D. L. Zou, L. Zhen, C. Y. Xu, and W. Z. Shao. Characterization of Adiabatic Shear Bands in AM60B Magnesium Alloy under Ballistic Impact. *Materials Characterization*, 62:496–502, 2011.

[38] R. G. McQueen and S. P. Marsh. Equation of State for Nineteen Metallic Elements form Shock-Wave Measurements to Two Megabars. *Journal of Applied Physics*, 31:1253–1269, 1960.

[39] R. G. McQueen, S. P. Marsh, J. W. Taylor, J. N. Fritz, and W. J. Carter. The Equation of State of Solids from Shock Wave Studies. In R. Kinslow, editor, *High Velocity Impact Phenomena*, pages 293–299. Academic Press, New York, 1970.

[40] P. S. Follansbee and G. T. Gray III. The Response of Single Crystal and Polycrystal Nickel to Quasistatic and Shock Deformation. *International Journal of Plasticity*, 7:651–660, 1991.

[41] P. S. Follansbee and G. T. Gray III. Dynamic Deformation of Shock Prestrained Copper. *Materials Science and Engineering*, A138:23–31, 1991.

[42] G. T. Gray III and K. S. Vecchio. Influence of Peak Pressure and Temperature on the Structure/Property Response of Shock-Loaded Ta and Ta-10W. *Metallurgical and Materials Transactions A*, 26A:2555–2563, 1995.

[43] B. Pang, I. P. Jones, J. C. F. Millett, G. Whiteman, N. Bourne, and Y.-L. Chiu. Radial Stress Release Wave Induced Twinning in a Tantalum Single Crystal. *Metallurgical and Materials Transactions A*, 46:4522–4526, 2015.

[44] N. K. Bourne and G. T. Gray III. Computational Design of Recovery Experiments for Ductile Metals. *Proceedings of the Royal Society A*, 461:3297–3312, 2005.

[45] N. K. Bourne, G. T. Gray III, and J. C. F. Millett. On the Shock Response of Cubic Metals. *Journal of Applied Physics*, 106:091301–1–091301–14, 2009.

[46] H. Tresca. *Proceedings of the Institute of Mechanical Engineers*, 30:301–345, 1878.

[47] C. Zener and J. H. Hollomon. Effect of Strain Rate Upon Plastic Flow of Steel. *Journal of Applied Physics*, 15:22–32, 1944.

[48] S. A. Manion and T. A. C. Stock. Adiabatic Shear Bands in Steel. *International Journal of Fracture Mechanics*, 6:106–107, 1970.

[49] J. H. Beatty, L. W. Meyer, M. A. Meyers, and S. Nemat-Nasser. Formation of Controlled Adiabatic Shear Bands in AISI 4340 High Strength Steel. Technical Report AD-A230 99, U.S. Army Materials Technology Laboratory, 1990.

[50] Q. Xue, V. F. Nesterenko, and M. A. Meyers. Evaluation of the Collapsing Thick-Walled Cylinder Technique for Shear-Band Spacing. *International Journal of Impact Engineering*, 28:257–280, 2003.

[51] P. Cizek, F. Bai, W. M. Rainforth, and J. H. Beynon. Fine Structure of Shear Bands Formed during Hot Deformation of Two Austenitic Steels. *Materials Transactions*, 45:2157–2164, 2004.

[52] J. F. C. Lins, H. R. Z. Sandim, H.-J. Kestenbach, D. Raabe, and K. S. Vecchio. A Microstructural Investigation of Adiabatic Shear Bands in an Interstitial Free Steel. *Materials Science and Engineering A*, 457:205–218, 2007.

[53] C. S. Lee, W. T. Hui, and B. J. Duggan. Macroscopic Shear Bands in Cross-Rolled Alpha Brass. *Materials Science and Engineering A*, 457:205–218, 2007.

[54] S. Nourbakhsh and Q. Song. Shear Band Formation in Heavily Cold-Rolled 70-30 Brass. *Metallurgical Transactions A*, 20:1267–1275, 1989.

[55] T. Kozmel, M. Vural, and S. Tin. EBSD characterization of Shear Band Formation in Aluminum Armor Alloys. *Journal of Materials Science*, 51:7554–7570, 2016.

[56] T. D. Rostova and V. V. Zakharov. Shear Bands in Aluminum-Lithium Alloys. *Metal Science and Heat Treatment*, 39:236–239, 1997.

[57] Q. Xue, M. A. Meyers, and V. F. Nesterenko. Self-Organisation of Shear Bands in Titanium and Ti-6Al-4V Alloy. *Acta Materialia*, 50:575–596, 2002.

[58] Y. Yang, B. F. Wang, J. Xiong, X. Y. Yang, Y. Zeng, and Z. P. Chen. Adiabatic Shear Bands on the Titanium Side in the Titanium/Mild Steel Explosive Cladding Interface: Experiments, Numerical Simulation, and Microstructure Evolution. *Metallurgical and Materials Transactions A*, 37A:3131–3137, 2006.

[59] S.-C. Liao and J. Duffy. Adiabatic Shear Bands in a Ti-6Al-4V Titanium Alloy. *Journal of Mechanics and Physics of Solids*, 46:2201–2231, 1998.

[60] J. Peirs, W. Tirry, B. Amin-Ahmandi, F. Coghe, P. Verleysen, L. Rabet, D. Schryvers, and J. Degrieck. Microstructure of Adiabatic Shear Bands in Ti6Al4V. *Materials Characterization*, 75:79–92, 2013.

[61] S. M. Fatemi-Varzaneh, A. Zarei-Hanzaki, and J. M. Cabrera. Shear Banding During Severe Plastic Deformation of an AZ91 Magnesium Alloy. *Journal of Alloys and Compounds*, 507:3806–3810, 2011.

[62] R. C. Batra and Z. Peng. Development of Shear Bands in Dynamic Plane Strain Compression of Depleted Uranium and Tungsten Blocks. *International Journal of Impact Engineering*, 16:375–395, 1995.

[63] L. S. Magness Jr. High Strain Rate Deformation Behaviours of Kinetic Energy Penetrator Materials During Ballistic Impact. *Mechanics of Materials*, 17:147–154, 1994.

[64] P. Bésuelle. Compacting and Dilating Shear Bands in Porous Rock: Theoretical and Experimental Conditions. *Journal of Geophysical Research: Solid Earth*, 106:13435–13442, 2001.

[65] A. G. Evans and B. J. Dalgleish. Influence of Shear Bands on Creep Rupture in Ceramics. *Journal of the American Ceramic Society*, 68:44–48, 1985.

[66] R. B. Frey. The initiation of explosive charges by rapid shear. In *Proceedings of the 7th Symposium on Detonation*, 1981.

[67] J. H. Giovanola. Adiabatic Shear Banding under Pure Shear Loading - Part I: Direct Observation of Strain Localization and Energy Dissipation Measurements. *Mechanics of Materials*, 7:59–71, 1988.

[68] J. H. Giovanola. Adiabatic Shear Banding under Pure Shear Loading - Part II: Fractographic and Metallographic Observations. *Mechanics of Materials*, 7:73–87, 1988.

[69] S. M. Walley. Shear Localization: A Historical Overview. *Metallurgical and Materials Transactions A*, 38A:2629–2654, 2007.

[70] T. J. Burns and M. A. Davies. On Repeated Adiabatic Shear Band Formation During High-Speed Machining. *International Journal of Plasticity*, 18:487–506, 2002.

[71] P. S. Mathur and W. A. Backofen. Mechanical Contributions to the Plane-Strain Deformation and Recrystallization Textures of Aluminum-Killed Steel. *Metallurgical Transactions*, 4:643–651, 1973.

[72] Y. Me-Bar and D. Shechtman. On the Adiabatic Shear of Ti-6Al-4V Ballistic Targets. *Materials Science and Engineering*, 58:181–188, 1983.

[73] L. W. Meyer and S. Manwaring. Metallurgical Applications of Shock-Wave and High Strain-Rate Phenomena. In M. A. Meyers L. E. Murr, K. P. Staudhammer, editor, *Metallurgical Applications of Shock-Wave and High Strain-Rate Phenomena*, pages 657–674. Dekker, New York, 1986.

[74] J. Peirs, P. Verleysen, J. Degrieck, and F. Coghe. The Use of Hat-Shaped Specimens to Study the High Strain Rate Shear Behavior of Ti-6Al-4V. *International Journal of Impact Engineering*, 37:703–714, 2010.

[75] V. F. Nesterenko and M. P. Bondar. Localization of Deformation in Collapse of a Thick Walled Cylinder. *Combustion, Explosion and Shock Waves*, 30:500–509, 1994.

[76] H. A. Grebe, H.-R. Pak, and M. A. Meyers. Abiabatic Shear Localization in Titanium and Ti-6 Pct Al-4 Pct V Alloy. *Metallurgical Transactions A*, 16A:761–775, 1985.

[77] D. E. Grady and M. E. Kip. The Growth of Unstable Thermoplastic Shear with Application to Steady-Wave Shock Compression in Solids. *Journal of the Mechanics and Physics of Solids*, 35:95–119, 1987.

[78] T. W. Wright and H. Ockendon. A Scaling Law for the Effect of Inertia on the Formation of Adiabatic Shear Bands. *International Journal of Plasticity*, 12:927–934, 1996.

[79] M. A. Meyers, F. Gregori, and B. K. Kad. Laser-Induced Shock Compression of Monocrystalline Copper. *Acta Materialia*, 51:1211–1228, 2003.

[80] J. B. Clark, R. K. Garrett Jr, T. L. Jungling, R. A. Vandermeer, and C. L. Vold. Effect of Processing Variable on Texture and Texture Gradients in Tantalum. *Metallurgical Transactions A*, 22A:2039–2048, 2015.

[81] K. Wongwiwat and L. E. Murr. Effect of Shock Pressure, Pulse Duration and Grain Size on Shock-Deformation Twinning in Molybdenum. *Materials Science and Engineering*, 35:273–285, 1978.

[82] C.-Y. Hsu, K.-C. Hsu, L. E. Murr, and M. A. Meyers. The Attenuation of Shock Waves in Nickel. In M. A. Meyers and L. E. Murr, editors, *Shock Waves and High Strain-Rate Phenomena in Metals*, pages 433–452. Plenum Publishing Corporation, New York, 1981.

[83] M. A. Meyers, K.-C. Hsu, and K. Couch-Robino. The Attenuation of Shock Waves in Nickel: Second Report. *Materials Science and Engineering*, 59:235–249, 1983.

[84] V. Vitek. Effect of Dislocation Core Structure on the Plastic Properties of Metallic Materials. In Institute of Metals CRU Unit and M. H. Loretto, editors, *Dislocations and Properties of Real Materials*, pages 30–50. Institute of Metals, London, 1985.

[85] J. C. F. Millett, G. Whiteman, N. T. Park, S. Case, and N. K. Bourne. The Role of Cold Work on the Shock Response of Tantalum. *Journal of Applied Physics*, 113:233502–1–233502–10, 2013.

[86] W. M. Isbell. *Shock Waves: Measuring the Dynamic Response of Materials*. Imperial College Press, London, 2005.

[87] B. H. Sencer, S. A. Maloy, and G. T. Gray III. The Influence of Shock-Pulse Shape on the Structure/Property Behavior of Copper and 316 L Austenitic Stainless Steel. *Acta Materialia*, 53:3293–3303, 2005.

[88] E. Moin and L. E. Murr. The Ineractive Effects of Shock Loading Parameters on the Substructure and Mechanical Properties of Nickel and Stainless Steel. *Materials Science and Engineering*, 37:249–269, 2005.

[89] J. C. F. Millett, N. K. Bourne, N. T. Park, G. Whiteman, and G. T. Gray III. On the Behaviour of Body-Centred Cubic Metals to One-Dimensional Shock Loading. *Journal of Materials Science*, 46:3899–3906, 2011.

[90] S. H. Carpenter and G. S. Baker. Dislocation-Interstitial Interactions in Single-Crystal Tantalum. *Journal of Applied Physics*, 36:1733–1738, 1965.

[91] R. L. Smialek and T. E. Mitchell. Interstitial Solution Hardening in Tantalum Single Crystals. *Philosophical Magazine*, 22:1105–1127, 1970.

[92] L. Stainier, A. M. Cuitino, and M. Ortiz. A Micromechanical Model of Hardening, Rate Sensitivity and Thermal Softening in bcc Single Crystals. *Journal of the Mechanics and Physics of Solids*, 50:1511–1545, 2002.